

Springer Theses

Recognizing Outstanding Ph.D. Research

Bhuvnesh Bharti

Adsorption, Aggregation and Structure Formation in Systems of Charged Particles

From Colloidal to Supracolloidal
Assembly

 Springer

Springer Theses

Recognizing Outstanding Ph.D. Research

For further volumes:

<http://www.springer.com/series/8790>

Aims and Scope

The series “Springer Theses” brings together a selection of the very best Ph.D. theses from around the world and across the physical sciences. Nominated and endorsed by two recognized specialists, each published volume has been selected for its scientific excellence and the high impact of its contents for the pertinent field of research. For greater accessibility to non-specialists, the published versions include an extended introduction, as well as a foreword by the student’s supervisor explaining the special relevance of the work for the field. As a whole, the series will provide a valuable resource both for newcomers to the research fields described, and for other scientists seeking detailed background information on special questions. Finally, it provides an accredited documentation of the valuable contributions made by today’s younger generation of scientists.

Theses are accepted into the series by invited nomination only and must fulfill all of the following criteria

- They must be written in good English.
- The topic should fall within the confines of Chemistry, Physics, Earth Sciences, Engineering and related interdisciplinary fields such as Materials, Nanoscience, Chemical Engineering, Complex Systems and Biophysics.
- The work reported in the thesis must represent a significant scientific advance.
- If the thesis includes previously published material, permission to reproduce this must be gained from the respective copyright holder.
- They must have been examined and passed during the 12 months prior to nomination.
- Each thesis should include a foreword by the supervisor outlining the significance of its content.
- The theses should have a clearly defined structure including an introduction accessible to scientists not expert in that particular field.

Bhuvnesh Bharti

Adsorption, Aggregation and Structure Formation in Systems of Charged Particles

From Colloidal to Supracolloidal Assembly

Doctoral Thesis accepted by
Technical University of Berlin, Germany

 Springer

Author

Dr. Bhuvnesh Bharti
Department of Chemical and Biomolecular
Engineering
North Carolina State University
Raleigh
USA

Supervisor

Prof. Gerhard H. Findenegg
Stranski Laboratorium
Department of Chemistry
Technical University of Berlin
Berlin
Germany

ISSN 2190-5053

ISBN 978-3-319-07736-9

DOI 10.1007/978-3-319-07737-6

Springer Cham Heidelberg New York Dordrecht London

ISSN 2190-5061 (electronic)

ISBN 978-3-319-07737-6 (eBook)

Library of Congress Control Number: 2014941099

© Springer International Publishing Switzerland 2014

This work is subject to copyright. All rights are reserved by the Publisher, whether the whole or part of the material is concerned, specifically the rights of translation, reprinting, reuse of illustrations, recitation, broadcasting, reproduction on microfilms or in any other physical way, and transmission or information storage and retrieval, electronic adaptation, computer software, or by similar or dissimilar methodology now known or hereafter developed. Exempted from this legal reservation are brief excerpts in connection with reviews or scholarly analysis or material supplied specifically for the purpose of being entered and executed on a computer system, for exclusive use by the purchaser of the work. Duplication of this publication or parts thereof is permitted only under the provisions of the Copyright Law of the Publisher's location, in its current version, and permission for use must always be obtained from Springer. Permissions for use may be obtained through RightsLink at the Copyright Clearance Center. Violations are liable to prosecution under the respective Copyright Law.

The use of general descriptive names, registered names, trademarks, service marks, etc. in this publication does not imply, even in the absence of a specific statement, that such names are exempt from the relevant protective laws and regulations and therefore free for general use.

While the advice and information in this book are believed to be true and accurate at the date of publication, neither the authors nor the editors nor the publisher can accept any legal responsibility for any errors or omissions that may be made. The publisher makes no warranty, express or implied, with respect to the material contained herein.

Printed on acid-free paper

Springer is part of Springer Science+Business Media (www.springer.com)

Parts of this thesis have been published in the following journal articles:

1. B. Bharti; J. Meissner; S. H. L. Klapp; G. H. Findenegg, “Bridging interaction of protein with silica nanoparticles: Influence of pH, ionic strength and protein concentration”, *Soft Matter*, **2014**, *10*, 718.
2. B. Bharti; G. H. Findenegg; O. D. Velev, “Co-Assembly of Oppositely Charged Particles into Linear Clusters and Chains of Controllable Length”, *Sci. Rep. (Nature)*, **2012**, *2*, 1004.
3. B. Bharti; M. Xue; J. Meissner; V. Cristiglio; G. H. Findenegg, “Assembling Wormlike Micelles in Tubular Nanopores by Tuning Surfactant-Wall Interactions”, *J. Am. Chem. Soc.*, **2012**, *134*, 14756.
4. B. Bharti; G. H. Findenegg, “Protein-specific Effects of Binding to Silica Nanoparticles”, *Chem. Lett.*, **2012**, *41*, 1122.
5. B. Bharti; J. Meissner; U. Gasser; G. H. Findenegg, “Surfactant Adsorption and Aggregate Structure at Silica Nanoparticles: Effects of Particle Size and Surface Modification”, *Soft Matter*, **2012**, *8*, 6573.
6. B. Bharti; J. Meissner; G. H. Findenegg, “Aggregation of Silica Nanoparticles Directed by Adsorption of Lysozyme”, *Langmuir*, **2011**, *27*, 9823.

*No problem can stand the assault of
sustained thinking.*

C. F. Kettering

Supervisor's Foreword

Interaction of inorganic colloids with soft matter covers a wide range of phenomena that play an important role in the natural environment as well as in industrial and biomedical applications. In his Ph.D. work, Bhuvnesh Bharti addresses fundamental questions about the interaction of surfactants and proteins with nanoscale silica materials. Concepts developed from the study of interactions of soft and hard matter at the nanoscale are then used for assembling permanent linear chain structures of oppositely charged polystyrene microbeads.

Threadlike molecular assemblies are excluded from narrow pores unless attractive interactions with the confining pore walls compensate for the loss of configurational entropy. In the thesis it is shown by small-angle neutron scattering (SANS) that wormlike micelles of the nonionic surfactant $C_{12}E_5$ can be assembled in the 8 nm tubular nanopores of SBA-15 ordered mesoporous silica by adjusting the interaction of the surfactant with the pore walls. In addition, the curvature of the adsorbing surface also has a significant influence on the morphology of the surface aggregates. This is indicated by an observed strong decrease in the limiting adsorption of $C_{12}E_5$ with decreasing diameter of silica nanoparticles. I believe that the concept of tuning the surfactant–substrate interactions by changing curvature or by adding a surface modifier will be applicable to a variety of self-assembling molecules and nano-curved surfaces. Experimental and theoretical follow-up studies have confirmed the importance of this work.

pH-induced ionization of weakly acidic or basic surface groups on colloidal particles represents another important route to manipulate interactions at the nanoscale. Specifically, the interplay between attractive and repulsive interactions of a pair of oppositely charged particles can lead to the formation of unique supramolecular assemblies. In the thesis, the globular protein lysozyme and silica nanoparticles (20 nm) have been chosen as a model system which was studied by a combination of experimental techniques over a wide range of pH and ionic strength. It was found that the adsorption affinity and binding capacity of lysozyme on the silica particles increases strongly with increasing pH, indicating the directing role of electrostatic interactions in the adsorption processes. Analytical centrifugation and small-angle X-ray scattering studies showed that the adsorbed protein induces bridging aggregation of the silica particles. Compact aggregates were formed at pH 4–6, but loose flocculated network at pH 7–9,

followed by a sharp decrease in aggregate size near the isoelectric point (IEP) of lysozyme. The results of silica aggregation in the presence of lysozyme were compared with a similar globular protein (cytochrome C). In this case, a shift in the aggregating pH regime was observed and attributed to the non-uniform surface charge distribution of the cytochrome C. These studies have already been widely appreciated in the scientific community.

As concluded from the protein-particle project, oppositely charged colloidal particles snap on contact and form permanent, but disordered aggregates. In contrast, AC-electric fields can cause a directional assembly of chains from repulsive particles by dielectrophoresis (DEP), but these structures fall apart once the field is switched off. In this thesis it has been demonstrated that well-organized, permanent clusters and chains of micron-sized particles can be assembled by applying DEP to mixtures of oppositely charged microspheres. It was found that the assembly process depends on the size ratio as well as the number ratio of the two particles, and a set of *assembly rules* for the structures resulting from the process could be formulated. This study forms a basis for tailoring new classes of permanent supra-colloidal clusters and gels.

Berlin, Germany, April 2014

Prof. Gerhard H. Findenegg

Acknowledgments

First and foremost I offer my sincere gratitude to my supervisor, Prof. Gerhard H. Findenegg, who encouraged me throughout the tenure of my thesis. This Ph.D. work would not have been possible without his constant support and luminous guidance. In equal measures, I am thankful to my second supervisor, Prof. Orlin D. Velev for hosting me at NCSU, and guiding me with his patience, knowledge and innovative ideas during my stay in his group. I would also like to acknowledge the useful discussions and inputs given by Professors R. v Klitzing, S. Klapp, D. Lerche, S. K. Mehta and M. Gradzielski.

I am grateful to Jens Meissner for his help with the experiments; he has been a great asset to me not only in my Ph.D. work, but also as a close friend. I am also thankful to Dr. D. Lugo (TU, Berlin) and Dr. S. Gangwal (NCSU, Raleigh) for their help in starting up the new projects. In addition, I would like to express my gratitude to Dr. S. Prévost (TU Berlin) and Dr. S. Smukov (NCSU, Raleigh) for their useful ideas and advices. I highly appreciate the help of Dr. T. Söbisch (LUM, Berlin), Dr. U. Gasser (PSI, Zurich), Dr. V. Cristiglio (ILL, Grenoble), Dr. J. Justin (LLB, Saclay), S. Selve (ZELMI, Berlin), Dr. T. Mielke and J. Bürger (MPI für Molekulare Genetik, Berlin) for their helps with the various experimental techniques.

I am indebted to Deutsche Forschungsgemeinschaft (DFG) in the frame work of IGRTG-1524 for the financial support. I am grateful to all IGRTG members; specifically, I would like to thank the Chairman, Prof. M. Schön, Managing Director, Dr. D. Fliegner and Administrative Assistant, Mrs. P. Erdmann for their friendly support. I am also thankful to secretaries, Christiane, Maria and CTA's Ingeke, René, Michaela, Gabi and Jana for their help with the bureaucratic and experimental work.

I consider myself to be lucky to have such awesome colleagues both in TU Berlin as well as in NCSU Raleigh. Specially, I would like to thank Raphael, Heiko and Ravneet for their friendly support and motivation.

Contents

Part I Introduction and Basics

| | | |
|----------|---|----|
| 1 | Introduction | 3 |
| 1.1 | Why Study Colloidal Interactions? | 3 |
| 1.2 | Interaction of Nanoparticles with Nonionic Surfactants | 4 |
| 1.3 | Protein-Nanoparticle Interactions | 5 |
| 1.4 | Supra-Colloidal Permanent Assembly of Microparticles. | 7 |
| 1.5 | Overview | 8 |
| 1.6 | Thesis Outline | 9 |
| 1.6.1 | Part-I: Introduction and Basics. | 9 |
| 1.6.2 | Part-II: Curvature and Surface Energy Effects on the Interaction of Hydrophilic Silica with Nonionic Surfactant | 10 |
| 1.6.3 | Part-III: Adsorptive and Aggregative Effects of Proteins on Silica Nanoparticles | 10 |
| 1.6.4 | Part-IV: Field Directed Assembly of Hetero-Aggregating Microparticles | 10 |
| 1.6.5 | Part-V: Summary and Outlook. | 11 |
| | References. | 11 |
| 2 | Methods | 15 |
| 2.1 | Synthesis and Characterization of Silica Nanoparticles. | 15 |
| 2.1.1 | Synthesis | 15 |
| 2.1.2 | Zeta Potential | 16 |
| 2.1.3 | Nitrogen Adsorption. | 17 |
| 2.2 | Adsorption at Solid/Liquid Interface | 18 |
| 2.2.1 | Surfactant Adsorption. | 19 |
| 2.2.2 | Protein Adsorption | 20 |
| 2.3 | Turbidity and Analytic Centrifugation | 22 |
| 2.4 | Small Angle Scattering. | 23 |
| 2.5 | Small Angle Diffraction | 26 |
| | References. | 27 |

| | | |
|---|---|----|
| 3 | Theory and Modeling | 29 |
| 3.1 | Scattering Data Analysis | 29 |
| 3.1.1 | Micelle-Decorated Bead Model | 30 |
| 3.1.2 | Raspberry-Like Bead Model | 33 |
| 3.2 | Particle Assembly | 34 |
| 3.2.1 | Dielectrophoresis | 34 |
| 3.2.2 | Chain-Length Distribution from Numerical Simulations | 36 |
| 3.2.3 | Equally-Sized Particles: Random Arrangement of Balls | 36 |
| 3.2.4 | Differently-Sized Particles: Throwing Balls in Boxes | 37 |
| 3.2.5 | Statistical Model for Chain Length Distribution | 38 |
| 3.2.6 | Equally-Sized Particles | 38 |
| 3.2.7 | Differently-Sized Particles | 39 |
| | References | 42 |
| | | |
| Part II Curvature and Surface Energy Effects on the Interaction of Hydrophilic Silica with Nonionic Surfactant | | |
| 4 | Surfactant Adsorption and Aggregate Structure at Silica Nanoparticles | 47 |
| 4.1 | Introduction | 47 |
| 4.2 | Results | 48 |
| 4.2.1 | Characterization of Silica Nanoparticles | 48 |
| 4.2.2 | Surfactant Adsorption on Lys-Sil Nanoparticles | 49 |
| 4.2.3 | Lysine Adsorption on Silica Nanoparticles | 50 |
| 4.2.4 | SANS Study of Surfactant Aggregate Structure | 51 |
| 4.3 | Discussion | 54 |
| 4.3.1 | Size Dependence of the Adsorption of C ₁₂ E ₅ on Lys-Sil | 54 |
| 4.3.2 | Effect of Lysine on Binding Strength of Surfactant | 56 |
| 4.3.3 | Potential Application Relevance | 57 |
| 4.4 | Conclusions | 59 |
| | References | 59 |
| | | |
| 5 | Assembling Wormlike Micelles in Tubular Nanopores by Tuning Surfactant-Wall Interactions | 63 |
| 5.1 | Introduction | 63 |
| 5.2 | Theoretical Background | 64 |
| 5.3 | Experimental | 67 |
| 5.3.1 | Characterization of SBA-15 | 67 |
| 5.3.2 | Lysine Adsorption | 67 |
| 5.3.3 | Sample Preparation and SANS Measurements | 68 |

| | | |
|-------|------------------------|----|
| 5.4 | Results | 69 |
| 5.4.1 | Lysine Adsorption | 69 |
| 5.4.2 | SANS Results | 70 |
| 5.5 | Discussion | 74 |
| 5.5.1 | Lysine Adsorption | 74 |
| 5.5.2 | Lysine Induced Effects | 74 |
| 5.6 | Conclusion | 76 |
| | References | 76 |

Part III Adsorptive and Aggregative Effects of Proteins on Silica Nanoparticles

| | | |
|----------|---|-----|
| 6 | Aggregation of Silica Nanoparticles Directed by Adsorption of Lysozyme | 81 |
| 6.1 | Introduction | 81 |
| 6.2 | Results | 81 |
| 6.2.1 | Characterization of Silica Nanoparticles | 82 |
| 6.2.2 | Lysozyme Adsorption | 83 |
| 6.2.3 | pH Effects at a Constant Protein-to-Silica Ratio | 85 |
| 6.2.4 | Characterization by Analytical Centrifuge | 88 |
| 6.2.5 | Cryo-TEM Study of Flocculation | 90 |
| 6.2.6 | SAXS Study of Flocculate | 91 |
| 6.2.7 | Influence of Polydispersity on the Evaluation of $S(q)$ | 93 |
| 6.3 | Discussion | 95 |
| 6.3.1 | Nature of Adsorptive Interaction | 95 |
| 6.3.2 | Protein-Induced Aggregation | 96 |
| 6.3.3 | Interparticle Bonds and Flocculate Structure | 97 |
| 6.4 | Conclusions | 99 |
| | References | 100 |
| 7 | Effect of pH and Salinity on Silica–Lysozyme Hetero-Aggregation | 103 |
| 7.1 | Introduction | 103 |
| 7.2 | Results | 104 |
| 7.2.1 | Adsorption Isotherms | 104 |
| 7.2.2 | pH Driven Lysozyme Binding | 106 |
| 7.2.3 | Aggregation of Protein/Silica Core-Shell Composite | 106 |
| 7.3 | Discussion | 114 |
| 7.3.1 | Role of Electrostatic Interactions | 114 |
| 7.3.2 | Protein Induced Silica Aggregation | 115 |
| 7.3.3 | Lysozyme/Silica Patchy Particles | 116 |
| 7.4 | Conclusions | 117 |
| | References | 117 |

| | | |
|---|--|------------|
| 8 | Protein-Specific Effects of Binding to Silica Nanoparticles | 121 |
| 8.1 | Introduction | 121 |
| 8.2 | Results | 121 |
| | 8.2.1 Characterization of Proteins | 121 |
| | 8.2.2 Protein-Binding to Silica Surface | 123 |
| 8.3 | Discussion | 126 |
| 8.4 | Conclusions | 128 |
| | References | 128 |
| | | |
| Part IV Field Directed Assembly of Hetero-Aggregating Microparticles | | |
| 9 | Permanent Supracolloidal Biparticle Assembly Triggered by an Electric Field | 131 |
| 9.1 | Introduction | 131 |
| 9.2 | Methods | 132 |
| 9.3 | Results and Discussion | 132 |
| | References | 138 |
| | | |
| Part V Summary and Outlook | | |
| 10 | Summary and Outlook | 143 |
| 10.1 | Interaction Between Hydrophilic Silica and a Nonionic Surfactant | 143 |
| 10.2 | Protein-Nanoparticle Interactions | 144 |
| 10.3 | Supra-Colloidal Permanent Assembly of Microparticles | 145 |
| Appendix | | 147 |

Part I

Introduction and Basics

After a general introduction to the subject area and the systems studied (Chap. 1), the main experimental methods used for studying the system, including the measurement of adsorption isotherms, small angle scattering and diffraction, are summarized in Chap. 2. A detailed account of the analysis of the scattering data and the theory behind it is given in Chap. 3. This chapter also explains the basics of particle chaining in an AC-electric field due to dielectrophoresis (DEP), and provides a detailed account of the statistical approach for predicting the length of permanent chain structure developed in this work.

Chapter 1

Introduction

1.1 Why Study Colloidal Interactions?

Colloid science is known to the scientific community for 150 years since the pioneering work of Thomas Graham in the 1860s. In terms of length scales, the colloidal regime is roughly considered between 1 nm and 1,000 nm [1]. It covers the size range between simple molecules and objects visible in a light microscope. In many cases a colloidal system consists of two distinct phases: a *dispersed phase* (or *internal phase*) and a *continuous phase* (or *dispersion medium*). Depending upon the form of dispersed phase and dispersion medium, colloidal system can be solid in liquid, liquid in liquid, liquid in gas, etc.

The interactions between colloidal particles play a vital role in colloidal stability and lead to a wealth of important and interesting kind of dispersion behavior [2, 3]. Colloids consisting of *nano* and *micron* sized particles play an important role in industrial products like paints, varnishes, inks, cosmetics, etc. [4, 5], and are also extensively involved in food products [6, 7] and bio-medical applications [8–10] like imaging [11], bacterial detections [12], protein fibrillation [13], also as drug carriers [14]. Large-scale structures (one-, two-, or three-dimensional), assembled by colloidal particles as their building units have found applications in many fields of modern technology, including infrared-emitting nano crystals [15], surface coatings [16], single-nanowire light emitting diodes [17], single electron transistors [18] and in microfluidic devices [19]. Interactions between *nano*- and *micro*-sized inorganic colloid particles of fixed shape (*hard matter*), as well as interactions between hard and *soft matter* (surfactants, proteins and polymers) is of great relevance in the field of nanotechnology and holds the key to the stability, fabrication and properties of the nanomaterials. Hence, studying the interactions in the colloidal domain is of importance not only for their bio-medical applications but also for the improvement and betterment of many daily-use industrial products.

1.2 Interaction of Nanoparticles with Nonionic Surfactants

Surfactant adsorption involves the transfer of amphiphilic molecules from bulk solution to an interface. This transfer can cause drastic modifications in the hydrophobicity, surface charge, and other key properties of the interface, which in turn govern interfacial processes such as flocculation/dispersion, flotation, wetting, detergency, and corrosion inhibition [20–22]. Nonionic surfactants form an important class of amphiphiles, which are extensively involved in various biological and industrial processes [23]. Surfactant adsorption on hydrophilic and hydrophobic surfaces has been the focus of many recent studies [24–26]. Surfactant-surface interactions may include electrostatic, hydrogen bond and hydrophobic forces, and more specific interactions such as Lewis acid-base interactions. In the case of nonionic surfactants, the strength of interaction between the surfactant head groups and hydrophilic surface is considerably weaker than the coulomb interaction between an oppositely charged surfactant-surface pair [27]. In our specific case, the adsorption of ethoxylate surfactants (C_iE_j) on to a silica surface involves the formation of hydrogen bonds between the ether head groups of the C_iE_j molecule and the surface silanol (Si-OH) groups of silica. The hydrogen bonds formed can be either direct or mediated by bulk water [28]. The surfactant adsorption and its aggregate morphology depend on interaction energy (function of adsorption energy) between the ethoxylate head group of C_iE_j surfactant and silica surface [29]. The surface of silica can be modified by the addition of small molecules like alcohols and depending on net interaction potential between silica and surfactant, it can either attach or desorb from the silica surface. There have been many studies reported in literature, comprehending the adsorption of ethoxylate surfactants on a flat surface [30–32]. However, the factors affecting the adsorption on curved surfaces are still not well understood. In the thesis, we give a detailed account of the factors affecting the binding strength of $C_{12}E_5$ surfactant on spherical silica nanoparticles (positive curvature [33]) and in the nanopores of SBA-15 silica (negative curvature [33]).

Adsorption on silica nanoparticles: Silica nanoparticles and their composites with surfactants are extensively used in the field of oil recovery [34], foam stabilizations [35], sensors [36] etc. Hence, studying the interaction of nanoparticles with the surfactant molecules is of great practical relevance. In the work earlier done in our group [37], it was found that nonionic surfactants adsorb at silica in the form of small surface micelles rather than a uniform bilayer. In addition, it was also established that the morphology of the surfactant surface aggregate can be tuned by changing the curvature (size) of the silica nanoparticles [38, 39].

The studies mentioned above pose the obvious question *what are the implications of curvature effect on limiting surface excess of amphiphile?* To address this problem, we have studied the adsorption of $C_{12}E_5$ surfactants on silica nanoparticles of different sizes. From our adsorption isotherm measurements, we proved that the maximum amount of surfactant adsorbed per unit area of the silica surface decreases with the decrease in the particle size. Another question we have studied

is the effect of a surface modifier (lysine) on the surfactant binding affinity to silica nanoparticles. The transitions occurring in the surfactant aggregate structure with small additions of surface modifier were followed by Small Angle Neutron Scattering (SANS). The scattering study revealed that the addition of lysine forces a morphological transition of surfactant aggregates from discrete surface micelles attached to the particles to elongated (wormlike) micelles in bulk.

Adsorption in cylindrical pores: Silica materials with highly ordered mesopore structure have been employed in chromatography [40], drug delivery [41], and related applications [42]. The synthesis of these silica materials involves the use of surfactant mesophase as templates [43]. Nonionic polymer surfactants (e.g. PEO-PPO-PEO) are widely used in the synthesis of silica mesoporous materials; [44] their interaction with the oxide surface plays a vital role in determining the physical properties of the synthesized materials e.g. porosity, size, pore morphology etc [45, 46]. The surface aggregate morphology of a nonionic surfactant $C_{12}E_5$ in the pores of SBA-15 has been previously studied by our group [47]. In the earlier study it was proved that the surfactant forms discrete patches adhering to the pore-wall of SBA-15. A fundamental question that arises from the study is *Can we alter the surfactant aggregate morphology inside the pores?* As explained earlier, the morphology of the surfactant on a surface depends on the adsorption energy, which can be altered by the addition of some small molecules. In this project, we modulated the interaction of surfactant with the SBA-15 pore-wall by the addition of lysine as a modifier. The change in aggregate morphology inside the pores was followed by Small Angle Neutron Diffraction (SAND). Interestingly, we discovered that the addition of surface modifier causes $C_{12}E_5$ to desorb from the pore wall, but there exists a rather wide lysine concentration regime where the displacer is able to detach the surfactant patches from the pore wall but the surfactant still remains in the pores, forming elongated (rods or wormlike) structures.

Our SANS, SAND and adsorption measurements for the surfactant $C_{12}E_5$ for two silica materials with opposite surface curvature give conclusive evidence that highlights the effects of surface curvature (particle size) and surface modifier (lysine) on the adsorption of nonionic surfactant to curved silica surfaces.

1.3 Protein-Nanoparticle Interactions

Proteins are biopolymers made up of amino acid monomers arranged in specific geometries in three dimensional space. Proteins make up the bulk of the structural components of cells and play a key role in intra- and inter-cellular signaling [48]. Globular proteins are an important class of proteins and have more or less spherical shape, induced by their tertiary structure. Hydrophobic side-groups of globular proteins tend to be buried in the interior of the molecule, with most of their charged groups on the periphery of the protein. Globular proteins are relatively compact objects and are commonly treated as hard nanocolloids [48].

In the last decade, there has been an enormous increase in the availability of nanomaterials that have potential applicability in biomedical sciences [49, 50]. The use of nanomaterials for *in vivo* functions results in a direct contact between the synthetic material and the biological matter. Proteins are one of the major components of biological matter, and their interaction with foreign surface (nanomaterials) determines the response of a living cell against the incubated materials [51]. There have been many recent attempts to apprehend the interaction of nanomaterials with the biological entities [52–54], including proteins with solid surfaces [55, 56], but no conclusive generalization has been drawn, primarily because of the complexity of the nature of interactions involved [57–59]. Depending upon the nature of surfaces, proteins can either adhere to or get repelled from the substrate. Protein adsorption on a flat or a curved surface is a complex process in which the structural stability of a protein, the ionic strength and pH of the solution, and the hydrophobicity or hydrophilicity of the interacting surfaces are known to influence the protein binding to the given interface [60, 61]. The adsorption of proteins to nanoparticles not only brings about changes in secondary and tertiary structure of proteins, but also affects the surface properties and stability of the sorbent particle solution. Hence, the study of changes induced in nanoparticle dispersions by the protein adsorption is of great relevance in biotechnology and the biomedical field.

Protein adsorption on a surface is the net result of the various interactions between and within the system components, which include the sorbent surface, the protein molecules, the solvent (water) and any other solutes present such as low molecular mass ions [62]. The origin of these interactions include Lifshitz-van der Waals forces (i.e. dispersion, orientation and induction forces), Lewis acid-base forces (including hydrogen bond forces), electrostatic forces (including ion pairing) and more entropically based effects such as the hydrophobic effect (at least under ambient conditions) and internal packing (steric/excluded-volume) restrictions [63]. There have been many recent attempts to probe and understand the interactions between protein and adsorbent's surface [64, 65]. Daly et al. [66] studied the reorganization of lysozyme on a flat silica surface, using total internal reflection fluorescence, streaming current and optical reflectometry. It was concluded that lysozyme undergoes an irreversible reorientation to a configuration that places its most positively charged patch against the negatively charged silica surface. Neutron reflectometry was used to study the effect of solution pH on the structure of lysozyme adsorbed at a flat silica surface [67]. On the other hand, the understanding of protein interaction with small nanoparticles is rather limited. Vertegel et al. [68] have studied the influence of silica nanoparticle size on the deformation of the adsorbed lysozyme. It was concluded that with increasing size of the particles the curvature-induced protein structure deformation becomes more pronounced than on very small particles. In a separate study by Lundqvist et al. [69], similar results of the particle's curvature were obtained for the adsorption of human carbonic anhydrase on silica nanobeads.

As a part of this PhD project, we studied the interaction of globular proteins with silica nanoparticles from a colloid science point of view. Lysozyme and cytochrome C were chosen as model proteins. High structural stability of lysozyme and cytochrome C, makes them good models for “hard” proteins [70]. Spherical silica nanoparticles of 20 nm diameter with low polydispersity ($\approx 10\%$) were synthesized and characterized by the methods explained in Chap. 2. The amount of lysozyme bound to silica nanoparticles was determined by adsorption isotherms (Chap. 2) over a wide range of pH and dispersion salinity. A pronounced influence of pH and dispersion salinity was found on the maximum adsorption amount, indicating the important role of electrostatic interactions in these systems. Lysozyme adsorption on silica nanoparticles was accompanied by a protein-induced aggregation of silica nanoparticles. This aggregation was observed to be completely reversible with pH. A combination of analytical centrifugation, cryo-TEM and Small Angle X-ray Scattering (SAXS) was used to characterize the properties and structure of the hetero-aggregate over the pH range from the Iso-Electric Point (IEP) of the silica to the IEP of lysozyme. The aggregation behavior was also studied for a similar globular protein cytochrome C. SAXS and turbidity measurements of silica-cytochrome C composites at different pH show the different aggregation pH regimes. We propose that the observed differences are due to a more unsymmetrical distribution of surface charge on cytochrome C in comparison to lysozyme.

1.4 Supra-Colloidal Permanent Assembly of Microparticles

As discussed in the Sect. 1.3, silica nanoparticles were observed to form hetero-aggregates with oppositely charged proteins. This hetero-aggregation was non-directional and essentially random. Although the pH of the dispersion does allow some control over the aggregate morphology, a direct tuning of the aggregate structure was not possible in the protein/silica systems. Based on our protein-particle aggregation studies, the question arises *How it may be possible to control the morphology of a biparticle system exhibiting strongly attractive interaction*, i.e. to assemble an aggregating pair of positive and negative particles into long-range ordered arrays. To address this question, the effect of an external electric field on the hetero-aggregation of latex microspheres was studied. Micrometer sized particles were used in order to simplify the experimental characterization of the system.

Assembling colloidal particles is an active and challenging field of materials science. In the past decade, there have been a number of studies focusing on patterning of colloidal particles [71], primarily because of their potential applications in surface-coatings [72], nano-electronic devices [73], nanofluidic sieves [74] etc. Assembled linear structures of microparticles have been studied extensively in view of their potential application in microcircuits [75]. One

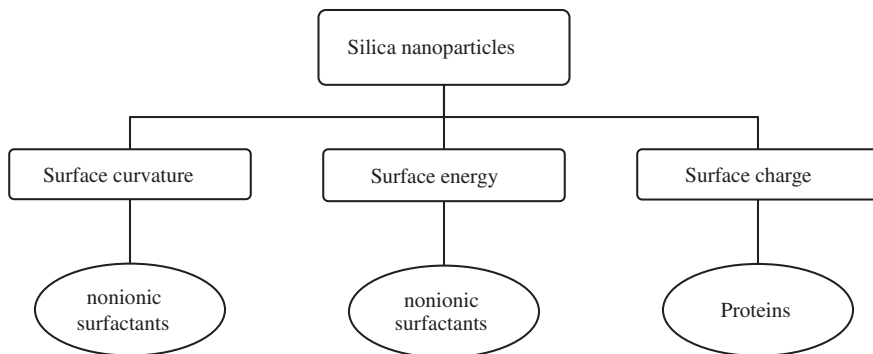
of the most widely used methods for drawing micro particles to linear chains is through the application of external fields (electric or magnetic) [76]. In the presence of external alternating electric field, dielectric particles (e.g. latex) tend to align into chain structures along the direction of applied field. This phenomenon is called Dielectrophoresis (DEP) [77]. In the presence of electric field, each dielectric particle has a net induced dipole moment and because of the dipole-dipole interaction between the particles, long range, highly ordered structures can be formed (for details see Chaps. 3 and 9). DEP-induced structures formed by equally charged particles are temporary and last only as long as external field is applied. The structure completely disintegrates upon removing the external field, primarily because of the surface charge-charge repulsion between the particles.

In order to exploit the field-induced chain formation for harvesting permanent structures, particles should remain in their assembled state even after the external electric field is switched off. For achieving such ‘*everlasting*’ chain structures, we used a bi-particle system, i.e. a dispersion of two types of colloidal particles having opposite surface charges. By replacing equally charged with oppositely charged micro-particles, we introduce a short-range strongly attractive potential between the particles. DEP is then used to drag the particles near the surface contact point, where the strong attractive electrostatic potential glues the particles together (i.e. forms hetero-aggregate) and the structures formed survive when the electric field is switched off.

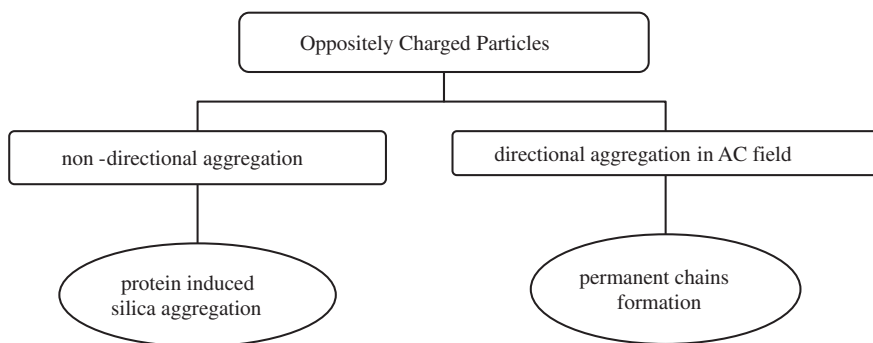
In addition to developing a novel experimental technique for synthesizing such permanent structures, we developed a theoretical approach based on a statistical model that predicts the chain length distribution for a given size ratio and number ratio of the positive and negative particles. On further development of this model and experimental technique, it should be possible to tune the chain length depending on the requirement of any industrial or biochemical process.

1.5 Overview

As outlined above, the focus of this PhD project was to accomplish a better understanding of the interaction phenomena of colloidal particles with soft matter. From a colloidal science point of view, many aspects of these interactions depend on surface curvature (particle size) and surface chemistry (surface energy and charge). Dispersions of silica nanoparticles were used as model systems for studying the effect of surface curvature (particle size) and surface energy on the adsorption of nonionic ethoxylate surfactant $C_{12}E_5$. On the other hand, surface charge on silica nanoparticle surface as well as the net charge of protein molecules are premium factors in controlling protein adsorption at nanoparticles and protein-induced nanoparticle aggregation.



As explained above, protein-nanoparticle aggregation was non-directional. In order to achieve a directional hetero-aggregation, a mixture of oppositely charged latex particles was forced to aggregate in the presence of an external electric field. In the thesis research we tailored the interactions between polystyrene colloidal particles and developed a novel approach for harvesting permanent linear chain structures.



1.6 Thesis Outline

This thesis is organized into five parts and the details and the contents of each part are given as follows:

1.6.1 Part-I: Introduction and Basics

After this general introduction to the subject area and the systems studied (Chap. 1), the main experimental methods used for studying the system, including the measurement of adsorption isotherms, small angle scattering and diffraction,

are summarized in Chap. 2. A detailed account of the analysis of the scattering data and the theory behind it is given in Chap. 3. This Chapter also explains the basics of particle chaining in an AC-electric field due to dielectrophoresis (DEP), and provides a detailed account of the statistical approach for predicting the length of permanent chain structure developed in this work.

1.6.2 Part-II: Curvature and Surface Energy Effects on the Interaction of Hydrophilic Silica with Nonionic Surfactant

In Chap. 4, we present the results of adsorption and SANS measurements aimed to study the effect of particle size and surface modification of silica nanoparticles on the self-assembly of surfactant $C_{12}E_5$. Chapter 5 deals with the complementary situation of the self-assembly of the surfactant in cylindrical nanopores of SBA-15 silica and the effects of a surface modifier on the binding tendency of the $C_{12}E_5$ surfactant to the pore-walls are also presented.

1.6.3 Part-III: Adsorptive and Aggregative Effects of Proteins on Silica Nanoparticles

Part III of the thesis presents the studies of the interactions between silica nanoparticles (20 nm) with two globular proteins, cytochrome C and lysozyme. Chapter 6 deals with the effects of pH on the adsorption of lysozyme to silica nanoparticles and the protein-induced aggregation of the silica particles. In direct continuation to these studies, Chap 7, focuses on the effect of ionic strength on the adsorption and the concomitant aggregation of the protein/silica system. Chapter 8 highlights the differences in the aggregation induced behavior observed for lysozyme and cytochrome C with silica.

1.6.4 Part-IV: Field Directed Assembly of Hetero-Aggregating Microparticles

Part IV of the thesis reports formation of permanent long chains made up of positive and negatively charged latex particles. In Chap. 9 we demonstrate how the hetero-aggregation phenomenon and DEP can be combined to assemble permanent linear structures. We provide a complete characterization of the chains formed for two different particle size ratios and different number ratios of the positive and negative particles. We also present an analysis of the data according to a new statistical model.

1.6.5 Part-V: Summary and Outlook

To conclude, a short summary of the work is given which indicates how the different projects studied address and contribute to the better understanding of the colloidal interactions. We also propose an outlook of the projects to highlight the possible extension and applications of the studied projects.

References

1. Levine IN (2001) Physical chemistry, vol 5. Tata McGraw-Hill, USA
2. Martínez AG, Barbosa S, Santos IP, Marzán LML (2011) Nanostars shine bright for you: colloidal synthesis, properties and applications of branched metallic nanoparticles. *Curr Opin Colloid Interface Sci* 16:118
3. Henglein A (1861) Small-particle research: physicochemical properties of extremely small colloidal metal and semiconductor particles. *Chem Rev* 1989:89
4. Coelho MC, Torrao EN, Grácio J (2012) Nanotechnology in automotive industry: research strategy and trends for the future—small objects, big impacts. *J Nanosci Nanotechnol* 12:6621
5. Lu AH, Salabas EL, Schüth F (2007) Magnetic nanoparticles: synthesis, protection, functionalization, and application. *Angew Chem Int Ed* 46:1222
6. Weiss J, Takhistov P, McClements J (2006) Functional materials in food nanotechnology. *J Food Sci* 71:R107
7. Mao Y, McClements DJ (2012) Fabrication of viscous and paste-like materials by controlled heteroaggregation of oppositely charged lipid droplets. *Food Chem* 134:872
8. Liu GY, Wang JM, Xia Q (2012) Application of nanostructured lipid carrier in food for the improved bioavailability. *Eur Food Res Technol* 234:391
9. Patel A, Velikov KP (2011) Colloidal delivery systems in foods: A general comparison with oral drug delivery, *LWT-Food. Sci Technol* 44:1958
10. Osaka T, Matsunga T, Nakanishi T, Arakaki A, Niwa D, Iida H (2006) Synthesis of magnetic nanoparticles and their application to bioassays. *Anal Bionanal Chem* 384:593
11. Xiong HM, Xu Y, Ren QG, Xia YY (2008) Stable aqueous ZnO@ polymer core-shell nanoparticles with tunable photoluminescence and their application in cell imaging. *J Am Chem Soc* 130:7522
12. Gao J, Gu H, Xu B (2009) Multifunctional magnetic nanoparticles: design, synthesis, and biomedical applications. *Acc Chem Res* 42:1097
13. Colvin VL, Kulinowski KM (2007) Nanoparticles as catalysts for protein fibrillation. *Proc Natl Acad Sci* 104:8679
14. Farokhzad OC, Langer R (2009) Impact of nanotechnology on drug delivery. *ACS Nano* 3:16
15. Rogach AL, Eychmüller A, Hickey SG, Kershaw SV (2007) Infrared-emitting colloidal nanocrystals: synthesis, assembly, spectroscopy, and applications. *Small* 4:536
16. Prevo BG, Hon EW, Velev OD (2007) Assembly and characterization of colloid-based antireflective coatings on multicrystalline silicon solar cells. *J Mater Chem* 17:791
17. Gudiksen MS, Lauthon LJ, Wang J, Smith DC, Lieber CM (2002) Growth of nanowire superlattice structures for nanoscale photonics and electronics. *Nature* 415:617
18. Thelander C, Mårtensson T, Björk MT, Ohlsson BJ, Larsson MW, Wallenberg LR, Samuelson L (2003) Single-electron transistors in heterostructure nanowires. *Appl Phys Lett* 83:2052
19. Terray A, Oakey J, Marr DWM (2002) Fabrication of linear colloidal structures for microfluidic applications. *Appl Phys Lett* 81:1555
20. Zhang R, Somasundaran P (2006) Advances in adsorption of surfactants and their mixtures at solid/solution interfaces. *Adv Colloid Interface Sci* 123–126:213

21. Xiao L, Xu GY, Zhang ZQ, Wang YB, Li GZ (2003) Adsorption of sodium oleate at the interface of oil sand/aqueous solution. *Colloids Surf A* 224:199
22. Holmberg K, Shah DO, Schwuger MJ (2002) *Handbook of applied surface and colloid chemistry*. Wiley, New York
23. Jiao J (2008) Polyoxyethylated nonionic surfactants and their applications in topical ocular drug delivery. *Adv Drug Deliver Rev* 15:1663
24. Soria-Sánchez M, Maroto-Valiente A, Guerreo-Ruiz A, Nevskaja DM (2010) Adsorption of non-ionic surfactants on hydrophobic and hydrophilic carbon surfaces. *J Colloid Interface Sci* 343:194
25. Hunter N, Wanless EJ, Jameson GJ, Pugh RJ (2009) Non-ionic surfactant interactions with hydrophobic nanoparticles: impact on foam stability. *Colloids Surf A* 347:81
26. Griffith JC, Alexander AE (1967) Equilibrium adsorption isotherms for wool/detergent systems: I. The adsorption of sodium dodecyl sulfate by wool. *J Colloid Interface Sci* 25:311
27. Somasundaran P, Krishnakumar S (1997) Adsorption of surfactants and polymers at the solid-liquid interface. *Colloids Surf A* 123–124:491
28. Trems P, Denoyel R (1993) Conformation of poly (ethylene glycol) polymers at the silica/water interface: a microcalorimetric study. *Langmuir* 9:519
29. Levitz P, Damme HV (1986) Fluorescence decay study of the adsorption of nonionic surfactants at the solid-liquid interface. 2. Influence of polar chain length. *J Phys Chem* 90:1302
30. Tiberg F (1996) Physical characterization of non-ionic surfactant layers adsorbed at hydrophilic and hydrophobic solid surfaces by time-resolved ellipsometry. *J Chem Soc, Faraday Trans* 92:531
31. Penfold J, Staples E, Tucker I (2002) On the consequences of surface treatment on the adsorption of nonionic surfactants at the hydrophilic silica-solution interface. *Langmuir* 18:2967
32. Grant LM, Tiberg F, Ducker WA (1998) Nanometer-scale organization of ethylene oxide surfactants on graphite, hydrophilic silica, and hydrophobic silica. *J Phys Chem B* 102:4288
33. Ouyang G, Wang X, Yang GW (2009) Surface energy of nanostructural materials with negative curvature and related size effects. *Chem Rev* 109:4221
34. Le NYT, Pham DK, Le KH, Nguyen PT (2011) Design and screening of synergistic blends of SiO₂ nanoparticles and surfactants for enhanced oil recovery in high-temperature reservoirs. *Adv Nat Sci Nanosci Nanotechnol* 2:035013
35. Dickinson E, Ettelaie R, Kostakis T, Murray BS (2004) Factors controlling the formation and stability of air bubbles stabilized by partially hydrophobic silica nanoparticles. *Langmuir* 20:8517
36. Latterini L, Amelia M (2009) Sensing proteins with luminescent silica nanoparticles. *Langmuir* 25:4767
37. Lugo DM (2010) Adsorption of surfactants on colloidal silica: effects of surface curvature on the structure of surface aggregates. Ph.D. thesis, Technische Universität, Berlin, Germany
38. Lugo DM, Oberdisse J, Karg M, Schweins R, Findenegg GH (2009) Surface aggregate structure of nonionic surfactants on silica nanoparticles. *Soft Matter* 5:2928
39. Lugo DM, Oberdisse J, Lapp A, Findenegg GH (2010) Effect of nanoparticle size on the morphology of adsorbed surfactant layers. *J Phys Chem B* 114:4183
40. Gallis KW, Araujo JT, Duff KJ, Moore JG, Landry CC (1999) The use of mesoporous silica in liquid chromatography. *Adv Mater* 17:1452
41. Chen JF, Ding HM, Wang JX, Shao L (2004) Preparation and characterization of porous hollow silica nanoparticles for drug delivery application. *Biomaterials* 25:723
42. Slowing II, Escoto JLV, Wu CW, Lin VSY (2008) Mesoporous silica nanoparticles as controlled release drug delivery and gene transfection carriers. *Adv Drug Delivery Rev* 60:1278
43. Huo Q, Margolese DI, Stucky GD (1996) Surfactant control of phases in the synthesis of mesoporous silica-based materials. *Chem Mater* 8:1147
44. Bagshaw SA, Prouzet E, Pinnavaia TJ (1995) Templating of mesoporous molecular sieves by nonionic polyethylene oxide surfactants. *Science* 269:1242
45. Kuang D, Brezesinski T, Smarsly B (2004) Hierarchical porous silica materials with a trimodal pore system using surfactant templates. *J Am Chem Soc* 126:10534
46. Wan Y, Shi Y, Zhao D (2007) Designed synthesis of mesoporous solids via nonionic-surfactant-templating approach. *Chem Commun* 9:897

47. Shin TG (2010) The self-assembly of surfactants in ordered mesoporous silica studied by neutron scattering. Ph.D. thesis, Technische Universität, Berlin, Germany
48. Poon WCK (2006) Soft condensed matter physics in molecular and cell biology. Taylor & Francis Group, USA
49. De M, Ghosh PS, Rotello VM (2008) Applications of nanoparticles in biology. *Adv Mater* 20:4225
50. Sarikaya M, Tamerler C, Jen AKY, Schulten K, Baneyx F (2003) Molecular biomimetics: nanotechnology through biology. *Nat Mater* 2:577
51. Lynch I, Salvati A, Kenneth DA (2009) Protein-nanoparticle interactions: What does the cell see? *Nat Nanotechnol* 4:546
52. Niemeyer CM (2001) Nanoparticles, proteins, and nucleic acids: biotechnology meets materials science. *Angew Chem Int Ed* 40:4128
53. Cedervall T, Lynch I, Lindman S, Berggard T, Thulin E, Nilsson H, Dawson KA, Linse S (2007) Understanding the nanoparticle-protein corona using methods to quantify exchange rates and affinities of proteins for nanoparticles. *Proc Natl Acad Sci* 104:2050
54. Verma A, Stellacci F (2010) Effect of surface properties on nanoparticle-cell interactions. *Small* 6:12
55. Cohavi O, Corni S, Rienzo RD, Felice RD, Gottschalk KE, Hoefling M, Kokh D, Molinari E, Schreiber G, Vaskevich A, Wade RC (2010) Protein-surface interactions: challenging experiments and computations. *J Mol Recognit* 23:259
56. Rabe M, Verdes D, Seeger S (2011) Understanding protein adsorption phenomena at solid surfaces. *Adv Colloid Interface Sci* 162:87
57. Lynch I, Dawson KA (2008) Protein-nanoparticle interactions. *Nano Today* 3:40
58. Klein J (2007) Probing the interactions of proteins and nanoparticles. *Proc Natl Acad Sci* 104:2029
59. Li N, Zeng S, He L, Zhong W (2010) Probing nanoparticle-protein interaction by capillary electrophoresis. *Anal Chem* 82:7460
60. Pasche S, Vörös J, Griesser HJ, Spencer ND, Textor M (2005) Effects of Ionic strength and surface charge on protein adsorption at PEGylated surfaces. *J Phys Chem B* 109:17545
61. Haynes CA, Norde W (1994) Globular proteins at solid/liquid interfaces. *Colloids Surf B* 2:517
62. Norde W, Lyklema J (1978) The adsorption of human plasma albumin and bovine pancreas ribonuclease at negatively charged polystyrene surfaces: V. Microcalorimetry. *J Colloid Interface Sci* 66:295
63. Huang R, Carney RP, Stellacci F, Lau BLT (2013) Protein-nanoparticle interactions: the effects of surface compositional and structural heterogeneity are scale dependent. *Nanoscale* 5:6928
64. Roach P, Farrar D, Perry CC (2004) Interpretation of protein adsorption: surface-induced conformational changes. *J Am Chem Soc* 127:8168
65. Monopoli MP, Walczyk D, Campbell A, Elia G, Lynch I, Bombelli FB, Dawson KA (2011) Physical-chemical aspects of protein corona: relevance to in vitro and in vivo biological impacts of nanoparticles. *J Am Chem Soc* 133:2525
66. Daly SM, Przybycien TM, Tilton RD (2003) Coverage-dependent orientation of lysozyme adsorbed on silica. *Langmuir* 19:3848
67. Su TJ, Lu JR, Thomas RK, Cui ZF, Penfold J (1998) The effect of solution pH on the structure of lysozyme layers adsorbed at the silica-water interface studied by neutron reflection. *Langmuir* 14:438
68. Vertegeel AA, Siegel RW, Dordick JS (2004) Silica nanoparticle size influences the structure and enzymatic activity of adsorbed lysozyme. *Langmuir* 20:6800
69. Lundqvist M, Sethson I, Jonsson BH (2004) Protein adsorption onto silica nanoparticles: conformational changes depend on the particles' curvature and the protein stability. *Langmuir* 20:10639
70. Norde W, Favier JP (1992) Structure of adsorbed and desorbed proteins. *Colloid Surf* 64:87
71. Vutukuri HR, Stiefelhagen J, Vissers T, Imhof A, van Blaaderen A (2012) Bonding assembled colloids without loss of colloidal stability. *Adv Mater* 24:412
72. Prevo BG, Hon EW, Velev OD (2007) Assembly and characterization of colloid-based antireflective coatings on multicrystalline silicon solar cells. *J Mater Chem* 17:791

73. Vanmaekelbergh D (2011) Self-assembly of colloidal nanocrystals as route to novel classes of nanostructured materials. *Nano Today* 6:419
74. Zeng Y, Harrison DJ (2007) Self-assembled colloidal arrays as three-dimensional nanofluidic sieves for separation of biomolecules on microchips. *Anal Chem* 79:2289
75. Hermanson KD, Lumsdon SO, Williams JP, Kaler EK, Velev OD (2001) Dielectrophoretic assembly of electrically functional microwires from nanoparticle suspensions. *Science* 294:1082
76. Velev OD, Gupta S (2001) Materials fabricated by micro- and nanoparticle assembly—The challenging path from science to engineering. *Adv Mater* 21:1897
77. Velev OD, Bhatt KH (2006) On-chip micromanipulation and assembly of colloidal particles by electric fields. *Soft Matter* 2:738

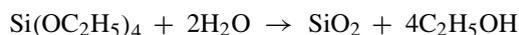
Chapter 2

Methods

2.1 Synthesis and Characterization of Silica Nanoparticles

2.1.1 Synthesis

Silica nanoparticles of diameter 12, 21 and 42 nm were prepared by the hydrolysis of tetraethyl orthosilicate $\text{Si}(\text{OC}_2\text{H}_5)_4$ (TEOS) with water. The reaction taking place is a sol-gel process and is shown below:



The reaction proceeds by hydrolysis of TEOS to $\text{Si}(\text{OH})_4$ and a series of condensation reactions that convert the orthosilicic acid into a mineral-like solid via the formation of Si-O-Si linkages [1]. Reaction was carried out in the presence of the basic amino acid lysine as reported by Davis et al. [2] and Thomassen et al. [3] In a typical synthesis 0.51 g of lysine monohydrate was dissolved in 102 mL milli-Q water in a 250 mL round bottom flask (RB). After equilibration at 60 °C for 1 h, 16 mL of TEOS was added dropwise and the reaction mixture was kept in the reaction vessel at an optimized temperature and stirring rate. The resulting silica dispersion was dialyzed to remove unreacted TEOS and reaction by-products, using dialysis membranes with a molecular-weight cut-off at 14 kDa. Dialysis was carried for 1 week with changing of milli-Q water twice per day. Bigger aggregates of silica formed during the reaction were removed from the dialyzed dispersion by a series of filtration steps. Filtration was done with 5 μm followed by 0.8 μm and eventually using 0.22 μm filters. In order to avoid aggregation of silica, pH was adjusted to ≈ 9 and the dispersion was stored at 8 °C. The particle size was tuned solely by optimizing the stirring speed and the adjustment of the temperature of the reaction mixture. Since the different sizes of silica nanoparticles were prepared by altering only the physical conditions, the surface chemistry (surface charge density) presumably remains unaltered. The resulting silica nanoparticles were characterized for their size and polydispersity by Small Angle X-ray Scattering (SAXS), for their surface charge by zeta potential and for their specific surface area by nitrogen adsorption.

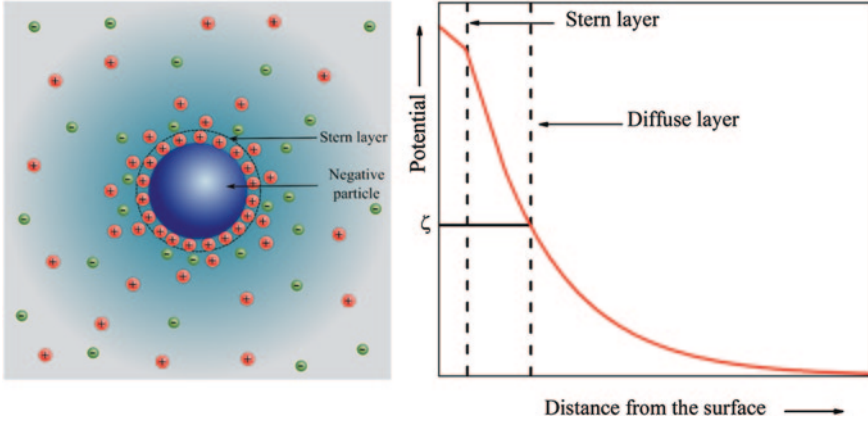


Fig. 2.1 Diagram showing the distribution of the ions around the negatively charged particle, indicating the presence of a shell of strongly bound counter ions (stern layer) and weakly bound layer called the diffuse layer

2.1.2 Zeta Potential

The surface charge of a colloidal particle in aqueous media is balanced by an equal number of oppositely charged counter ions. Some of the counter ions are bound to the surface within, the so called *Stern* or *Helmholtz layer*, while others form an atmosphere of loosely bound ions further away from the surface known as the *diffuse double layer* [4]. Within the diffuse layer there is a notional boundary, inside which the ions move together with the particle, whereas the ions outside this boundary do not travel with the particle. This boundary is called the surface of hydrodynamic shear or *slipping plan* [5] (Fig. 2.1). The potential that exists at this boundary is known as the *zeta potential*. It is an electric potential in the interfacial double layer at the location of the slipping plane versus a point in the bulk fluid away from the interface [6]. In other words, zeta potential is the potential difference between the bulk dispersion medium and the stationary layer of fluid attached to the particle's surface. Zeta potential is not measurable directly but it can be calculated from electrophoretic mobility (μ_e) using the Henry equation

$$\zeta = \frac{3\eta\mu_e}{2\epsilon f(\kappa R)}, \quad (2.1)$$

where ζ is the zeta potential of the particle with radius R , η and ϵ are the viscosity and dielectric constant of the medium respectively and $f(\kappa R)$ is called the Henry's function. The Henry's function depends on particle size and the ionic strength of the dispersion via the Debye length ($1/\kappa$)

$$1/\kappa = \sqrt{\frac{\epsilon_0 \epsilon k_B T}{2N_A e^2 I}} \quad (2.2)$$

where ε_0 is the permittivity of free space, ε is the Dielectric constant, k_B is Boltzmann constant; T is the temperature in K, N_A being the Avogadro number, e is the elementary electronic charge and I is the ionic strength of the dispersion.

The electrophoretic mobility of a particle can be determined by the application of an electric field across the dispersion. The charged particles suspended in the electrolyte are attracted towards the electrode of opposite charge. Viscous forces acting on the particles tend to oppose this movement. When a steady velocity v , is reached, the electrophoretic mobility is given by $\mu_e = v/E$, where E is the electric field strength. The Henry's function $f(\kappa R)$ acquires the value of 1.5 in the limit $\kappa R \gg 1$, i.e. large particles and high ionic strength (Smoluchowski approximation), whereas $f(\kappa R) = 1$ in the limit $\kappa R \ll 1$, i.e. small particles in low ionic strength media (Hückel approximation). Measurements of the electrophoretic mobility were carried out with a Zetasizer Nano ZS (Malvern Instruments, UK) operating with a 4 mW HeNe laser (633 nm) and a light scattering detector positioned at 90° and a temperature control jacket for the cuvette. The sample was equilibrated for 2 min at 25°C before starting the measurements. Three measurements, each consisting of 30 runs were performed for each sample, and an average of the measurements was used for further reference.

2.1.3 Nitrogen Adsorption

The surface area of the nanoparticles was determined by nitrogen adsorption at 77 K. The adsorption isotherm was then interpreted on the basis of BET model of multilayer gas adsorption [7]. The surface of a solid is regarded as an array of equivalent adsorption sites. As in *Langmuir* model of monolayer adsorption, each of these sites can accommodate one adsorbed molecule in direct contact with the surface. However, in BET model each occupied site can act, in turn as a site for molecules adsorbed in the second layer, and so on for infinite number of higher layers. The resulting BET model can be written in the form

$$\frac{p/p_0}{V(1-p/p_0)} = \frac{1}{V_m c} + \frac{c-1}{V_m c} (p/p_0) \quad (2.3)$$

here V is the amount of adsorbed gas expressed as ideal gas volume at standard temperature and pressure (V_{STP}), V_m is respective volume of a complete monolayer adsorbed gas quantity, p is the equilibrium pressure, p_0 is saturation vapor pressure, the term p/p_0 is called the relative vapor pressure and c is the BET constant, $c = e^{\Delta E/RT}$, where ΔE is the difference between the heat of adsorption of first layer and the higher layers. The derivation of the BET equation can be found elsewhere [7]. The relation presented in Eq. 2.3 can be plotted with $\frac{p/p_0}{V(1-p/p_0)}$ as ordinate and p/p_0 as abscissa resulting into a straight line. This representation is called BET plot. In many cases, the linear behavior of the equation is maintained for $0.05 < p/p_0 < 0.3$. The slope of the straight line is equal to $1/V_m$ and is related to the specific surface area (a_s) by the following relation

$$a_s = \frac{a_m V_m N_A}{V_{STP}} \quad (2.4)$$

where a_m is the average area occupied by a molecule of adsorbate ($a_m = 0.162 \text{ nm}^2$ for N_2), N_A is the Avogadro constant and V_{STP} is the volume occupied by 1 mol of the gas at STP ($V_{STP} = 22.414 \text{ L/mol}$). In our work, we have measured the adsorption isotherms of nitrogen at 77 K for the synthesized silica materials by gas volumetry using a Micromeritics Gemini III 2,375 Volumetric Surface Analyzer. Before the gas adsorption measurements, the silica material was dried and outgassed at 393 K for 1 h under vacuum. For nitrogen adsorption isotherm measurements, Micromeritics sample holder with thermal isolation by Dewar vessel containing liquid nitrogen was used.

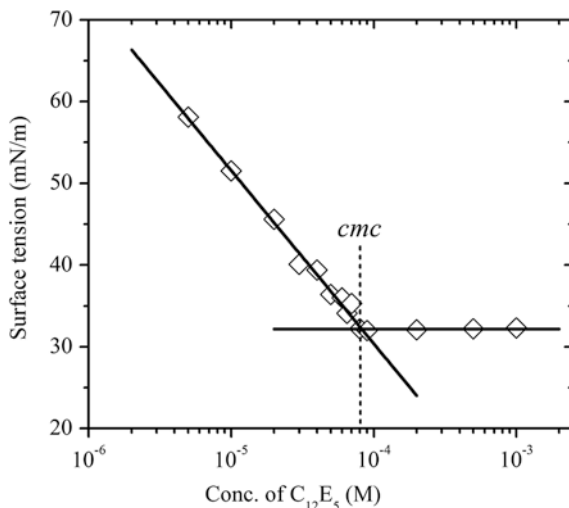
2.2 Adsorption at Solid/Liquid Interface

Adsorption phenomena take place whenever two immiscible phases are brought into direct contact with each other, resulting in the excess accumulation of either component in the interfacial region. The process of transfer of the component from bulk to the surface continues until a state of adsorption equilibrium is reached [8]. Adsorption from solution onto a solid surface depends on the composition of the solution and is expressed in terms of an *adsorption isotherm*, where amount adsorbed (n_{ads}) is expressed as the function of equilibrium concentration (i.e. free adsorbate concentration) in the bulk (c_{eq}). In our studies, we determined adsorption isotherms by solvent depletion method. In a typical experimental scheme, a certain concentration of adsorbate (c_0) (protein or surfactant) was added to the dispersion containing a fixed amount of silica nanoparticles and the mixture obtained was equilibrated for 24 h on a multiple axel rotor. After complete equilibrium was reached, nanoparticles with the adsorbed protein (or surfactant) were removed from the dispersion by centrifugating the samples for 2 h at $\approx 21,000 \text{ g}$ (15,000 RPM) in a Hettich Universal 320R centrifugation equipment fitted with 1420-A sample holder. The supernatant was carefully isolated from the centrifugated mixture and the amount of unadsorbed protein (or surfactant) in the supernatant was determined by the methods described in the following sections. After the precise determination of the residual equilibrium concentration c_{eq} the amount adsorbed was calculated as $n_{ads} = V(c_0 - c_{eq})$, where V is the volume of dispersion and c_0 is the total amount of adsorbent added to silica dispersion. The surface concentration (excess) of the adsorbed material is then given by Eq. 2.5 [9, 10]

$$\Gamma = \frac{(c_0 - c_{eq})V}{a_s m} \quad (2.5)$$

here Γ is the surface excess concentration (expressed in mol/m^2), c_0 , c_{eq} are the concentration before and after equilibration with the solid (in mol/L), V is the total

Fig. 2.2 Surface tension variation of aqueous solution of $C_{12}E_5$ surfactant at different bulk concentrations, the intersection point of the linear fit for the two regions of surface tension curve gives the value of cmc



volume of solution (in L), m is the total mass (in g) and a_s is the specific surface area of the particles (in m^2/g) (Sect. 2.1.3). Different initial amounts of adsorbate (c_0) were added to the nanoparticle dispersion in order to access different surface concentration regimes, and thus to obtain complete adsorption isotherm.

2.2.1 Surfactant Adsorption

The adsorption isotherm of $C_{12}E_5$ on silica nanoparticles was determined by the procedure explained in the previous section. Surface tension was used to determine the equilibrium surfactant concentration (c_{eq}). Surface tension measurements were made by the Du Noüy ring method using a Krüss K11 Tensiometer. The Platinum-Iridium ring of 20 mm diameter was used to examine the pulling force (and hence surface tension) from the liquid-air interface for the determination of surface tension of solution. The ring was completely dried before each measurement and all the samples were equilibrated at 25 °C for 5 min before the measurement. Three consecutive readings were taken and their mean value was used as the final surface tension of the solution. A surface tension curve for known concentration of $C_{12}E_5$ surfactant is shown in Fig. 2.2, the dashed line indicates the value of critical micelle concentration (cmc). The region of linear decay in the surface tension with surfactant concentration $< cmc$, was used as the reference, and the linear fit to the points was used as the calibration values for determining unknown concentrations of surfactant. A typical adsorption isotherms curve for nonionic surfactant ($C_{12}E_5$) on silica surface is shown in Fig. 2.3a. The adsorption isotherm of nonionic surfactants on silica surface shows an S-shaped curve [11, 12] which is contradistinct from the *Langmuir* model of adsorption (Fig. 2.3b).

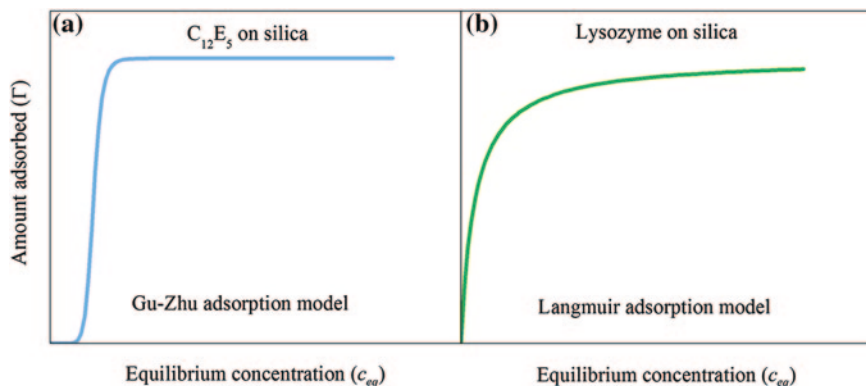
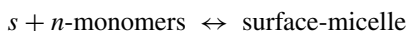


Fig. 2.3 Generalized example of two different types of adsorption isotherms on silica nanoparticles. **a** Adsorption isotherm of $C_{12}E_5$ on silica, it presents an S-type curve and can be represented by Gu-Zhu model [14]. **b** Lysozyme adsorption isotherm at silica surface, it shows a very strong affinity of adsorption on silica surface and can be represented by Langmuir adsorption model

For nonionic ethoxylate surfactants, because of the presence of weak non-electrostatic interactions between the ethoxylate surfactant head groups and silica surface silanol groups, the adsorption isotherms do not show the second plateau region as is the case with ionic surfactants [13] (not shown here). The adsorption behavior of nonionic surfactant has been well explained by Zhu et al. [14]. According to the proposed model, the aggregation of n monomers of nonionic surfactant on a surface site (s) forms a surface-micelle, where n is the nominal aggregation number of the surface-micelle.

At equilibrium,



By applying the mass action model to the above assumption, the surface excess concentration (Γ) of nonionic surfactant is given by the following Eq. 2.6.

$$\Gamma = \frac{\Gamma_m K c_{eq}^n}{1 + K c_{eq}^n} \quad (2.6)$$

where Γ_m is the maximum surface concentration, c_{eq} is the equilibrium concentration of surfactant, K is the adsorption constant and n is the mean aggregation number. This equation was used for fitting the experimental data points in (Chap. 4) and hence determining the Γ_m and n values.

2.2.2 Protein Adsorption

Adsorption isotherms of proteins (lysozyme or cytochrome C) on silica nanoparticles were measured at different pH and ionic strength in 50 mM 2-(N-morpholino)

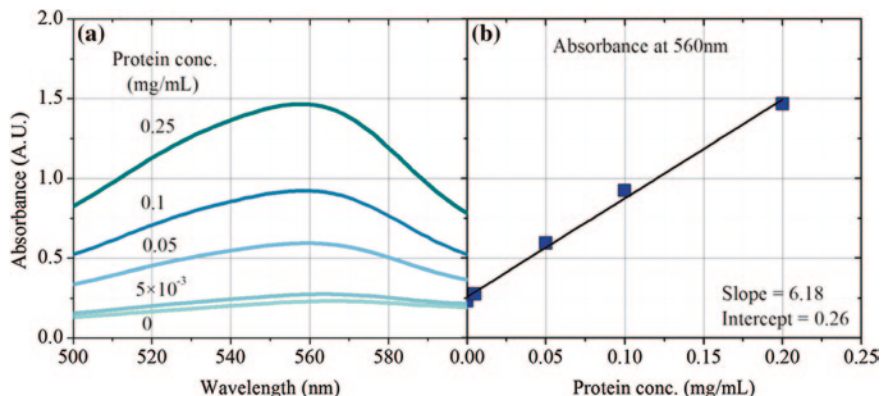


Fig. 2.4 **a** Absorbance variation for samples treated with BCA protein assay at 60 °C for 2 h and having different protein content indicated by the numbers. **b** The change in the absolute absorbance values at 560 nm; the scattered points are the measured data points (shown in **a**) and *solid line* is the linear fit to the data points

ethanesulfonic acid (MES) or 2-(Bis(2-hydroxyethyl)amino)acetic acid (BICINE) buffer. Organic buffers were used with the purpose of keeping the ionic concentration caused by buffers to a minimum. The free protein concentration in the supernatant obtained after centrifugating out silica with adsorbed protein was determined by measuring its absorbance at $\lambda = 280$ nm using a Varian Cary UV-vis spectrophotometer. For precise determination of protein concentration at $\text{pH} > 7$, the BCA protein assay kit was used. 0.15 ml of the protein sample was incubated with 3 mL of working reagent for 2 h at 60 ± 1 °C, and the absorbance at $\lambda = 560$ nm was measured. BCA uses reduction of Cu^{+2} to Cu^{+} by protein in an alkaline medium (biuret reaction) with the highly sensitive and selective colorimetric detection of Cu^{+} using a unique reagent containing bicinchoninic acid [15]. At first, a calibration curve with known protein amounts was obtained. Based on this calibration curve, the unknown protein concentration was determined. Figure 2.4a shows the typical UV-vis measured for different known concentrations of the protein, The calibration curve resulting from the measurements is shown in Fig. 2.4b. The linear fit to the experimental points gives a slope m with an intercept of b . Hence equilibrium concentration of protein is given by Eq. 2.7.

$$c_{eq} = \frac{(A_{560} - b)}{m} \quad (2.7)$$

where A_{560} is the absorbance of the assay-protein complex, $b = 0.26$ and $m = 6.18$.

The adsorption isotherms obtained were of the type shown in Fig. 2.4b. This type of isotherm is typical for strong monolayer adsorption and can be represented by the *Langmuir* adsorption model. According to this model there exists equilibrium between empty surface sites (s), free particles (p) and sites occupied by a single particle (sp), i.e. $s + p \leftrightarrow sp$. Surface of protein at any point can be estimated by the above model using the Langmuir equation [16]

$$\Gamma = \frac{\Gamma_m K c_{eq}}{1 + K c_{eq}} \quad (2.8)$$

where Γ is the surface (excess) concentration at any point on adsorption isotherm, Γ_m is the maximum surface concentration, c_{eq} is the equilibrium concentration in the solution and K is the Langmuir equilibrium constant. Its value depends on the strength of adsorption, i.e., the binding affinity (or energy) of the sorbent to the substrate. Comparing Eqs. 2.6 and 2.8 the only difference between the two model isotherms is the presence of the aggregation number ‘ n ’ in Eq. 2.6, which accounts for rapid increase in adsorption beyond a specific onset concentration.

2.3 Turbidity and Analytic Centrifugation

As will be discussed in Chaps. 6 and 7, the samples of silica dispersion containing lysozyme in a pH range 4–9 causes a lysozyme-mediated silica aggregation. In order to study the evolution and nature of these aggregates as a function of pH, turbidity measurements were made. The turbidity τ_c of the dispersions was determined from their optical transmittance (T) at wavelength 800 nm with the relation $\tau_c = (\log_{10}(1/T))/lc$, where c is the mass concentration of the silica in the dispersion, and l is the optical path length. The transmittance of the samples was determined in 1 mm quartz cuvettes using a UV-vis spectrophotometer.

Another newly developed technique used for the characterization of aggregate morphology is the analytical photo-centrifuge. It allows speeding up the sedimentation of dispersions by the application of centrifugal force. The rate of sedimentation of nanoparticles or aggregates in the centrifugal field is dependent on their size and morphology. Hence monitoring sedimentation by measuring the intensity of the light transmitted through the sample can provide detailed information about the aggregate structure. As described elsewhere [17, 18], in Space and Time Extinction Profiles (STEP)-technology, the sample is measured simultaneously over its full sample length as a function of time as shown in Fig. 2.5. For a given type of sample cells the position corresponds to a defined sample volume, the relationship between position and sample volume can be established by calibration. This allows to directly determine separate phase volumes and to calculate packing densities.

In the present work, the analytical centrifugation measurements were carried out in cooperation with Prof. D. Lerche and Dr. T. Sobisch at LUM Berlin. The sedimentation kinetics and phase volume of the silica-protein hetero-flocculate, and the size distribution of the flocculated particles was derived from the progression of transmission profiles. The sedimentation kinetics was measured at a centrifugal acceleration of 36 g (bottom position). Subsequently, the compression kinetics of the sediments formed was obtained at 2,300 g. The size distributions were determined in a separate measurement in which the centrifugal acceleration was gradually increased from 13 to 2,300 g [19].

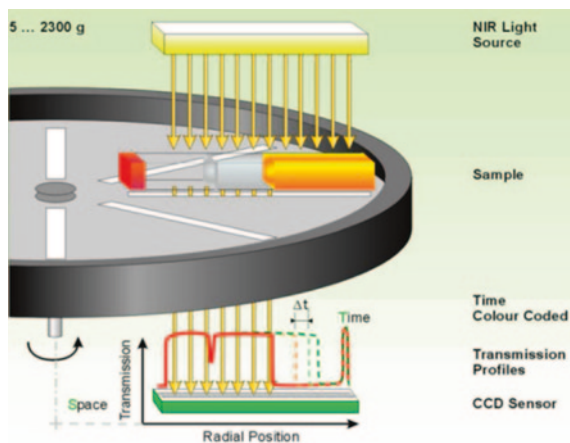


Fig. 2.5 Experimental setup of the multisample analytical photocentrifuge. Parallel NIR-light is passed through the sample cells and the distribution of local transmission is recorded at preset time intervals over the entire sample length. (Figure reproduced with the permission of LUM, Berlin, GmbH)

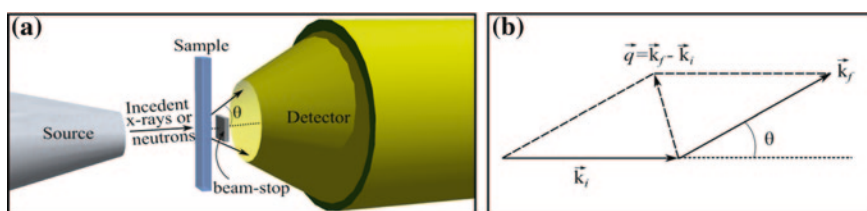


Fig. 2.6 **a** Experimental setup for the small angle scattering experiment, where the incident beam from the source (neutron or X-ray) is projected on the sample and the scattered beam is monitored by the detector in line with the incident beam. **b** Schematic illustration of a neutron scattering geometry and vector relations

2.4 Small Angle Scattering

Scattering is the phenomenon where an incident radiation (light, X-rays or neutrons) is forced to deviate from a straight linear path when passing through a medium (solid, liquid or gas). In general, when an electromagnetic wave is incident on a system then the constituents of the system emit secondary wavelets in all the directions. The overall scattering pattern is then resulting from the superposition and interference of all the secondary wavelets. A typical set up for small angle instrument is shown in the Fig. 2.6a. Here, a collimated X-ray or neutron beam is incident on the sample and the pattern arising from the scattering was observed by the detector placed in line with the incident beam. Beam-stop is placed in order to avoid the high intensity direct beam, which could lead to damage of detector.

In my PhD work, Small Angle Neutron Scattering (SANS) and Small Angle X-ray Scattering (SAXS) were used to study the structural features of hard and soft matter in the nanoparticle dispersions. The principle of the two techniques is exactly the same but important differences between SANS and SAXS result from the different nature of the scattered radiation. Neutrons are neutral elementary subatomic particles which interact with the atomic nuclei of the sample. On the other hand, X-rays interact with the electron shell of the atoms and thus gives information about the electron density in different parts of the sample. In both cases, it is the elastic, coherent scattering of X-rays/neutrons that gives rise to small-angle scattering. Coherent scattering is “in phase” and thus can contribute to small-angle scattering. Incoherent scattering is isotropic in a small-angle scattering experiment and thus contributes to the background signal and degrades signal to noise [20]. Figure. 2.6b shows the scattering process in terms of incident (k_i) beam vector that scatters from a sample S at an angle θ , resulting into secondary beam vector (k_f). For elastic, coherent scattering $|\vec{k}_i| = |\vec{k}_f|$, the scattering vector q can be obtained as

$$\begin{aligned} q = |\vec{q}| &= \left| \vec{k}_f - \vec{k}_i \right| = \sqrt{k_f^2 + k_i^2 - 2k_i k_f \cos\theta} \\ &= \frac{4\pi}{\lambda} \sin \frac{\theta}{2} \end{aligned} \quad (2.9)$$

where λ is the wavelength of the incident beam and θ is the scattering angle.

Regardless of the fact that the sample is crystalline or amorphous, we can still write the condition for constructive interference in terms of Bragg’s law:

$$2d \sin \frac{\theta}{2} = n\lambda \quad (2.10)$$

where n is the order of peak (say $n = 1$), and d is the real space distance corresponding to wave vector q and is given by $d = 2\pi/q$. The formula between q and d gives the relation between the size of the object and the corresponding momentum transfer in a diffraction experiment. The measured counts (neutron or electron) of a scattered beam, $I(q)$, recorded by the detector in time t , is dependent on the absolute scattering cross section $\frac{d\sum(q)}{d\Omega}$, by the expression given by Eq. 2.11

$$I(q) = K_{inst} \times d \times t \times T \times \frac{d\sum(q)}{d\Omega} \quad (2.11)$$

where t is the counting time, d is the sample thickness, T is the transmission of the sample and K_{inst} is a constant dependent on instrumental factors and reads as

$$K_{inst} = \varphi_{flux} \times A \times \Delta\Omega \times \varepsilon \quad (2.12)$$

where φ_{flux} is the incident radiation flux on the sample (neutron/cm² s), A is the cross-sectional area of the incident beam, $\Delta\Omega$ is the solid angle subtended by the single pixel of the detector and ε is the detector efficiency. The 2D data obtained for a sample is radial averaged to obtain the 1D data which is then treated for further instrumental correction to obtain the final reduced scattering profile $I(q)$ versus q , where $I(q)$ is expressed in the units of cm⁻¹ and q in nm⁻¹ (or Å⁻¹).

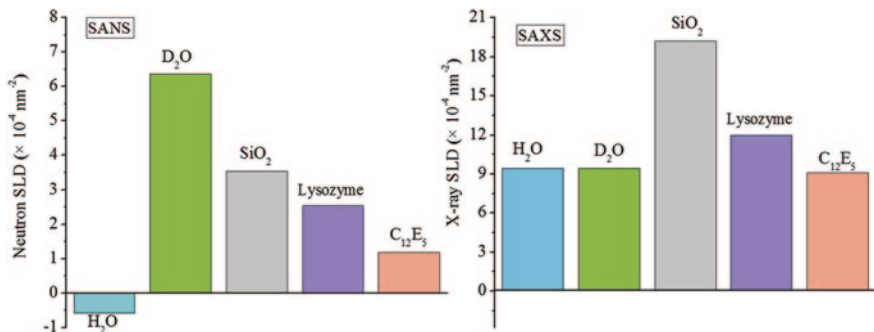


Fig. 2.7 Scattering length density for different components used in the SAXS and SANS experiments. Neutron SLD for H₂O is slightly negative while D₂O has high positive value. This difference enables the use of H₂O/D₂O mixture to contrast match other components in the dispersion, which is not possible with X-rays

The total scattering intensity from a dispersion of nanoparticles can be factorized as follows

$$I(q) = \varphi \Delta\rho^2 VP(q)S(q) \quad (2.13)$$

where φ is the volume fraction of the scattering particles in the dispersion, V is the volume of the single scattering particle, $\Delta\rho$ is the scattering contrast of the particle against the surrounding matrix, $P(q)$ is the form factor of a particle and $S(q)$ is the structure factor of the assembly of the particles. The scattering contrast $\Delta\rho$ in Eq. 2.13 is the difference between the Scattering Length Density (SLD) of scattering particles and the matrix. The value of ρ for a sample composed of different atom i can be calculated as [21]

$$\rho = \sum_i b_i \frac{\delta N_A}{m} = N \sum_i b_i \quad (2.14)$$

where δ is the bulk density of the molecule, m is its relative molar mass, N is the number density of scattering centers and b_i is the coherent scattering length of the nucleus i (for SANS). In X-ray scattering, the scattering length b_i of an atom is proportional to the atomic number Z_i and is given by $b_i = Z_i r_e$ [22], where r_e is the classical electron radius = 2.82×10^{-15} m. Clearly, if in Eq. 2.13 $\Delta\rho$ is zero, the total scattering intensity $I(q)$ becomes zero. When this condition is met the scattering centers are said to be *contrast matched*. Since the scattering from a multi-component system is the weighted summation of the scattering contrast of each component, the contrast matching can simplify the scattering pattern. Figure 2.7 gives the neutron and Cu-K $_{\alpha}$ SLD [23] for H₂O, D₂O, silica, the protein lysozyme [24, 25] and the surfactant C₁₂E₅ (Chaps. 4 and 5). As can be seen, the SLD of H₂O is <0 but for D₂O it is >0. Hence in SANS, the key to the contrast is adjusting the volume ratio of H₂O and D₂O to arrive at the contrast match point for one of the dispersed components of a complex system (in our case silica). In SAXS, this zero scattering

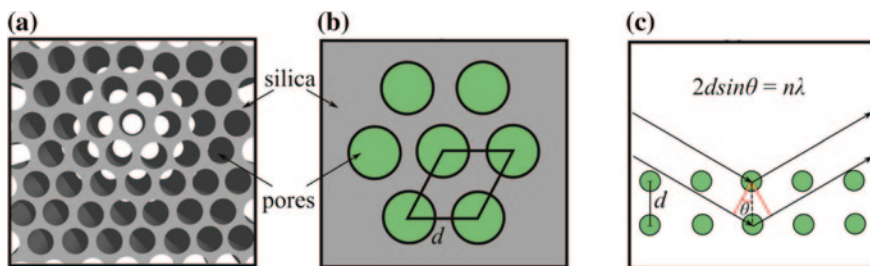


Fig. 2.8 **a** Cartoon showing the ordered pores in the SBA-15 material; **b** 2D hexagonal lattice of the pores indicating the ordered lattice parameters. **c** Bragg's diffraction: Two beams with identical wavelength and phase (X-rays or neutrons) incident on an ordered solid, which are scattered off from two different pores within the lattice

condition cannot be achieved merely by $\text{H}_2\text{O}/\text{D}_2\text{O}$ mixture and the scattering pattern originates from all of its components. For investigating the effect of additives on the adsorbed surfactant on silica nano-spheres SANS measurements were performed on SANS-II instrument at the Paul Scherer Institut, Villigen, Switzerland. For avoiding complications, the silica dispersion was contrast matched by using $\text{H}_2\text{O}/\text{D}_2\text{O}$ ($\approx 38:62$) that corresponds to the SLD of pure silica ($= 3.54 \times 10^{-4} \text{ nm}^{-2}$), hence the scattering originates solely from the surfactant in the dispersion. The SANS data reduction was done by using *BerSANS* software package [26]. Further modeling of the form factors and structure factor is explained in Chap. 3.

2.5 Small Angle Diffraction

In Chap. 5, we have studied the assembly of nonionic surfactant C_{12}E_5 in cylindrical mesopores of SBA-15 silica material. A given mesoporous material is identified by its pore diameter (or width) and pore lattice. A cylindrical pore is regarded as the unit cell i.e. the basic building block of the pseudo crystalline structure of SBA-15. Since the ordered structure of SBA-15 has hexagonal symmetry (Fig. 2.8a, b), the unit cell can be reduced to parallelepiped (Fig. 2.8b) that has two characteristic sides whose length is equal to ' d_{hk} ' lattice parameter. In our study of the self-assembly of surfactant in such ordered mesoporous silica materials, Small Angle Neutron Diffraction (SAND) was applied. The experimental setup of a SAD is similar to SAS. In both the cases, a beam of X-rays or neutrons is incident on the sample and the scattered or diffracted beam is measured by the detector. Diffracted waves from different centers in a material can interfere with each other and the resultant intensity distribution is strongly modulated by this interaction (Fig. 2.8c). If the scattering centers are arranged in a periodic fashion, as in crystals, the diffracted waves will consist of sharp interference maxima (peaks) with the same symmetry as the distribution of the scattering centers. The peaks in a diffraction pattern are directly related to the periodic distance between

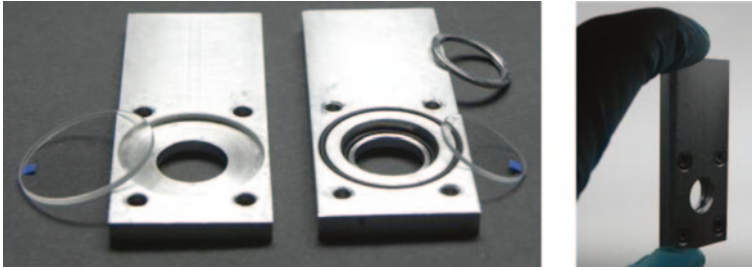


Fig. 2.9 Sample holder used for the scattering experiments with SBA-15 in its disassembled and assembled stage

lattice planes d_{hk} by Eq. 2.10. Whereas, the lattice parameter is related to the scattering vector (Eq. 2.9) by the following equation

$$d_{hk} = 4\pi \sqrt{h^2 + k^2 + hk/q_{hk}\sqrt{3}}, \quad hk = (10, 11, 20) \quad (2.15)$$

where h and k are the Miller indices of the diffraction peak maxima at the wave vector q_{hk} . Hence by determining the peak position in the SAD profile, the lattice parameter can be easily extracted.

SAND measurements were made on D16 instrument at Institut Laue-Langevin, Grenoble, France. 2-D Scattering data was acquired for two different detector angles 0 and 12°. The wavelength broadening for the instrument was $\Delta\lambda/\lambda = 0.1$. *LAMP* software was used for reducing 2D data into 1D diffraction curves, and *SciLab* was used for further modeling of the data. We have studied the adsorption of surfactants in SBA-15 by SAD of neutrons. The samples were prepared in the contrast match H₂O/D₂O water at the contrast match point of SBA-15 ($3.70 \times 10^{-4} \text{ nm}^{-2}$), hence the scattering originates solely from the surfactant with no contribution from the silica material. In a typical experiment a fixed amount of SBA-15 material was taken in a vial with a fixed amount of contrast match water. A requisite amount of C₁₂E₅ surfactant was added to vial and was equilibrated for 12 h. After complete equilibration, SBA-15 with the adsorbed surfactant in the pores settles down and supernatant was drained away, leaving behind the thick slurry. This viscous slurry was transferred to the specially designed holders for the samples (as in Fig. 2.9) and was measured for SAND.

References

1. Livage J, Sanchez C, Henry M, Doeuff S (1989) The chemistry of the sol-gel process. *Solid State Ionics* 32–33:633
2. Davis TM, Snyder MA, Krohn JE, Tsapatsis M (2006) Nanoparticles in lysine-silica sols. *Chem Mater* 18:5814
3. Thomassen LCJ, Aerts A, Rabolli V, Lison D, Gonzalez L, Kirsch-Volders M, Napierska D, Hoet PH, Kirschhock CEA, Martens JA (2010) Synthesis and characterization of stable monodisperse silica nanoparticle sols for in vitro cytotoxicity testing. *Langmuir* 26:328

4. Isrealachvilli JN (2011) Intermolecular and surface forces. Academic Press, USA
5. Atkins PW (1994) Physical chemistry. Oxford University Press, Oxford
6. Hunter RJ (1988) Zeta potential in colloid science: principles and applications. Academic Press, UK
7. Gregg SJ, Sing KSW (1982) Adsorption, surface area and porosity. Academic Press, UK
8. Chatoraj DK, Birdi KS (1984) Adsorption and the Gibbs surface excess. Plenum Press, USA
9. Findenegg GH (1992) Theoretical advancement in chromatography and related separation techniques. Kluwer Academic Publishers, The Netherlands
10. Dietsch O, Eltekov A, Bock H, Gubbins KE, Findenegg GH (2007) Crossover from normal to inverse temperature dependence in the adsorption of nonionic surfactants at hydrophilic surfaces and pore walls. *J Phys Chem C* 111:16045
11. Singh SK, Notely SM (2010) Adsorption of nonionic surfactants (CnEm) at the silica-water and cellulose-water interface. *J Phys Chem B* 114:14977
12. Lugo DM, Oberdisse J, Karg M, Schweins R, Findenegg GH (2009) Surface aggregate structure of nonionic surfactants on silica nanoparticles. *Soft Matter* 5:2928
13. Tyrode E, Ruthland MW, Bain CD (2008) Adsorption of CTAB on hydrophilic silica studied by linear and nonlinear optical spectroscopy. *J Am Chem Soc* 130:17434
14. Gu T, Zhu BY (1990) The S-type isotherm equation for adsorption of nonionic surfactants at the silica gel—water interface. *Colloid Surf* 44:81
15. Smith PK, Krong RI, Hermanson GT, Mallia AK, Gartner FH, Frovenzano MD, Fujimoto EK, Goeke NM, Olson BJ, Klenk DC (1985) Measurement of protein using bicinchoninic acid. *Anal Biochem* 150:76
16. Bharti B, Meissner J, Findenegg GH (2011) Aggregation of silica nanoparticles directed by adsorption of lysozyme. *Langmuir* 27:9823
17. Lerche D, Sobisch T (2007) Consolidation of concentrated dispersions of nano- and micro-particles determined by analytical centrifugation. *Powder Technol* 174:46
18. Sobisch T, Lerche D (2008) Thickener performance traced by multisample analytical centrifugation. *Colloid Surf A* 331:114
19. Detloff T, Lerche D, Sobisch T (2006) Particle size distribution by space or time dependent extinction profiles obtained by analytical centrifugation. *Part Part Syst Charact* 23:184
20. Linder P, Zemb Th (2002) Neutrons, X-rays and light scattering methods applied to soft condensed matter. Delta Series-Elsevier, Netherlands
21. Gabrys BJ (2000) Applications of neutron scattering to soft condensed matter. Gordon and Beach Science publishers, USA
22. Narayanan J, Liu XY (2003) Protein interactions in undersaturated and supersaturated solutions: a study using light and X-ray scattering. *Biophys J* 84:523
23. <http://www.ncnr.nist.gov/resources/sldcalc.html>
24. Efimova YM, van Well AA, Hanefeld U, Wierczinski B, Bouwman WG (2004) On the neutron scattering length density of proteins in H₂O/D₂O. *Phys B* 350:e877
25. Stuhmann HB, Fuess H (1976) A neutron small-angle scattering study of hen egg-white lysozyme. *Acta Cryst* A32:67
26. Keiderling U (2002) The new 'BerSANS-PC' software for reduction and treatment of small angle neutron scattering data. *Appl Phys A* 74:S1455

Chapter 3

Theory and Modeling

3.1 Scattering Data Analysis

As a first step to the modeling of the scattering data, incoherent scattering background was subtracted by applying Porod's law. In the scattering profiles, at sufficiently high- q values, the scattering originates solely from the interface between matrix and scattering object. According to this law, for smooth particle having a sharp interface the scattering intensity should decay as $I(q) \propto q^{-4}$. Hence, to satisfy this condition the data of the high- q scattering regime is fitted to the following equation

$$I(q) \approx A_p q^{-4} + I_{ib} \quad (3.1)$$

where I_{ib} is the incoherent background scattering which is then subtracted from the whole scattering curve. The Porod constant A_p obtained by fitting the experimental curve is related to the specific surface area S and scattering contrast $\Delta\rho$ as

$$A_p = 2\pi S \Delta\rho^2 \quad (3.2)$$

After the background subtraction the scattering profiles were fitted on the basis of form factors models as discussed below. The *Scilab* software package [1] was used for building up the codes for the models, whereas SASfit program [2] was used for the fitting of simple and predefined scattering structure and form factor functions.

Scattering data of dilute dispersions of silica particles were fitted according to the form factor of spheres dispersed in a medium of given contrast. The form factor $P_m(q)$ of monodisperse spheres with radius R is given by

$$P_m(q) = \left[\frac{4}{3}\pi R^3 \times \Delta\rho \times 3 \frac{\sin(qR) - qR \cos(qR)}{(qR)^3} \right]^2 \quad (3.3)$$

where $\Delta\rho$ is the scattering contrast of the sphere against the dispersion medium i.e. $\Delta\rho = \rho_{particle} - \rho_{medium}$. The size polydispersity in the silica beads was taken into

account by the log-normal size distribution. The distribution for mean particle size R_0 and standard deviation σ (polydispersity) is given by

$$D(R, R_0, \sigma) = \frac{1}{\sqrt{2\pi R\sigma}} \exp\left[-\frac{1}{2\sigma^2} \left(\ln \frac{R}{R_0}\right)^2\right] \quad (3.4)$$

The form factor of the system of polydisperse spheres is then given by

$$P(q) = \int D(R, R_0, \sigma) P_m(q, R) dR \quad (3.5)$$

The form factor of the polydisperse sphere was normalized so that the forward scattering ($I(q \rightarrow 0) = 1$). The overall scattering intensity in absolute units was obtained by using the $P(q)$ in the following equation

$$I(q) = NV^2 \Delta\rho^2 P(q) S(q) \quad (3.6)$$

where N is the number density of the particles with scattering length contrast $\Delta\rho$ against the background, V is the volume of single particle and $S(q)$ is the structure factor of the system. $S(q)$ accounts for the inter-particle correlations arising in the system. For a dilute non-interacting system $S(q) = 1$.

3.1.1 *Micelle-Decorated Bead Model*

In Chap. 4, we report a SANS study of surfactant adsorption on silica nanoparticles, where the SANS profiles are modeled on the basis of previously developed micelle decorated bead model [3]. The model accounts for the structure of the adsorbed surface micelles on spherical silica beads in the silica contrast match scenario. The model assumes that there is a random distribution of the spherical (or ellipsoidal) surface micelles of radius R_a .

First step of this model involves the generation of a completely random set of coordinates of the center of each surface micelle lying on the outer surface of a silica nanoparticle of radius R_b . This random but uniform distribution of spherical micelles was achieved by *hypercube rejection method* [4], where three numbers (A_1 , A_2 and A_3) are generated from a completely random distribution that satisfies the following set of conditions

$$A_4 = A_1^2 + A_2^2 + A_3^2 \quad (3.7)$$

If $A_1 \neq -1$; $A_2 \neq -1$; $A_3 \neq -1$; and $A_4 \leq 1$ then the coordinates of the surface micelles is given by

$$\begin{aligned} x &= (R_a + R_b) \times \frac{2(A_4 + A_1 A_3)}{a_4}; \\ y &= (R_a + R_b) \times \frac{2(A_3 A_4 - A_1 A_2)}{a_4}; \\ z &= (R_a + R_b) \times \frac{2(A_1^2 + A_4^2 - A_2^2 - A_3^2)}{A_4} \end{aligned} \quad (3.8)$$

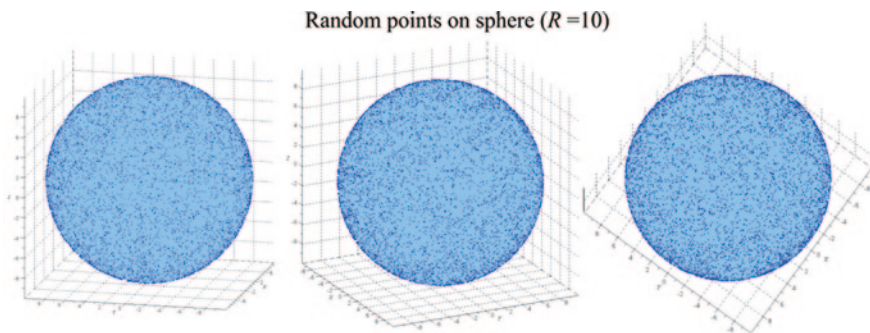


Fig. 3.1 A set of 1,000 points generated on a sphere of radius 10. The simulation gives the uniform and completely random distribution of points on the sphere

Figure 3.1 shows the set of 1,000 such random points generated on the surface of a sphere of radius 10 (units). The distribution was completely random as can be seen in Fig. 3.1. The adsorption of micelles to silica means that the center of each surface micelle will lie on the sphere of radius ($R_a + R_b$).

The inter-micellar structure factor $S_a(q)$ arising due to the correlations between the N_a micelles on the surface of the same sphere is generated by Fourier transformation of their real space pair-distribution function. Mathematically, it can be represented as [5]

$$S_a(q) = 1 + \frac{1}{N_a} \sum \frac{\sin(q(r_i - r_j))}{q(r_i - r_j)} \quad (3.9)$$

Here $r_i - r_j$ is the center-to-center distance between a pair of surface micelles sitting on the surface of a particle. To get a statistically averaged $S_a(q)$, the simulation was an average over 1,000 iterations. The polydispersity of silica bead as well as for the surface micelles was taken into account by generating the radii of R_a and R_b from their respective log-normal size distribution.

The overall intensity of the scattering profile in absolute scale is given by the equation similar to (3.6) which reads as follows

$$I(q) = NV_a^2 \Delta\rho^2 P_a(q) S_a(q) S_{HS}(q) \quad (3.10)$$

Here N is the number density of the surface micelles in the dispersion (=no. density of silica bead $\times N_a$), $P_a(q)$ is the form factor of surface micelles, V_a is the volume of one surface micelles and $\Delta\rho$ is the average contrast of the surface micelle against the $\text{H}_2\text{O}/\text{D}_2\text{O}$ mixture ($\rho_{\text{silica}} = 3.54 \times 10^{-4} \text{ nm}^{-2}$), and is calculated by incorporating the change in contrast due to hydration of surfactant micelles. Figure 3.2a shows the average inter-micellar structure factor $S_a(q)$ for 20 surface micelles on a silica bead of 10 nm radius. The figure also presents the form factor of a spherical surface micelle $P_a(q)$ of 2 nm radius and having 10 % polydispersity in size. The overall form factor of the bead decorated with spherical surface micelles is given by the product of $P_a(q)$ and $S_a(q)$ and is shown in Fig. 3.2b,

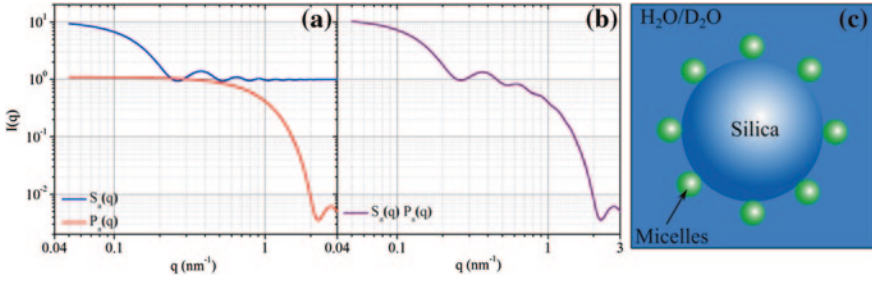


Fig. 3.2 **a** Simulated inter-micellar structure factor $S_d(q)$ for 20 micelles on the silica particle with radius $R_b = 10$ nm (10 % polydispersity) (blue line). Red line indicates the form factor $P_a(q)$ of spherical micelles of radius $R_a = 2$ nm (10 % polydispersity). **b** Overall form factor of the micelle-decorated bead model ($P(q) = S_d(q) \times P_a(q)$). **c** Cartoon representing the silica nanoparticle in contrast matched medium with spherical surfactant micelles at its periphery

where the oscillation at $q \simeq 0.3 \text{ nm}^{-1}$ is the signature of the invisible silica particles and the oscillation at $q \simeq 3.0 \text{ nm}^{-1}$ is the primary oscillation of the form factor of surface micelle. In Eq. 3.10, the term $S_{\text{HS}}(q)$ is the hard-sphere structure factor accounting for correlations between the silica particles in the dispersion. In the experimental pH range silica nanoparticles are negatively charged and the dispersion is stable because of their repulsive interaction. If the number density of silica particles is high then there appears a pseudo order in the system, which results in the appearance of a radial correlation function. The first maximum in the correlation function corresponds to the distance by which the particles are separated and is called the hard sphere repulsion radius. The analytic expression for $S_{\text{HS}}(q)$ is as follows [6, 7]

$$S(q) = \frac{1}{1 + 24\varphi \frac{G(q)}{qR_{\text{HS}}}} \quad (3.11)$$

where φ is the volume fraction of the particles in the dispersion and $G(q)$ is given by

$$G(q) = \alpha \frac{(\sin A - A \cos A)}{A^2} + \beta \frac{(2A \sin A + (2 - A^2) \cos A - 2)}{A^3} + \gamma \frac{(-A^4 \cos A + 4[(3A^2 - 6) \cos A + (A^3 - 6A) \sin A + 6])}{A^5} \quad (3.12)$$

with $\alpha = \frac{(1+2\varphi)^2}{(1-\varphi)^4}$; $\beta = -6\varphi \frac{(1+\varphi/2)^2}{(1-\varphi)^4}$; $\gamma = \frac{\varphi\alpha}{2}$ and $A = 2R_{\text{HS}}q$ where R_{HS} is the hard sphere repulsion.

The micelle-decorated bead model can successfully predict the morphology of C_{12}E_5 micelles on silica nanoparticles at silica/solvent contrast match conditions. In other situations where this contrast scenario is not feasible it is desirable to study such decorated particles in a full contrast scenario. The corresponding relations have been derived and given below.

3.1.2 Raspberry-Like Bead Model

As mentioned in the previous section that the micelle-decorated bead model was applicable only to core contrast-match conditions. Here we present the respective model applicable for the full contrast conditions. The model can be applied to scattering patterns generated by the *raspberry* shaped materials synthesized recently [8, 9]. In the present context, the model has been developed for its potential application to the system of silica beads with adsorbed protein molecules. In the full contrast scenario, the incident neutrons observe the protein and silica as the system made up of three phases viz. protein, silica and solvent. The principle of the model is similar to the micelle-decorated bead model, where the inter-micellar structure factor is generated and then the overall scattering intensity is given by Eq. 3.14. Up to this point, the modeling remains the same as in Sect. 3.1.1, but in order to take into account the scattering originating from the core of raspberry structure. By neglecting the cross terms, the net scattering intensity is given by the arithmetic sum of I_a and I_b given by following equations

$$I_a(q) = NV_a^2 \Delta\rho_{\text{sol-pro}}^2 P_a(q) S_a(q) \quad (3.13)$$

$$I_b(q) = N_b V_b^2 \Delta\rho_{\text{sol-core}}^2 P_b(q) \quad (3.14)$$

where

$I_a(q), I_b(q) \rightarrow$ intensity contribution of the adsorbed protein and silica,

$N, N_b \rightarrow$ number densities of protein and silica bead,

$V_a, V_b \rightarrow$ volume of one protein and silica particle,

$\Delta\rho_{\text{sol-pro}}, \Delta\rho_{\text{sol-core}} \rightarrow$ SLD contrast between protein-solvent and silica-solvent,

$S_a(q) \rightarrow$ structure factor arising due to correlation of adsorbed protein on single silica particle,

$P_a(q), P_b(q) \rightarrow$ form factor of the protein (sphere or ellipsoid) and of the silica core,

The overall scattering of the composite system is given by the sum of the individual scattering functions as in Eqs. 3.13 and 3.14 which reads as

$$I_{\text{total}}(q) = [I_a(q) + I_b(q)] S_{\text{HS}}(q) \quad (3.15)$$

here $I_{\text{total}}(q)$ is net scattering intensity and $S_{\text{HS}}(q)$ is the hard-sphere structure factor between the silica beads decorated with protein molecules.

Simulations profiles for the RLB model show that the profiles are sensitive to the arrangement of the raspberry-like entities (adsorbed surfactant micelles or protein molecules), as shown in Fig. 3.3, which compares RLB with a simple sphere. The main difference in the scattering profile of the two is observed in the Porod regime, where a higher scattering intensity of the composite material arises because of the larger surface area presented to the incident beam (because of adsorbed entities). The relevant parameters in the RLB model are bead radius R_b , volume fractions (ϕ_a, ϕ_b) of protein (or micelle) and silica, size (R_a) and shape of adsorbed entity and polydispersity of the bead (s_b). Table 3.1 summarizes the values of the parameters used for simulating the scattering profiles shown in Fig. 3.3.

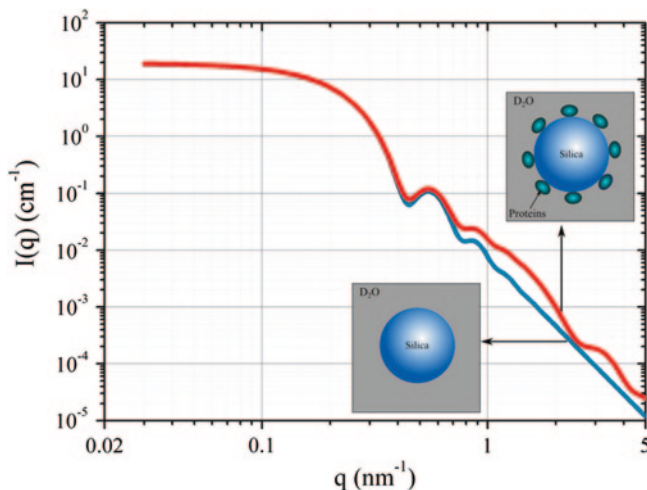


Fig. 3.3 Simulated scattering profile for the bare spherical particles and particles covered with ellipsoidal particles. The profile shows the significant differences at the high- q regions

Table 3.1 Parameters for simulating the scattering intensity profiles for *Raspberry-like-bead* (RLB) model and spheres, as presented in Fig. 3.3

| | R_b (nm) | R_a (nm) | φ_b | φ_a | s_b |
|-----------|------------|------------|--------------------|--------------------|-------|
| RLB model | 10 | 1.75 | 5×10^{-3} | 7×10^{-4} | 0.1 |
| Sphere | 10 | – | 5×10^{-3} | – | 0.1 |

Polydispersity is expressed by the standard deviation from the mean particle size

3.2 Particle Assembly

In Chap. 9, we present a novel method devised for harvesting permanent linear chains of oppositely charged latex particles by the initial application of an AC electric field. Here we introduce the basic theory behind the chaining process by dielectrophoresis (DEP) and then give the details of the theory developed, which predicts the distribution of chain lengths of the permanent chains for equally-sized and differently-sized particles of the binary system.

3.2.1 Dielectrophoresis

Colloidal particles suspended in a medium (aqueous or non-aqueous) can be assembled into ordered structures by the application of direct (DC) [10] or alternating current (AC) fields [11, 12], where the driving force of assembly is the particle polarization, ionic mobility in the medium coupled with fluid flow, and forces resulting from gradients in the field. Whenever a dielectric particle is

subjected to a non-uniform electric field, a force is exerted on the particle, the force experienced is called the dielectrophoretic force (F_{DEP}) and the phenomenon is called dielectrophoresis (DEP). Mathematically, F_{DEP} is given by the following equation [13–15]

$$F_{DEP} = 2\pi \varepsilon_1 \text{Re}|K(\omega)|R^3 \nabla E^2 \quad (3.16)$$

where ∇E is the gradient of the field, R is the radius of the particle, $\text{Re}|K(\omega)|$ is the real part of Clausius-Mossotti function, $K(\omega)$, given by

$$\text{Re}|K(\omega)| = \frac{\varepsilon_2 - \varepsilon_1}{\varepsilon_2 + 2\varepsilon_1} + \frac{3(\varepsilon_1\sigma_2 - \varepsilon_2\sigma_1)}{\tau_{MW}(\sigma_2 + 2\sigma_1)^2(1 + \omega^2\tau_{MW}^2)} \quad (3.17)$$

where ε and σ represent the dielectric permittivity and electrical conductivity, and the indices 1 and 2 refer to the solvent medium and the particles, respectively and τ_{MW} is the Maxwell–Wagner charge relaxation time, given as [12] $\tau_{MW} = \frac{\varepsilon_2 + 2\varepsilon_1}{\sigma_2 + 2\sigma_1}$.

The origin of the DEP is the frequency-dependent polarization of particles in AC fields applied across a suspension. The magnitude of the dipoles induced in the particles is given in Eq. 3.18. The electric field induced effects on dispersions containing particles are very complex, primarily because of the presence of large numbers of interacting dipoles (i.e. particles). The dipoles induced within a particle interact with those of neighboring particles, thus drawing them into long chains along the direction of field. The electric field directed along the positive z -axis with strength E , induces an electric dipole moment μ in the spherical particle given as

$$\mu = \mathbf{a}_z 4\pi \varepsilon_1 \left(\frac{\varepsilon_2 - \varepsilon_1}{\varepsilon_2 + 2\varepsilon_1} \right) R^3 E \quad (3.18)$$

where \mathbf{a}_z is the unit vector in z -direction. The force of attraction felt by a sphere with induced dipole moment (μ_1) due to another sphere with induced dipole moment (μ_2) along the direction of field ($\theta = 0^\circ$ (F_0)) and perpendicular to the field ($\theta = 90^\circ$ (F_{90})) is given by Stoy [16] and reads as

$$F_0 = -\mathbf{a}_z E \frac{6\mu_1\mu_2}{4\pi \varepsilon_1 D^4}; \theta = 0^\circ \quad (3.19)$$

$$F_{90} = \mathbf{a}_z E \frac{3\mu_1\mu_2}{4\pi \varepsilon_1 D^4}; \theta = 90^\circ \quad (3.20)$$

where θ is the angle between the vector joining the centers of two particles (length = D) with \mathbf{a}_z .

In the absence of field, particles with symmetric surface charge distribution, the dipole moment becomes zero and the force between the particles vanishes. The assembly of the particle induced by AC field disintegrates (because of surface charge repulsion and thermal motion) and hence is temporary. As will be discussed in Chap. 9, we have devised a method for avoiding this disintegration of chain

structures by using a bi-particle system composed of oppositely charged particles. In the Sect. 3.2.2 a numerical simulation algorithm is presented to determine the chain-length distribution of the resulting permanent chains, and in Sect. 3.2.3 a closed expression for this chain-length distribution is derived.

3.2.2 Chain-Length Distribution from Numerical Simulations

Chain length distribution as a function of the number ratio of the two components by a numerical simulation approach was adopted. In this algorithm the bi-particle assembly was treated analogous to the classical statistical problem of randomly distributing balls into boxes. The balls and boxes problem has been applied to find the distribution functions of numerous statistical arrangements and ensembles for many practical applications [17–19]. This simulation was adopted to predict the chain length distribution of the assembled structure. In our experiments, we have used pairs of particles of similar size (system 1) and of dissimilar size (system 2). In equal particle size scenario (system 1) both positive and negative particles participate in chain formation. In the case of unequal sized particles (system 2), only the larger particles (*A*-type) are involved in the primary chain formation step and only then the small particles (*B*-type) are dragged at the interstitial sites between the bigger particles (for details see Chap. 9). For both the systems, it was assumed that in the presence of the electric field all the particles are contained in a single chain made of 10^5 particles. When the field is switched-off, all the secondary permanent chains break from this parent chain only. The mechanisms of the chain formation for the two systems are different and we have distinguished our simulation approach for the two cases as follows:

3.2.3 Equally-Sized Particles: Random Arrangement of Balls

For equally-sized particles, in the presence of the AC field, a completely random arrangement of positive and negative particles in the chain is formed. Hence for simulating system 1, an array of N boxes was arranged and $N_A + N_B$ balls were placed one-by-one in the boxes, with the constraint that no box can contain more than one ball. In a typical simulation run, 10^5 positive and 10^5 negative particles ($r = 1$) were arranged in a linear array of 2×10^5 (completely random distribution). Up to this point the assembly reflects the case in the presence of AC field. When the field is switched off the chain will break up at each location where two particles of same charge are present at consecutive position (*A*–*A* or *B*–*B*). The distribution of the permanent chain lengths was obtained by checking each pair of adjacent particles in the array and applying the above mentioned condition. Hence, for equally sized particles it is the correlation of the occurrence of two equally charged particles at adjacent position in an infinitely long chain that determines

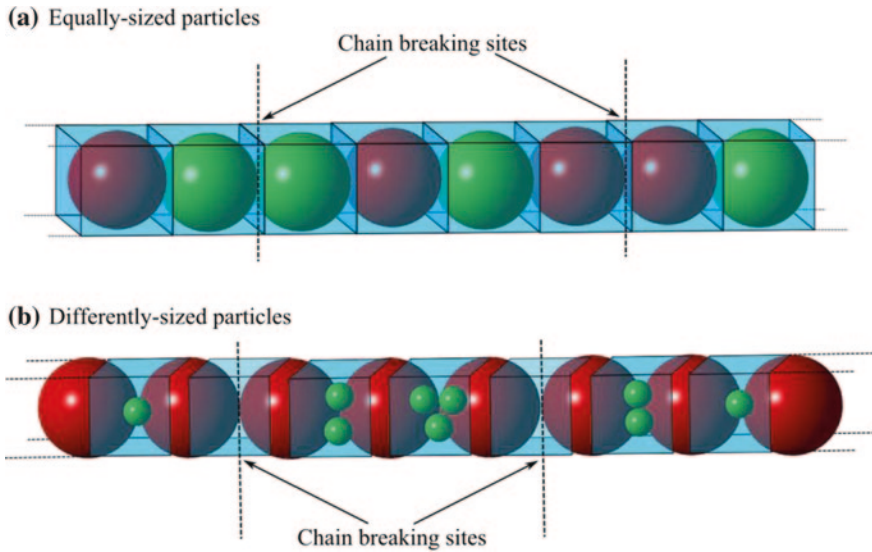


Fig. 3.4 Realizations of the two systems (1 and 2) in order to mimic it as balls and boxes statistical problem. **a System 1** Each positive and negative particle (balls) itself is contained in one box **b System 2** The box is assumed to be located at the site between the two large particles and the balls (small particles) are randomly distributed in the boxes

the chain length distribution. The results obtained by the above explained statistical simulations are given in Appendix A.3.1.1 of this thesis (Fig. 3.4).

3.2.4 Differently-Sized Particles: Throwing Balls in Boxes

The chaining of differently sized particles, when only the larger particles participate in the primary chaining step and the smaller particles are later drawn into the interstices between large particles, was simulated by the algorithm of throwing balls (small particles) into boxes arranged in between the large particles. The boxes can be taken as an analogy to the binding sites of small particles located in-between two larger ones in the chain. In these simulations, the chain length was defined by the number of large particles in the chains, rather than the total number ($N_A + N_B$) of particles bound, as was the case in system 1. In a typical simulation run, a numbered array of 10^5 boxes (binding sites = $N_A - 1$) was arranged and N_B balls ($= r \times N_A$) were distributed randomly with no restriction on the maximum occupancy of the box. Here, the condition for chain rupturing was met when a box after distributing all the balls remained unoccupied and the chain breaks away at that specific junction. Again, the chain length distribution was expressed in terms of fraction of chains (X_n) and fraction of particles (Φ_n) in the chains of given

length (L). Hence, in this case it's the correlation between the positions of the empty boxes in the single parent chain that determines the chain length distribution of the permanent structures formed. It has been shown in Appendix A.3.1.2, if the number of balls thrown to a fixed number of boxes increases, the mean chain length obtained increases, this can be understood by the fact that as the average number of balls thrown per box increases. The probability of a box to be occupied (containing at least 1 ball) increases. For system 2, we carried out the simulations at different r values and compared the chain length distribution given by simulations and the kinetic model.

3.2.5 Statistical Model for Chain Length Distribution

DEP can be used to assemble chains of charged spherical particles carrying opposite charges in a permanent way. We consider an assembly of N_A particles A (negatively charged) and N_B particles B (positively charged), all of equal size (radius R). Experiments show that “*chaining*” depends not only on the concentration of A and B type particles, but also on the size ratio of the two particles. Here we analyze the distribution of chain lengths for two cases, namely pairs of oppositely charged particles of equal and different sizes.

3.2.6 Equally-Sized Particles

For micrometer-sized particles the field-induced dipole interaction between the particles outweighs the interactions caused by the positive and negative surface charges of the two types of particles. Accordingly, in the electric field all the $N_A + N_B$ particles will assemble to long chains in which A and B particles are arranged in a purely statistical order. When the field is switched off, the electrostatic interactions between the charged surfaces of the particles determine the type of final structures formed. For particles of sufficiently high charge, bonds between oppositely charged neighboring particles (A–B) will survive, while bonds of equally charged neighboring particles (A–A or B–B) will break. Since the particles in the long chains had been arranged in a purely statistical manner, the probability of finding a chain of n particles A and B in alternating order depends on the mole fraction x of (B-type) particles in the biparticle dispersion. It is proportional to $x^{n/2}(1-x)^{n/2}$ for equal numbers of A and B (n even) and to $x^{(n+1)/2}(1-x)^{(n-1)/2}$ for chains with B particles on either end (n odd). For biparticle mixtures of stoichiometric composition ($x = x_0 = \frac{1}{2}$) the normalized concentration of n -mer chains is given by $X_n = \frac{1}{2}x_0^n$. When the composition deviates from the stoichiometric by some increment Δx , i.e., $x = x_0 + \Delta x$, the normalized concentrations of n -mer chains can be expressed by a polynomial in $\delta = \Delta x/x_0$, which for $\delta < 0.1$ can be approximated by

$$X_n = \frac{1}{2} x_0^n \left(1 - \frac{n'}{2} \delta^2 \right) \quad (3.21)$$

where $n' = n$ for even n and $n' = n - 1$ for odd n .

The results may also be expressed in terms of Φ_n , the fraction of particles contained in n -mer aggregates,

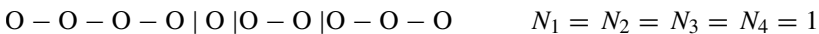
$$\Phi_n = nX_n = nx^n \quad (3.22)$$

In System 1 of this study particles A and B have similar sizes ($D_B/D_A = 1.1$) and thus the dipole moment induced by the electric field will also be similar ($\mu_B/\mu_A \approx 1.3$). Accordingly, this system should conform to the model of particle assembly outlined above. Figure 9.2 of the thesis shows that the distribution law resulting for this model (Eqs. 3.21 and 3.22) indeed gives a good representation of the experimental size distribution for this system.

3.2.7 Differently-Sized Particles

When the size of the two types of particles differs at least by the factor 4, as in system 2 of the studied systems ($D_B/D_A = 0.225$) [for details go to Chap. 9], the induced dipole moments in the two particles will differ by about two orders of magnitude ($\mu_B/\mu_A \approx 0.01$). Accordingly, only the large (A-type) particles will participate in the field-induced primary chain formation step. The small (B-type) particles will attach to these chains in a secondary step only while the electric field is still on. Based on evidence from earlier studies by Gupta et al. [20]. We suppose that the attachment sites for the B particles are at the rim between neighboring A particles. When the electric field is switched off, small B particles can form links between the two oppositely charged A particles, possibly by slipping in a central location between the neighboring A particles.

To model the resulting chain length distribution we assume that each contact point in the chain of large particles (A) formed in the primary DEP process represents a binding site for the positively charged small particles (B), which then forms a permanent bond between the two A particles when the field is switched off. If $S - S_0$ out of the S binding sites in the primary chain of A particles are occupied by B particles, and S_0 sites remain vacant, the primary chain will break up into $G = S_0 + 1$ fragment groups of particles (“secondary chains”) [The “number of chains” G includes single A particles] when the field is switched off. As an example, consider the situation of $N_A = 10$ and $N_B = 6$: The B particles form 6 bonds (indicated by horizontal lines) and leave 3 vacant binding sites (vertical lines). Accordingly, $G = N_A - N_B = 4$. In the example shown below the group is made up of one monomer ($N_1 = 1$), one dimer ($N_2 = 1$) one trimer ($N_3 = 1$) and one tetramer ($N_4 = 1$):



However, different distributions of n -mers can be realized by interchange of the locations of bonds and vacant sites, as summarized in the table below for $N_A = 10$, $N_B = 6$ ($G = 4$).

| k | N_1 | N_2 | N_3 | N_4 | N_5 | N_6 | N_7 | ω_k |
|---|-------|-------|-------|-------|-------|-------|-------|------------|
| a | 3 | – | – | – | – | – | 1 | 4 |
| b | 2 | 1 | – | – | – | 1 | – | 12 |
| c | 2 | – | 1 | – | 1 | – | – | 12 |
| d | 2 | – | – | 2 | – | – | – | 6 |
| e | 1 | 2 | – | – | 1 | – | – | 12 |
| f | 1 | 1 | 1 | 1 | – | – | – | 24 |
| g | 1 | – | 3 | – | – | – | – | 4 |
| h | – | 3 | – | 1 | – | – | – | 4 |
| i | – | 2 | 2 | – | – | – | – | 6 |

A distribution k characterized by a set of distribution numbers $\{N_n\} = \{N_1, N_2, N_3, \dots\}$ has a certain number of equivalent realizations, ω_k , given by

$$\omega_k = \frac{G!}{\prod_n N_n!} \quad (3.23)$$

The most likely distribution $\{N_n^*\}$ is the one with the largest number of realizations ω_k . Hence we look for the set of variables $\{N_n\}$ which maximizes ω_k subject to the constraints

$$\sum_n N_n = G \quad (3.24)$$

$$\sum_n nN_n = N_A \quad (3.25)$$

We calculate the set of most likely distribution numbers $\{N_n^*\}$ by the Lagrange method of undetermined multipliers (α and β). For large N_A and N_B the numbers of n -mer chains of this distribution are given by

$$N_n^* = e^{-\alpha} (e^{-\beta})^n = \frac{G^2}{N_A - G} \left(\frac{N_A - G}{N_A} \right)^n \quad (3.26)$$

So far we assumed that a bond between two A particles is made by a single B particle (single bond). In that case the number of fragment groups G is given by $N_A - N_B$. Accordingly, no fragmentation should occur when N_B is equal to the number of binding sites, $S = N_A - 1 \approx N_A$. The experiments show, however, that more than one B particle can be accommodated between two A particles. This implies that some sites will remain vacant even if $N_B > N_A$. For large particle numbers N_A and N_B we can replace the number of fragment groups by the number of vacant sites, i.e., $S_0 = G - 1 \approx G$. The number of n -mer chains normalized to the total number of A particles, X_n , and the fraction of A particles existing in form of r -mer chains, Φ_n , is then given by

$$X_n = \frac{N_n^*}{N_A} = \frac{S_0^2}{N_A(N_A - S_0)} \left(1 - \frac{S_0}{N_A}\right)^n = \sigma_0^2(1 - \sigma_0)^{n-1} \quad (3.27)$$

$$\Phi_n = nX_n = n\sigma_0^2(1 - \sigma_0)^{n-1} \quad (3.28)$$

where $\sigma_0 = S_0/N_A$ is the fraction of vacant sites.

Determination of the fraction of vacant sites σ_0

To determine the fraction of vacant binding sites we have to consider the distribution of B-type particles over the binding sites. The total number of binding sites, S , is made up of vacant sites (S_0), singly occupied sites (S_1), doubly occupied sites (S_2), etc.

$$S = S_0 + S_1 + S_2 + \dots = S_0 + \sum_{m=1}^{\infty} S_m \quad (3.29)$$

The distribution numbers $\{S_m\}$ will depend on whether the B-type particles are bound to the binding sites in a reversible or irreversible way. Irreversible binding leads to the Poisson distribution, while reversible binding can be treated by a multiple-step mass-action law.

(a) Poisson distribution

According to the Poisson distribution law the probability of finding m out of N particles on a given site is given by

$$P_N(m) = \frac{(Np)^m}{m!} e^{-Np} \quad (3.30)$$

where p is the probability for a single particle to be on this site. In the present case we have S equivalent binding sites and thus $p = 1/S$. When identifying N with the number of B-type particles in the system, we have $Np = \frac{N_B}{S} \approx \frac{N_B}{N_A} = r$. The probability $P_N(m)$ can then be identified with the fraction of binding sites occupied with m particles, $\sigma_m = S_m/S$,

$$\sigma_m = \frac{(r)^m}{m!} e^{-r} \text{ with } m = 0, 1, 2, \dots \quad (3.31)$$

Accordingly, on the basis of the Poisson distribution the fraction of vacant sites ($m = 0$) is $\sigma_0 = e^{-r}$.

(b) Multiple-step mass action law

When binding of B particles to vacant binding sites is reversible, the numbers of vacant and single occupied sites along the chain will be connected by a *Langmuir* type equilibrium

$$S_1 = K_1 c_B S_0 \quad (3.32)$$

where K_1 represents a binding constant and c_B is the concentration of free (non-bound) B particles. A similar relation will apply for the numbers of sites occupied

by one and two particles, and generally for the numbers of sites occupied by $m - 1$ and m particles, viz.

$$S_m = K_m c_B S_{m-1} \quad \text{for } m = 2, 3 \dots \quad (3.33)$$

where K_m represents the binding constant for sites at which $m - 1$ particles are already bound. Here we assume that all binding constants are equal, i.e. $K_1 = K_2 = \dots = K$. With the abbreviation $z = Kc_B$ we then obtain

$$S_m = z^{m-1} S_1 = z^m S_0 \quad m = 1, 2, 3 \dots \quad (3.34)$$

$$S = S_0 + \sum_{m=1}^{\infty} S_m = S_0 \left(1 + \sum_{m=1}^{\infty} z^m \right) = S_0 \left(1 + \frac{z}{1-z} \right) \quad (3.35)$$

$$N_B = \sum_{m=1}^{\infty} m S_m = S_0 \sum_{m=1}^{\infty} m z^m = S_0 \frac{z}{(1-z)^2} \quad (3.36)$$

From Eqs. (3.35) and (3.36) we find the average number of B particles per site

$$\frac{N_B}{S} = \frac{z/(1-z)^2}{1+z/(1-z)} = \frac{z}{(1-z)} \quad (3.37)$$

and with $\frac{N_B}{S} \approx \frac{N_B}{N_A} = r$ we obtain

$$z = \frac{r}{r+1} \quad (3.38)$$

When z is known, the number of vacant sites S_0 , and $\sigma_0 = S_0/N_A$, can be calculated by Eq. 3.36

$$S_0 = N_B \frac{(1-z)^2}{z} = N_B \frac{1}{r(r+1)}; \sigma_0 = r \frac{(1-z)^2}{z} = \frac{1}{r+1} \quad (3.39)$$

σ_0 is then used to determine the distribution numbers X_n and Φ_n by Eqs. (3.27) and (3.28). According to this relation, σ_0 is decreasing with increasing r much more slowly than the e^{-r} dependence predicted by the Poisson law. This is why the multiple-step mass action law, unlike the Poisson relation, does not yield an excessively wide distribution of chain lengths for larger r .

References

1. Consortium Scilab—Digiteo (2011) Scilab: free and open source software for numerical computation (OS, Version 5.3.3) [Software]. Available from: <http://www.scilab.org>
2. <http://kur.web.psi.ch/sans1/SANSSoft/sasfit.html>
3. Oberdisse J (2004) Small angle neutron scattering and model predictions for micelle-decorated colloidal silicabeads. Phys Chem Chem Phys 6:1557

4. <http://www.math.niu.edu/~rusin/known-math/96/sph.rand>
5. Despert G, Oberdisse J (2003) Formation of micelle-decorated colloidal silica by adsorption of nonionic surfactant. *Langmuir* 19:7604
6. Percus JK, Yevick GJ (1958) Analysis of classical statistical mechanics by means of collective coordinates. *Phys Rev* 110:1
7. Vrij A (1979) Mixtures of hard spheres in the Percus–Yevick approximation. Light scattering at finite angles. *J Chem Phys* 71:3267
8. Pi M, Yang T, Yuan J, Fujii S, Kakigi Y, Nakamura Y, Cheng S (2010) Biomimetic synthesis of raspberry-like hybrid polymer–silica core–shell nanoparticles by templating colloidal particles with hairy polyamine shell. *Colloid Surf B* 78:193
9. Su Y, Yan R, Dan M, Xu J, Wang D, Zhang W, Liu S (2011) Synthesis of hierarchical hollow silica microspheres containing surface nanoparticles employing the quasi-hard template of poly (4-vinylpyridine) microspheres. *Langmuir* 27:8983
10. Holgado M, Santamaria FG, Blanco A, Ibisate M, Cintas A, Miguez H, Serna CJ, Molpeceres C, Requena J, Mifsud A, Meseguer F, Lopez C (1999) Electrophoretic deposition to control artificial opal growth. *Langmuir* 15:4701
11. Hermanson KD, Lumsdon SO, Williams JP, Kaler EW, Velev OD (2001) Dielectrophoretic assembly of electrically functional microwires from nanoparticle suspensions. *Science* 294:1082
12. Velev OD, Bhatt KH (2006) On-chip micromanipulation and assembly of colloidal particles by electric fields. *Soft Matter* 2:738
13. Pohl HA (1958) Some effects of nonuniform fields on dielectrics. *J Appl Phys* 22:869
14. Jones TB (1995) *Electromechanics of particles*. Cambridge University Press, UK
15. Muller T, Gerardino A, Schnelle T, Shirley SG, Bordoni F, DeGasperi G, Leoni R, Fuhr G (1996) Trapping of micrometre and sub-micrometre particles by high-frequency electric fields and hydrodynamic forces. *J Phys D Appl Phys* 29:340
16. Stoy RD (1994) Interactive dipole model for two-sphere system. *J Electrostat* 33:385
17. Davis JM, Giddings JC (1983) Statistical theory of component overlap in multicomponent chromatograms. *Anal Chem* 55:418
18. Bialas P, Bogacz L, Jhonston D (2000) Finite size scaling of the balls in boxes model. *Nucl Phys B* 5:599
19. Ewens WJ, Wilf HS (2007) Computing the distribution of the maximum in balls-and-boxes problems with application to clusters of disease cases. *Proc Natl Acad Sci USA* 27:11189
20. Gupta S, Alargova RG, Kilpatrick PK, Velev OD (2008) On-chip electric field driven assembly of biocomposites from live cells and functionalized particles. *Soft Matter* 4:726

Part II

Curvature and Surface Energy Effects on the Interaction of Hydrophilic Silica with Nonionic Surfactant

In Chap. 4, we present the results of surfactant $C_{12}E_5$ adsorption on silica nanoparticles. In addition we perform SANS measurements aimed to study the effect of particle size and surface modification of silica nanoparticles on the self-assembly of the adsorbed surfactant. Chapter 5 deals with the complementary situation of the self-assembly of the surfactant in cylindrical nanopores of SBA-15 silica and the effects of a surface modifier on the binding tendency of the $C_{12}E_5$ surfactant to the pore-walls are also presented.

Chapter 4

Surfactant Adsorption and Aggregate Structure at Silica Nanoparticles

4.1 Introduction

Surfactant adsorption onto colloidal particles is of eminent importance to technological processes in which colloidal stability or detergency plays a role [1–5]. Surfactant adsorption onto hydrophilic surfaces can be regarded as a surface aggregation process, reminiscent of micelle formation in solution [6–14]. When the anchoring of the surfactant heads to the surface is weak, as in the case of nonionic surfactants at oxide surfaces, the morphology of surface aggregates may depend both on the anchoring strength [15, 16] and on the curvature of the adsorbing surface [17–23]. For instance, for the surfactant penta (ethyleneglycol) monododecylether ($C_{12}E_5$) it was recently found that discrete surface micelles are formed on silica nanoparticles [19, 21], although flat bilayers aggregates are preferred at planar silica surfaces [11, 12]. At even weaker anchoring energies, surface micelles may be disfavored against micelles in solution, implying that little or no adsorption occurs, as in the case of dodecyl maltoside (β - $C_{12}G_2$) at silica nanoparticles [19].

Here, we study the influence of particle size and surface modification on the adsorption of the surfactant $C_{12}E_5$ at silica nanoparticles. The particles were synthesized by a modified Stöber method [24] yielding particles of narrow size distribution down to the 10 to 50 nm size range which was of interest in this study. In this method, the basic amino acid lysine is used instead of ammonia as the catalyst for the hydrolysis of the silica precursor. For the resulting Lys-Sil particles [24] it was found that the adsorption isotherm of $C_{12}E_5$ exhibits a pronounced dependence on particle size. To assess the influence of lysine on the surface energy and the adsorption of the surfactant at the silica particles we also investigated the adsorption of lysine on pure siliceous silica nanoparticles (Ludox-TMA) and

Reprinted with permission from Bharti, B., Meissner, J., Gasser, U., Findenegg, G. H., *Soft Matter*, **2012**, 8, 2573. Copyright 2012 The Royal Society of Chemistry.

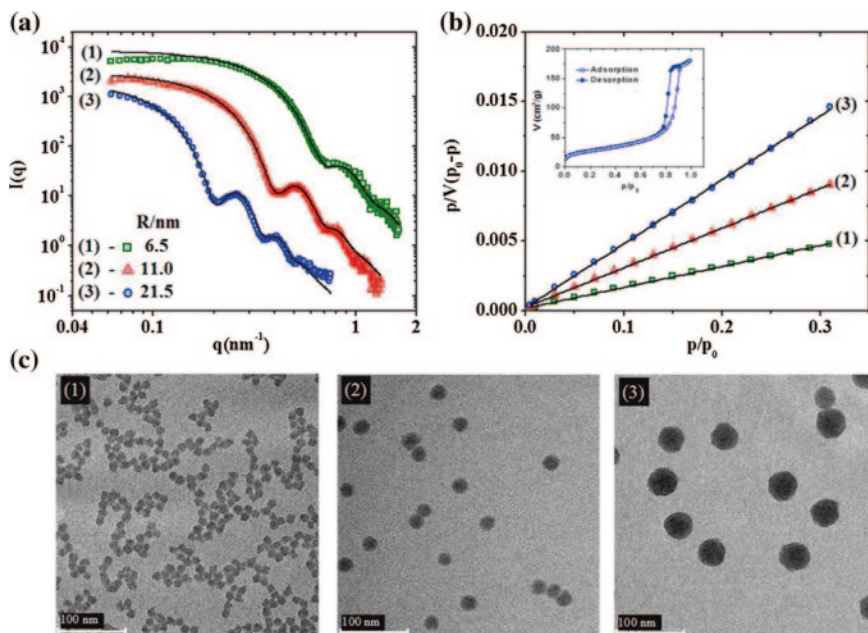


Fig. 4.1 Characterization of three Lys-Sil silica 1, 2 and 3: **a** Experimental SAXS profiles and fits to the points according to form factor of spheres dispersed in a medium. **b** BET-plot of N_2 adsorption isotherms (the inset is the measured complete isotherm for Lys-Sil-3 silica particles). **c** TEM images of the three Lys-Sil nanoparticles, shown at the same magnification

used Small Angle Neutron Scattering (SANS) to elucidate changes in surfactant self-assembly when adding increasing amounts of lysine to the silica dispersion. Based on these results we discuss the effects of surface curvature and anchoring strength of the surfactant heads on the adsorption of $C_{12}E_5$ at silica nanoparticles.

4.2 Results

4.2.1 Characterization of Silica Nanoparticles

Results of the characterization of three Lys-Sil materials by Small Angle X-ray Scattering (SAXS), nitrogen adsorption and Transmission Electron Microscopy (TEM) are shown in Fig. 4.1. The SAXS profiles of the three samples (Fig. 4.1a) can be represented by the form factor model of spherical particles having a log-normal size distribution. Values of the mean particle radius R and polydispersity σ of the three Lys-Sil materials are given in Table 4.1. The systematic deviations from the experimental $I(q)$ at low values of the scattering vector q can be attributed to repulsive long-range interactions between the charged particles at pH 9. These inter-particle features are of no relevance for the mean particle size and size distribution.

Table 4.1 Parameters for synthesis and characterization of three Lys-Sil samples: stirring rate r of the reaction mixture at temperature T , mean particle radius R and size polydispersity σ as derived from SAXS, and specific surface area a_{BET} of the sols as determined from the nitrogen adsorption measurements

| Silica | Synthesis | | SAXS | | N ₂ adsorpt. | |
|-----------|-----------|-----------|----------|----------|--------------------------------------|---------------------------------|
| | T (°C) | r (rpm) | R (nm) | σ | a_{BET} (m ² /g) | $a_{\text{BET}}/a_{\text{geo}}$ |
| Lys-Sil-1 | 60 | 1,300 | 6.5 | 0.13 | 293 | 1.40 |
| Lys-Sil-2 | 60 | 800 | 11.0 | 0.11 | 154 | 1.24 |
| Lys-Sil-3 | 70 | 300 | 21.5 | 0.10 | 95 | 1.50 |
| Ludox-TMA | – | – | 13.4 | 0.13 | 115 | 1.13 |

Polydispersity is expressed by the standard deviation from the mean particle size; a_{geo} is the geometric surface area

The specific surface area of the silica sols was determined from the nitrogen adsorption isotherms by the BET method in a range of relative pressures p/p_0 from 0.05 to 0.3 (Fig. 4.1b). The resulting values a_{BET} are given in Table 4.1 and compared with the geometric surface area per unit mass, $a_{\text{geo}} = 3/R\rho_{\text{SiO}_2}$, with R , the mean particle radius (from SAXS) and ρ_{SiO_2} , the density of silica (2.2 g cm⁻³).

4.2.2 Surfactant Adsorption on Lys-Sil Nanoparticles

Adsorption isotherms of the surfactant C₁₂E₅ at the three Lys-Sil sols at pH 7 and 20 °C are shown in Fig. 4.2. The graphs present the surface concentration Γ of the surfactant (amount adsorbed per unit area) versus Solution concentration expressed in the units of the critical micelle concentration ($cmc = 7 \times 10^{-5}$ M at 20 °C). The isotherms exhibit a steep increase in adsorption starting at an onset concentration below the cmc , and a plateau value that is reached shortly above the cmc . The isotherms can be represented by the S-type isotherm equation by Gu and Zhu [25, 26]

$$\Gamma = \Gamma_m \frac{K(c/cmc)^n}{1 + K(c/cmc)^n} \quad (4.1)$$

where Γ_m represents the maximum surface concentration (plateau value of the adsorption isotherm), K the adsorption constant and n is nominally the aggregation number of surface micelles. Fits of Eq. 4.1 to the adsorption data are shown by the full curves in Fig. 4.2 and the parameters are summarized in Table 4.2. Also given is the surface aggregation concentration c_0 , which can be calculated from the parameters K and n by Eq. 4.1 [25].

$$c_0/cmc = \left(\frac{n-1}{n+1} \right)^{(n+1)/n} K^{-1/n} \quad (4.2)$$

As indicated in Fig. 4.2, the uncertainty in the experimental values of Γ_m is large for the smallest particles. The uncertainty in c_0/cmc is estimated to ± 20 %.

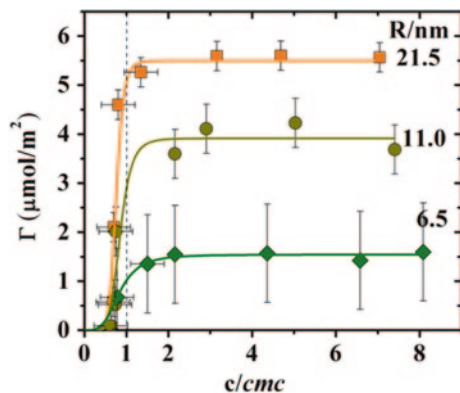


Fig. 4.2 Adsorption isotherms (20 °C) of the surfactant C_{12}E_5 at Lys-Sil silica particles of radius 6.5, 11 and 21.5 nm: Experimental data and fits by the Gu-Zhu equation. The dashed vertical line indicates the cmc of the surfactant

Table 4.2 Adsorption of C_{12}E_5 at Lys-Sil nanoparticles

| Silica | R (nm) | Γ_m ($\mu\text{mol m}^{-2}$) | K | n | c_0/cmc |
|-----------|----------|---------------------------------------|-----|-----|------------------|
| Lys-Sil-1 | 6.5 | 1.5 | 1.9 | 3.7 | 0.42 |
| Lys-Sil-2 | 11 | 3.9 | 2.8 | 6.2 | 0.58 |
| Lys-Sil-3 | 21.5 | 5.5 | 12 | 8.8 | 0.58 |

Fit of adsorption data of Fig. 4.2 by Eq. 4.1: maximum surface concentration Γ_m , adsorption constant K , nominal aggregation number of surface micelles n , and ratio of surface aggregation concentration to critical micelle concentration

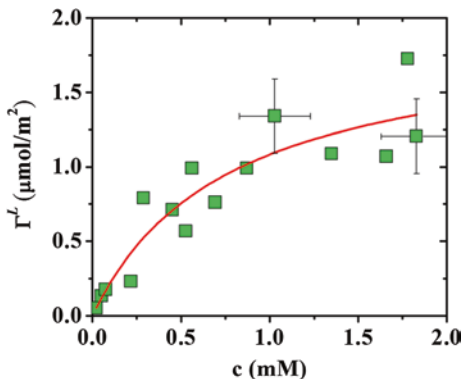
The most interesting aspect of the adsorption isotherms in Fig. 4.2 is the strong decrease of the limiting surface concentration Γ_m with decreasing size of the Lys-Sil particles. In preliminary adsorption measurements for C_{12}E_5 on pure siliceous Ludox-TMA particles ($R = 13.4$ nm) we found a plateau value $\Gamma_m = 4.5$ mmol m^{-2} , which fits into the size dependence of Γ_m observed with the Lys-Sil particles.

Yokoi et al. [27] investigated the formation and properties of Lys-Sil nanoparticles using a combination of liquid-state ^{13}C NMR, solid-state ^{13}C CP/MAS NMR, thermogravimetry, and differential thermal analysis. They concluded that a substantial fraction of lysine used in the particle synthesis remains adsorbed at the nanospheres. To find out in what way adsorbed lysine may affect the adsorption of the surfactant, we studied the adsorption of lysine on pure siliceous nanoparticles.

4.2.3 Lysine Adsorption on Silica Nanoparticles

The adsorption of lysine was studied on Ludox-TMA silica sol, as this material is free from any other organic base. The results are shown in Fig. 4.3. Within error limits the adsorption data can be represented by the Langmuir equation: $\Gamma^L = \Gamma_m^L bc / (1 + bc)$, where Γ^L is the surface concentration of lysine at equilibrium concentration c . We find a limiting surface concentration $\Gamma_m^L = 1.8$ $\mu\text{mol m}^{-2}$ (corresponding to a surface

Fig. 4.3 Adsorption isotherm of lysine on Ludox-TMA silica: experimental data and fit by the Langmuir equation



density of 1.1 nm^{-2}), and adsorption constant $b = 1.6 \text{ mM}^{-1}$. Our value of the limiting surface density is consistent with the value of 0.5 nm^{-2} reported by Yokoi [27] for the specific conditions of their particle synthesis. From here on, the amount of lysine adsorbed at silica nanoparticles will be expressed by the relative surface concentration $\theta = \Gamma^L / \Gamma_m^L$ to avoid mix-up with the adsorption of the surfactant.

4.2.4 SANS Study of Surfactant Aggregate Structure

SANS measurements were made to study surfactant aggregate structures at silica nanoparticles in the absence and presence of lysine. As in the preceding studies [19, 20], SANS measurements were made with a $\text{H}_2\text{O}/\text{D}_2\text{O}$ mixture that matches the scattering length density of the silica. In this contrast-match scenario the silica particles become invisible to the neutron beam. Hence in the absence of surfactant only a constant scattering background is observed, as shown in the inset in Fig. 4.4a. When surfactant is added, a scattering intensity profile $I(q)$ appears which is characteristic of the shape and size of the surfactant aggregates and their arrangement in space. Figure 4.4a shows the scattering profile for C_{12}E_5 in a 3.3 wt% Ludox-TMA silica dispersion at a surfactant concentration corresponding to $\Gamma = 3.5 \mu\text{mol m}^{-2}$, (i.e., well below the limiting adsorption, $\Gamma_m = 4.5 \mu\text{mol m}^{-2}$). Also shown in Fig. 4.4a is the scattering profile of the surfactant in the absence of silica, measured at a similar concentration but in pure D_2O , to enhance the scattering contrast. The scattering curve for C_{12}E_5 in the absence of silica can be represented quantitatively by the form factor model of wormlike micelles. The resulting fit parameters are given in Table 4.3. The scattering profile of the surfactant in contact with silica particles was analyzed in terms of two different models: (i) a spherical shell model [17], assuming that the surfactant is forming a layer of uniform thickness L ; (ii) the micelle-decorated bead model [28, 29], assuming a random distribution of N spherical surface micelles of radius R_m located at distance $R + R_m$ from the center of the silica particle. The parameters used to fit the data are given in Table 4.3. Figure 4.4b shows that both models give a fair representation of the experimental data in the low- q regime including the local maximum near $q = 0.3 \text{ nm}^{-1}$. For higher q the shell model

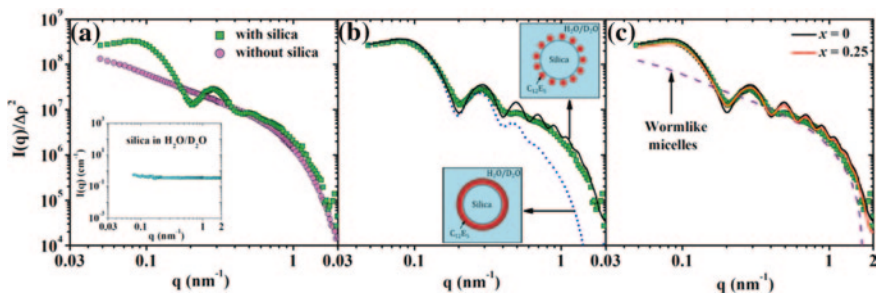


Fig. 4.4 SANS intensity profiles $I(q)$ for the surfactant $C_{12}E_5$ in a 3.3 wt% Ludox-TMA dispersion ($\Gamma = 3.5 \mu\text{mol m}^{-2}$) at silica/water contrast match conditions: **a** comparison of scattering profiles in presence of silica particles (*squares*) and the corresponding amount of surfactant in the absence of silica particles (*circles*) (the inset shows the contrast match of silica in absence of surfactant); **b** fit of the scattering curve by the shell model (*dotted curve*) and the micelle-decorated bead model (*full curve*), with $R_m = 2.2$ and $N = 105$; **c** fit to the scattering curve accounting for the dual population of the 25 % surfactant as wormlike bulk micelles (*red line*) and rest adsorbed; the dashed curve in the curve is the form factor of the wormlike micelle

Table 4.3 Analysis of SANS data for $C_{12}E_5$ adsorbed on Ludox-TMA particles by the micelle-decorated bead model and spherical shell model

| | Γ ($\mu\text{mol m}^{-2}$) | R_{bead} (nm) | R_m (nm) | $\Delta\rho$ ($\times 10^{-4} \text{ nm}^{-2}$) | N_{mic} | L (nm) | x |
|---------------|--|------------------------|------------|--|------------------|----------|------|
| Surf-micelles | 3.5 | 13.37 | 2.2 | 2.36 | 105 | – | 0.25 |
| Shell | 3.5 | 13.37 | – | 2.36 | – | 4.0 | – |

R_m is the radius of surface micelles and L is the thickness of shell according to core shell model

predicts a steeper decrease of $I(q)$ than the observed scattering curve. This deviation indicates that the shell model underestimates the overall surface area of the surfactant aggregates. The micelle-decorated bead model gives a satisfactory fit of the entire scattering curve. The higher-order oscillations in the region of $q > 0.4 \text{ nm}^{-1}$ produced by this model are caused by artifacts arising from the Fourier transformation of the pair-correlation function of surface micelles used to derive the inter-micellar structure factor. This pair-correlation function was generated by simulating random distributions of N spherical micelles on the silica bead (see Sect. 3.1.1). We stress that we have not attempted to determine the detailed shape of the surface micelles, but the model of spherical surface micelles was adopted for the sake of simplicity.

However, we have tested if the fit can be further improved by assuming that a part of the surfactant is not adsorbed but exists in form of free wormlike micelles. Specifically, the total scattering intensity was represented by

$$I(q) = (1 - x)I_{\text{surf}}(q) + xI_{\text{bulk}}(q) \quad (4.3)$$

where $I_{\text{surf}}(q)$ and $I_{\text{bulk}}(q)$ represent the scattering intensity functions of the micelle-decorated bead model and the model of free cylindrical micelles, respectively, and x is the fraction of scattering intensity contributed by the free micelles. Figure 4.4c shows that Eq. 4.3 with $x = 0.25$ gives indeed some improvement of the fit. However, more systematic studies and consideration of the finite experimental resolution of the SANS

data (experimental smearing) would be necessary to discriminate between the small differences of the two models. The limitations of Eq. 4.3 to account for the co-existence of two populations of surfactant micelles in the system are discussed below.

To establish the effect of lysine on the aggregate structure of the surfactant in the silica dispersion, SANS measurements were made for a set of samples of fixed concentration of $C_{12}E_5$ (20 mM) in a 3.3 wt% dispersions of Ludox-TMA and with gradually increasing concentrations of lysine. From the known adsorption isotherm of lysine on Ludox-TMA (Fig. 4.3) its amount in the samples was adjusted such as to cover a wide range of surface concentrations while keeping the concentration of free lysine in the solution as low as possible ($c < 3$ mM). Scattering profiles for lysine surface concentrations θ from 0.004 to 0.76 are presented in Fig. 4.5a. It can be seen that the peak in $I(q)$ at $q \simeq 0.3 \text{ nm}^{-1}$, which is a measure of the amount of surfactant forming the adsorbed layer, decreases in height as the lysine concentration at the surface increases. A small peak is still detectable at a lysine surface concentration $\theta = 0.62$, but the peak has vanished at $\theta = 0.76$. The scattering profile at this highest lysine concentration resembles the profile obtained for the surfactant in the absence of silica (cf. Figure 4.4a). This clearly indicates that at $\theta > 0.75$ all surfactant has been displaced from the surface of the silica particles and is forming wormlike micelles in the aqueous phase. This conclusion is justified as it was confirmed by SANS measurements that lysine does not affect the scattering profile of $C_{12}E_5$ in the absence of the silica (not shown), and hence has no significant influence on the morphology of the bulk micellar aggregates at the lysine concentrations relevant in the present context. Quantitative modeling of the scattering profiles in terms of two co-existing populations of surfactant aggregates (surface micelles and bulk aggregates) in the presence of lysine was not practicable because too many of the relevant parameters were unknown. Instead, we checked if the gradual change of the scattering profile as a function of added lysine can be represented by Eq. 4.3, i.e., an incoherent superposition of contributions from surface micelles and free cylindrical micelles as in the bulk solution. Results for $x = 0$ (all surfactant forming spherical surface micelles), $x = 1$ (all surfactant forming wormlike micelles in solution) and intermediate states with $x = 0.25, 0.5$ and 0.75 are shown in Fig. 4.5b. The parameters used for simulating individual form factors of a silica bead with adsorbed surface micelles ($P_{surf-mic}(q)$) and free wormlike micelles in the bulk ($P_{worm}(q)$) are given in Table 4.4. It can be seen that the simulated curves reproduce the trends of the experimental scattering profiles as a function of θ (Fig. 4.5a).

Closer inspection of the SANS profiles in Fig. 4.5a reveals that the main oscillation in $I(q)$ shifts to lower values of q as the surface concentration θ of lysine increases. In terms of the simple core-shell model, this shift corresponds to an increase in the mean layer thickness from 4 nm to roughly 6 nm. This suggests that small surface concentrations of lysine are causing only partial detachment of the oxyethylene head groups of the surfactant, connected with a rehydration of these groups. Hence the lysine-induced weakening of the binding of surfactant to the surface may involve the formation of a water-rich layer between the surfactant aggregates and the surface, which ultimately leads to the complete detachment and reorganization of the surfactant aggregates. This finding is reminiscent of the effect of temperature on the layer of $C_{12}E_5$ at silica particles as reported by Cummins et. al. [17] which was attributed to a temperature-induced reorganization and partial desorption of the surfactant.

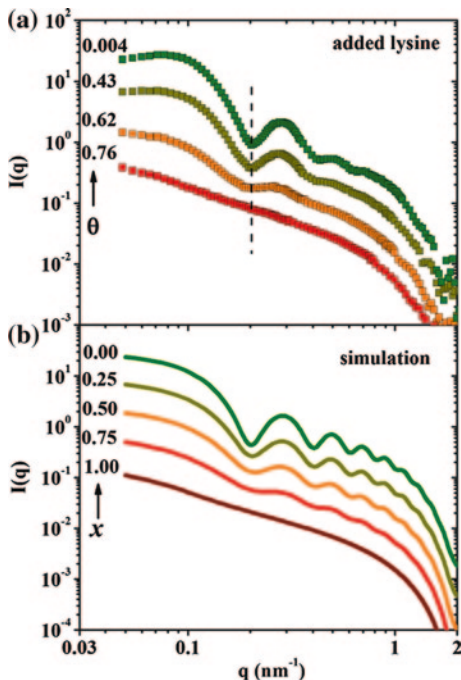


Fig. 4.5 **a** SANS experimental scattering curves for $C_{12}E_5$ in a 3.3 wt% dispersion of Ludox TMA with increasing lysine concentration corresponding to relative surface concentrations θ from 0.004 to 0.76; **b** simulation of data in **(a)** based on Eq. 4.3 with weight factor x of bulk micelles as given in the graph. In **(a)** and **(b)** curves for higher θ or x are shifted downward by factors of 3

Table 4.4 Parameters used to simulate the form factors of spherical surface micelles and bulk wormlike micelles as further used in Eq. 4.3

| $P_{\text{surf-mic}}(q)$ | | | | $P_{\text{worm}}(q)$ | | | |
|--------------------------|-------------------|------------------|---------------------|----------------------|------------------------|------------|------------|
| R_{bead} (nm) | s_{bead} | N_{mic} | R_{m} (nm) | s_{mic} | R_{worm} (nm) | L_c (nm) | L_k (nm) |
| 13.37 | 0.13 | 100 | 2.2 | 0.1 | 2.0 | 142 | 40.5 |

R_{bead} is the radius of the silica particle, s_{bead} its polydispersity, and s_{mic} is the polydispersity of the surface micelles. Whereas R_{worm} is the radius, L_c and L_k are the contour and Kuhn length of wormlike bulk micelles

4.3 Discussion

4.3.1 Size Dependence of the Adsorption of $C_{12}E_5$ on Lys-Sil

The sigmoidal shape of the adsorption isotherms in Fig. 4.2 is a well-known signature of aggregative adsorption of nonionic surfactants at hydrophilic surfaces [11, 14, 16, 25]. On the other hand, the strong decrease of the maximum surface

concentration of the surfactant with decreasing size of the Lys-Sil nanoparticles represents a remarkable new result. To our knowledge such a pronounced size effect on the adsorption has not been reported previously. This may be due to the difficulty of preparing oxide nanoparticles of well-defined size in this size range and determining the precise concentration of surfactant in the dispersion. Here we will discuss this finding from a point of view of the different structures of surfactant aggregates at the surface of the nanoparticles and in solution.

The SANS measurements presented in Sect. 4.2.4 have established that $C_{12}E_5$ is forming discrete surface aggregates at the Ludox-TMA silica particles, in agreement with our earlier findings with $C_{12}E_5$ at Stöber-type silica nanoparticles of similar size (16 nm) [19]. In that paper we conjectured that surface micelles are preferred because the high surface curvature of small particles prevents an effective packing of surfactant molecules in a bilayer film. For a particle of radius R with an adsorbed bilayer film of thickness L the area at the midpoint plane of the bilayer exceeds the surface area of the particle by a factor $f = (1 + L/2R)^2$. For the present Lys-Sil particles and a bilayer thickness of 4 nm we have $f = 1.2$ for the largest particles ($R = 21.5$ nm), but $f = 1.7$ for the smallest particles ($R = 6.5$ nm). For large particles this curvature-induced handicap may be met by formation of an asymmetric bilayer, having a higher number of molecules in the outer layer. For the smallest particles, on the other hand, it appears that the curvature-induced handicap is too high for any form of bilayer structure. Instead, self-assembly apparently leads to discrete, more highly curved surface aggregates, as indicated by the SANS study. As shown above for $C_{12}E_5$ at Ludox-TMA particles, the data can be represented by spherical surface micelles of about 4.4 nm in diameter. Assuming that this also pertains to $C_{12}E_5$ adsorbed at the Lys-Sil particle, we may estimate the number of surface micelles per particle from the adsorption isotherms of the surfactant. The volume of adsorbed surfactant per particle at the plateau of the adsorption isotherm is given by $V_a = A\Gamma_m N_A v_a$, where $A = 4\pi R^2$ is the surface area of a particle of radius R , N_A is the Avogadro constant, and v_a the volume of a surfactant molecule ($v_a = 0.97$ nm³ for $C_{12}E_5$ hydrated with 10 water molecules [9]). The number of surface micelles per particle is then given by $N = V_a/v_m$, with $v_m = (4\pi/3)R_m^3$, where R_m is the radius of a surface micelle. The maximum number of micelles that can be accommodated at the particle surface can be estimated as $N_{max} = A'/a_m$, with $A' = 4\pi(R + R_m)^2$ and a_m the effective cross-sectional area of a surface micelle, which we approximate by $a_m = 4R_m^2$, assuming a square lattice. Values of N and N_{max} for surface micelles of radius $R_m = 2.2$ nm at the three Lys-Sil nanoparticles are given in Table 4.5. These values indicate that the fraction of surface occupied by adsorbed micelles is strongly increasing with the particle size. For the smallest particles ($R = 6.5$ nm), this estimate yields $N/N_{max} \approx 0.2$, i.e., only a relatively small fraction of the surface is occupied with surface micelles. For the largest particles ($R = 21.5$ nm), on the other hand, our estimate yields $N/N_{max} > 1$, suggesting that for particles of this size the surfactant is not forming spherical surface micelles but aggregates which allow a higher packing density at the surface. This finding is plausible in view of the fact that $C_{12}E_5$ is forming flat (patchy) bilayer structures at planar surfaces [11, 12].

Table 4.5 Adsorption of $C_{12}E_5$ on Lys-Sil silica nanoparticles of radius R : measured maximum surface concentration Γ_m (Fig. 4.1), estimated number of spherical surface micelles ($R_m = 2.2$ nm) per silica particle, N , and N/N_{max}

| Silica | R (nm) | Γ_m ($\mu\text{mol m}^{-2}$) | N | N/N_{max} |
|-----------|----------|---------------------------------------|-----|-------------|
| Lys-Sil-1 | 6.5 | 1.5 | 10 | 0.21 |
| Lys-Sil-2 | 11 | 3.9 | 77 | 0.68 |
| Lys-Sil-3 | 21.5 | 5.5 | 417 | 1.14 |

Here N_{max} is the maximum number of surface micelles that can be accommodated at a particle of given radius (see text)

A particle-size induced transition from surface micelles to a surfactant bilayer can be rationalized by considering that adsorption of a surfactant bilayer on a curved surface involves bending the bilayer, and that the bending energy needed to wrap the particle can be balanced by the adhesion energy of the adsorbed layer. This is the essence of a phenomenological model by Lipowsky and Döbereiner [30] which predicts a transition from the naked particle to the particle wrapped by the bilayer to occur at a critical particle radius $R_c = \sqrt{2\kappa/|w_{bi}|}$, where κ is the effective bending constant of the bilayer and w_{bi} the adhesion area per unit area. Small surface micelles may be adsorbed also on particles of radius $R < R_c$, but due to the less effective packing, their adhesion energy per unit area, w_{mic} , will be smaller than that for an extended bilayer. On the basis of this argument we may expect a transition from a dense layer of micelles to a uniform bilayer to occur at a particle radius $R_{tr} = \sqrt{2\kappa/|w_{bi} - w_{mic}|}$. For surfactant bilayers we expect a bending constant $\kappa \approx 5kT$ and an attractive van der Waals interaction per unit area of the silica surface $w_{bi} \approx kT$. However, $|w_{bi} - w_{mic}|$ may be much smaller than w_{bi} . Assuming $|w_{bi} - w_{mic}| = 0.025kT$ leads to a transition at a radius $R_{tr} = 20$ nm, which is roughly the particle radius suggested by the analysis of the adsorption data (Table 4.5). Hence this model may explain the transition from discrete surface micelles to a uniform bilayer, but not the pronounced decrease of the number of surface micelles per unit area observed for the smaller particles. This size dependence of the surface concentration is considered in the following section.

4.3.2 Effect of Lysine on Binding Strength of Surfactant

In order to gain some understanding for the low surface concentration of the surfactant at the smallest silica particles we need to look more closely at the anchoring of the surface micelles. For surfactants of the poly(oxyethylene)alkyl ether type, such as $C_{12}E_5$, on hydrophilic silica, it is believed that hydrogen bonding of the silanol groups to the ether groups of the surfactant, either directly [31, 32] or mediated by water molecules [16], represents the dominant binding mechanism. To attain the necessary number of such bonds, surface micelles must acquire a sufficiently large contact area with the surface, which generally will imply some distortion of micellar shape relative to that in solution. For convex-shaped micelles the degree of distortion will depend on the mean curvature of the solid surface, being weakest at concave surfaces (as in nanopores) [33]

and largest at spherical nanoparticles. Since the strain energy caused by distortion of the surface micelles is of opposite sign as the binding energy, surface micelle formation will become less favorable the higher the surface curvature of the particles. Accordingly, fewer surface micelles will be formed per unit area as the particle size decreases. Hence the concept of strained surface micelles may explain the observed decrease in the number of surface micelles with decreasing particle radius (Table 4.5).

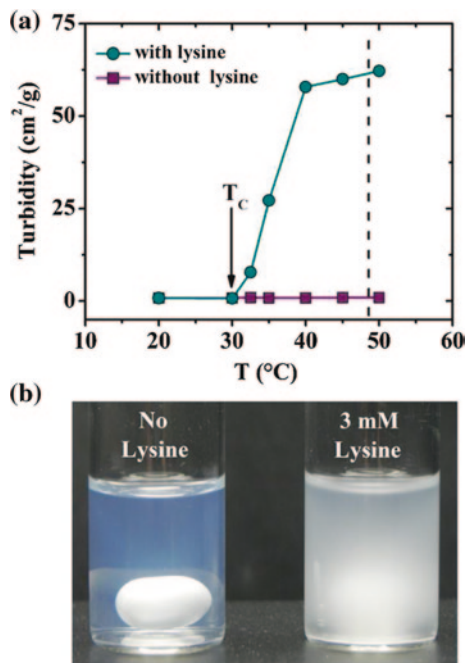
The observed displacement of surfactant from the surface of the silica particles induced by adsorption of lysine may be rationalized on the basis of these arguments. Lysine is more strongly adsorbed to the silica surface than the surfactant by hydrogen bonds between the weakly acidic silanol groups and the basic terminal amino group of lysine. Accordingly, adsorption of lysine causes a decrease in the number density of free silanol groups at the silica particles and thus a weaker binding of the surface micelles. As can be seen in Fig. 4.5, the increase in the surface concentration θ of lysine (Fig. 4.5a) indeed correlates directly with the fraction x of displaced surfactant (Fig. 4.5b).

Finally, we discuss the possible influence of lysine on the size dependence of the adsorption of $C_{12}E_5$ at the Lys-Sil nanoparticles (Fig. 4.2). Since the three samples of Lys-Sil were synthesized from the same reaction mixture, and particle size was tuned solely by the stirring rate and a weak temperature increase (see Table 4.1), we believe that the surface density of lysine and silanol groups was independent of particle size. This is in line with earlier published results on similar silica particles [27], where the surface density of lysine on the Lys-Sil particles was estimated to be 0.5 nm^{-2} , and a value 3 nm^{-2} was adopted for the surface density of silanol groups as reported previously by Shenderovich et al. [34] From these values the fraction of silanol groups blocked by lysine was estimated to be 15 %. This then implies that the surface density of free silanol groups at the Lys-Sil particles will be lower than for pure Stöber-type or Ludox-type silica. On the assumption that the binding strength of surface micelles of $C_{12}E_5$ is proportional to the surface density of free silanol, we may expect that the number of surface micelles on the Lys-Sil particles will be smaller than on Stöber-type or Ludox-type particles of equal size. Furthermore, we propose that this effect should be more pronounced for small, highly curved silica particles because in this case the straining energy would be higher than on larger particles. This conjecture is supported by the results of the earlier study of $C_{12}E_5$ at Stöber-type silica nanoparticles of radius 8 nm [19], for which a significantly higher limiting surface concentration was found than on the present Lys-Sil particles of radius 11 nm. However, more systematic work is needed to corroborate this combined influence of particle size and density of binding sites.

4.3.3 Potential Application Relevance

The finding that a nonionic surfactant can be displaced readily from the surface of nanoparticles by small amounts of a more strongly adsorbed substance is of practical relevance for the formulation of dispersions stabilized by such surfactants. In

Fig. 4.6 **a** Turbidity of 5.2 mM $C_{12}E_5$ in a 1 wt% dispersion of Ludox-TMA without lysine (*squares*) and with 3 mM lysine (*circles*); **b** photograph of the two constantly stirred samples at a temperature well above the cloud point T_c (*dashed line* in **a**)



addition, the displaced surfactant can cause significant changes in the macroscopic behavior of the system. Since non-ionic surfactants like $C_{12}E_5$ are forming worm-like micelles in a wide temperature and concentration range their displacement from the surface can affect the rheological behavior of the system [35]. For these surfactants it is even possible that the displacement of the surfactant drives the system from the one-phase region into the two-phase region of the surfactant + water phase diagram. For the present system this is demonstrated in Fig. 4.6. The phase diagram of the $C_{12}E_5$ + water exhibits a lower critical point (cloud point) at about 31 °C and 1 wt% surfactant [36]. Above this temperature the system separates into a water-rich and a surfactant-rich phase. Figure 4.6a shows the turbidity versus temperature of a 1 wt% Ludox-TMA dispersion containing 0.2 wt% $C_{12}E_5$, without and with added lysine. In the absence of lysine almost all surfactant is adsorbed at the particles (surface concentration $\Gamma = 4 \mu\text{mol m}^{-2}$, i.e., close to the limiting adsorption). The turbidity of this sample is moderately low and independent of temperature up to 50 °C. In the presence of lysine (3 mM), however, when the surfactant is detached from the particles, the turbidity of the stirred sample strongly increases at temperatures $T > T_c$, as most of the free surfactant is now forming droplets of the surfactant-rich phase. The silica particles remain dispersed in the aqueous phase. SAXS measurements on the samples without and with lysine show no increased intensity in the Guinier regime at different temperatures, confirming the absence of any aggregation of silica nanoparticles [37]. The scattering curves taken at temperatures from 20 to 50 °C superimpose (not shown). Photograph of

the samples without and with lysine at a temperature above T_c are also shown in Fig. 4.6b. This is a striking example to show the potential significance of such displacement effects for the formulation of nanoparticle dispersions with nonionic surfactants. Related phenomena were reported recently by Mustafina et al. [38].

4.4 Conclusions

This study has shown that the self-assembly of surfactants in a dispersion of nanoparticles can be tuned by an additive which modifies the surface energy by adsorption onto the particles. Lysine acts as an effective surface modifier in the present system. Small concentrations of lysine cause a complete displacement of the surfactant $C_{12}E_5$ from silica particles. SANS measurements reveal that the displacement process represents a morphological transition from discrete surface micelles attached to the particles to elongated (wormlike) micelles in the aqueous bulk phase. The detachment seems to proceed via an intermediate state in which a hydrated layer of adsorbed lysine intercalates between the surfactant aggregates and the surface. Further SANS studies are needed to elucidate this process.

For Lys-Sil particles we find a pronounced decrease of the maximum surface concentration of the surfactant with decreasing particle size. Our study suggests that this size effect is caused by the adsorbed layer of lysine, which reduces the binding strength of the surfactant head groups, in combination with the increasing curvature of the solid surface. For the smallest particles (diameter 13 nm) only a fraction of their surface is decorated with surface micelles. We speculate that this may be a consequence of a stronger distortion of surface micelles that is needed for attaining a sufficiently large contact area with the surface of small particles when some of the sites are blocked by lysine. The much higher limiting adsorption of the surfactant at the largest particles (43 nm) indicates that in this case the surfactant is not forming discrete surface micelles but less highly curved aggregates which allow a higher packing density at the surface. We present a simple model to account for such a transition in surface aggregate structure. Hence, this study can contribute to a better understanding of the factors controlling the self-assembly of surfactants at nanoparticles. This will be useful in the formulation of nanoparticle dispersions and their application in particle nanotechnology.

References

1. Holmberg K, Shah DO, Schwuger MJ (eds) (2002) Handbook of Applied Surface and Colloid Chemistry. Wiley, New York
2. Paria S, Khilar KC (2004) A review on experimental studies of surfactant adsorption at the hydrophilic solid-water interface. *J Colloid Interface Sci* 110:75
3. Limbach LK, Bereiter R, Müller E, Krebs R, Gälli R, Stark WJ (2008) Removal of oxide nanoparticles in a model wastewater treatment plant: influence of agglomeration and surfactants on clearing efficiency. *Environ Sci Technol* 42:5828

4. Veronovski N, Andeozzi P, Mesa CL, Smol MS, Ribitsch V (2010) Use of Gemini surfactants to stabilize TiO₂ P25 colloidal dispersions. *Colloid Polym Sci* 288:387
5. Zhang R, Somasundaran P (2006) Advances in adsorption of surfactants and their mixtures at solid/solution interfaces. *Adv Colloid Interface Sci* 123–126:213
6. Klimenko NA, Koganovs AM (1974) Adsorption of nonionic surfactants in associated state from aqueous solutions on porous sorbents. *Kolloidn Zh* 36:151
7. Klimenko NA, Kofanov VL, Sivalov EG (1981) Spectrophotometric study of the adsorption of non-ionic surfactant micelles on large-pore silica-gel. *Kolloidn Zh* 43:287
8. Levitz P (1991) Aggregative adsorption of nonionic surfactants onto hydrophilic solid/water interface. Relation with bulk micellization. *Langmuir* 7:1595
9. Böhmer MR, Koopal LK, Janssen R, Lee EM, Thomas RK, Rennie AR (1992) Adsorption of nonionic surfactants on hydrophilic surfaces. An experimental and theoretical study on association in the adsorbed layer. *Langmuir* 8:2228
10. Manne S, Gaub HE (1995) Molecular organization of surfactants at solid-liquid interfaces. *Science* 270:1480
11. Tiberg F (1996) Physical characterization of non-ionic surfactant layers adsorbed at hydrophilic and hydrophobic solid surfaces by time-resolved ellipsometry. *J Chem Soc Faraday Trans* 92:531
12. Grant LM, Tiberg F, Ducker WA (1998) Nanometer-scale organization of ethylene oxide surfactants on graphite, hydrophilic silica, and hydrophobic silica. *J Phys Chem B* 102:4288
13. Steitz R, Müller-Buschbaum P, Schemmel S, Cubitt R, Findenegg GH (2004) Lateral structure of a surfactant layer adsorbed at a hydrophilic solid/liquid interface. *Europhys Lett* 67:962
14. Dietsch O, Eltekov A, Bock H, Gubbins KE, Findenegg GH (2007) Crossover from normal to inverse temperature dependence in the adsorption of nonionic surfactants at hydrophilic surfaces and pore walls. *J Phys Chem C* 111:16045
15. Penfold J, Staples E, Tucker I (2002) On the consequences of surface treatment on the adsorption of nonionic surfactants at the hydrophilic silica-solution interface. *Langmuir* 18:2967
16. Matsson MK, Kronberg B, Claesson PM (2004) Adsorption of alkyl polyglucosides on the solid/water interface: equilibrium effects of alkyl chain length and head group polymerization. *Langmuir* 20:4051
17. Cummins PG, Penfold J, Staples E (1992) Nature of the adsorption of the nonionic surfactant pentaethylene glycol monododecyl ether on a ludox silica sol. *J Phys Chem* 96:8092
18. Penfold J, Staples E, Tucker I, Cummins P (1996) Adsorption of nonionic surfactants on silica sol particles: the effects of sol type and concentration, surfactant type, concentration, and temperature. *J Phys Chem* 100:18133
19. Lugo DM, Oberdisse J, Karg M, Schweins R, Findenegg GH (2009) Surface aggregate structure of nonionic surfactants on silica nanoparticles. *Soft Matter* 5:2928
20. Lugo DM, Oberdisse J, Lapp A, Findenegg GH (2010) Effect of nanoparticle size on the morphology of adsorbed surfactant layers. *J Phys Chem B* 114:4183
21. Sharma KP, Aswal VK, Kumaraswami G (2010) Adsorption of nonionic surfactant on silica nanoparticles: structure and resultant interparticle interactions. *J Phys Chem B* 114:10986
22. Kumar S, Aswal VK (2011) Tuning of nanoparticle–surfactant interactions in aqueous system. *J Phys Condens Mat* 23:035101
23. Ahualli S, Iglesias GR, Wachter W, Dulle M, Minami D, Glatter O (2011) Adsorption of anionic and cationic surfactants on anionic colloids: supercharging and destabilization. *Langmuir* 27:9182
24. Davis TM, Snyder MA, Krohn JE, Tsapatsis M (2006) Nanoparticles in lysine-silica sols. *Chem Mater* 18:5814
25. Gu T, Zhu B-Y (1990) The S-type isotherm equation for adsorption of nonionic surfactants at the silica gel–water interface. *Colloids Surf* 44:81
26. Zhu B-Y, Gu T, Zhao X (1989) General isotherm equation for adsorption of surfactants at solid/liquid interfaces. Part 2. Applications. *J Chem Soc Faraday Trans I* 85:3819

27. Yokoi T, Wakabayashi J, Otsuka Y, Fan W, Iwama M, Watanabe R, Aramaki K, Shimojima A, Tatsumi T, Okubo T (2009) Mechanism of formation of uniform-sized silica nanospheres catalyzed by basic amino acids. *Chem Mater* 21:3719
28. Despert G, Oberdisse J (2003) Formation of micelle-decorated colloidal silica by adsorption of nonionic surfactant. *Langmuir* 19:7604
29. Oberdisse J (2004) Small angle neutron scattering and model predictions for micelle-decorated colloidal silica beads. *Phys Chem Chem Phys* 6:1557
30. Lipowsky R, Döbereiner H-G (1998) Vesicles in contact with nanoparticles and colloids. *Europhys Lett* 43:219
31. Partyka S, Zaini S, Lindheimer M, Brun B (1984) The adsorption of non-ionic surfactants on a silica gel. *Colloids Surf* 12:255
32. Trens P, Denoyel R (1993) Conformation of poly(ethylene glycol) polymers at the silica/water interface: a microcalorimetric study. *Langmuir* 9:519
33. Müter D, Shin T, Demé B, Fratzl P, Paris O, Findenegg GH (2010) Surfactant self-assembly in cylindrical silica nanopores. *J Phys Chem Lett* 1:1442
34. Shenderovich IG, Mauder D, Akcakayiran D, Buntkowsky G, Limbach H-H, Findenegg GH (2007) NMR provides checklist of generic properties for atomic-scale models of periodic mesoporous silicas. *J Phys Chem B* 111:12088
35. Strey R (1996) I. Experimental facts: water-nonionic surfactant systems, and the effect of additives. *Ber Bunsenges Phys Chem* 100:182
36. Strey R, Schomäcker R, Roux D, Nallet F, Olsson U (1990) Dilute lamellar and L_3 phases in the binary water- $C_{12}E_5$ system. *J Chem Soc Faraday Trans* 86:2253
37. Bharti B, Meissner J, Findenegg GH (2011) Aggregation of silica nanoparticles directed by adsorption of lysozyme. *Langmuir* 27:9823
38. Mustafina AR, Elistratova JG, Bochkova OD, Burirov VA, Fedorenko SV, Konovalov AI, Soloveva SY (2011) Temperature induced phase separation of luminescent silica nanoparticles in Triton X-100 solutions. *J Colloid Interface Sci* 354:644

Chapter 5

Assembling Wormlike Micelles in Tubular Nanopores by Tuning Surfactant-Wall Interactions

5.1 Introduction

Nanoporous materials with pores of uniform size and shape are of interest in many known application fields, ranging from catalysis, membrane processes, and chromatography to new areas such as microelectronics and medical diagnosis [1, 2]. Since surfactants or related amphiphilic substances are involved in many of these fields, their self-assembly in nano-confined space can play an important and diverse role in these applications. For instance, surfactant adsorption in narrow pores is of importance in surfactant-aided membrane processes such as micellar-enhanced ultrafiltration (MEUF) [3] or micellar liquid chromatography [4]. It is well-known that surfactants can improve the wettability of hydrophobic nanopores by adsorption of an oriented monolayer [5]. Surfactant adsorption onto hydrophilic surfaces can be regarded as a surface aggregation process, reminiscent of micelle formation in solution [6–9].

Up to now only a few experimental studies have addressed the effect of confinement on the structure of complex fluids in nanopores. X-ray reflectivity and holographic X-ray diffraction [10, 11] have been used to investigate confinement-induced ordering in complex liquids between planar parallel surfaces. Structural and dynamic aspects of the self-assembly of the nonionic surfactant $C_{12}E_5$ in porous glass were studied by 1H NMR [12]. Recently, we have adopted Small-Angle Neutron Scattering (SANS) to characterize adsorbed layers of this and other nonionic surfactants in the cylindrical pores of SBA-15 periodic mesoporous silica [13, 14]. SBA-15 is made up of micrometer-sized particles which constitute arrays of cylindrical nanopores arranged side-by-side in a 2D hexagonal lattice (space group P6mm) [15]. Due to the high mesoscale order of these materials structural information about the density profile of fluids in the pores can be derived by analyzing the intensities of the Bragg reflections [16, 17]. By applying this technique

Modified with permission from Bharti, B., Xue, M., Meissner, J., Cristigilo, V., Findenegg, G. H., *J. Am. Chem. Soc.*, **2012**, *134*, 14756. Copyright 2012 American Chemical Society.

to the study of surfactants in the pores of SBA-15 it was found that initially the adsorption of the surfactant in the pores leads to the formation of discrete surface aggregates which increase in number and eventually merge to interconnected bilayer patches as the plateau of the adsorption isotherm is approached [13, 14].

Recently we have found that the anchoring strength of the surfactant $C_{12}E_5$ to the surface of silica nanoparticles can be modified by co-adsorption of a more strongly adsorbed substance, such as the amino acid lysine [18]. In an earlier SANS study it had been shown that in the absence of lysine, the surfactant is forming discrete surface micelles at the silica nanoparticles [19]. When increasing doses of lysine were added to the silica dispersion a gradual transition from the surface micelles to detached wormlike micelles in the bulk solution was observed. It was now of interest to see if such a lysine-induced morphological transition from surface micelles to wormlike micelles in solution occurs in a similar way for surfactant adsorbed in nanopores, or if the behavior is affected by the confined geometry of the pore space. Similar to our previous studies, here again, we used SANS as a primary experimental tool, and we follow the evolution of the scattering profiles at different lysine adsorption levels. As a surprising result of this study we find that in a limited lysine adsorption regime cylindrical micelles are formed in the central space of the tubular pores. Before presenting the experimental details we give a brief summary of the theoretical background of this method where we present simulated scattering curves to illustrate the potential to distinguish between different aggregate morphologies of the surfactant.

5.2 Theoretical Background

As was shown in the preceding studies [13, 14], the scattering from surfactant aggregates in the pores of SBA-15 can be represented by a sum of three contributions: Bragg scattering from the pore lattice (I_{Bragg}), diffuse scattering from surfactant aggregates (I_{diff}) and a background (I_b) due to incoherent scattering, mostly arising from the protons of H_2O and surfactant, i.e.,

$$I(q) = I_{\text{Bragg}}(q) + I_{\text{diff}}(q) + I_b \quad (5.1)$$

where q represents the modulus of the scattering vector. When the scattering contrast between the silica matrix and the solvent is suppressed by using a H_2O/D_2O solvent mixture that matches the scattering length density of the matrix, then in the absence of surfactant only a q -independent background, I_b appears. In the presence of surfactant, diffuse scattering will arise due to the inhomogeneous distribution of the surfactant in the porous matrix. In previous studies of our group [14], it was found that over a wide range of surfactant fillings this diffuse scattering can be represented by a scattering function for disperse two-phase systems with spatial correlations, similar to the Teubner-Strey relation [20]

$$I_{\text{diff}}(q) = \frac{sI_m}{s + (1-s)(q/q_m - 1)^2} \quad (5.2)$$

where q_m and I_m represent the values of the scattering vector and scattering intensity at the correlation peak, and $s = I_0/I_m$, with I_0 the limiting value of $I_{diff}(q)$ for $q \rightarrow 0$. From these experimental parameters two characteristic lengths, d and ξ , can be derived: d represents the quasiperiodic distance between surfactant domains in the matrix, and ξ is a decay length of this quasiperiodic order. They are given in terms of q_m and s as

$$d = \frac{2\pi\sqrt{2}}{q_m} \left[\frac{1}{(1-s)^{1/2}} + 1 \right]^{-1/2}; \xi = \frac{\sqrt{2}}{q_m} \left[\frac{1}{(1-s)^{1/2}} - 1 \right]^{-1/2}. \quad (5.3)$$

When surfactant is present in the pores, contrast match between pore fluid and matrix is eliminated and Bragg reflections from the pore lattice appear. The radial average of the total scattering intensity for an ensemble of long cylindrical objects is given by

$$I_{Bragg}(q) = ZS_L(q)P(q) \quad (5.4)$$

where $S_L(q)$ is the structure factor of the pore lattice, $P(q)$ is the form factor of the scattering entity in a pore, which depends on the shape and geometry of the surfactant aggregates, and Z is a constant. For a perfect 2D-hexagonal lattice the spherically averaged structure factor is given by $S_L(q) = q^{-2} \sum_{hk} m_{hk} S_{hk}(q)$, where m_{hk} is the multiplicity of a Bragg peak with Miller indices hk ($m_{hk} = 6$ for the 10, 11, and 20 peaks), and S_{hk} represents delta functions at positions $q_{hk} = \left(\frac{4\pi}{a_0\sqrt{3}} \right) \sqrt{h^2 + k^2 + hk}$. In reality, the Bragg reflections are broadened due to lattice imperfections and limited instrumental resolution. In this work, they are represented by Gaussian functions $S_{hk}(q) = a_{hk} \exp[-b(q - q_{hk})^2]$, where a_{hk} is the amplitude of peak hk , and parameter b characterizes the width of the individual Bragg peak. The value of b was determined from the SANS curve of SBA-15 in D₂O and kept constant in the data analysis of all samples. The form factor $P(q)$ in Eq. 5.4 was modeled in different ways, to account for the different scattering patterns observed as a function of the added surface modifier (see below).

To demonstrate the effect of the distribution of surfactant, Fig. 5.1 shows simulated Bragg scattering curves for two different adsorption scenarios, namely, discrete surface micelles adsorbed to the pore-walls, and rod-like aggregates non-attached to the pore-wall. Also shown in Fig. 5.1 is the expected scattering behavior for the case that the surfactant is non-adsorbed but forms micelles outside the pore space. The parameters used in the simulations are summarized in Table 5.1.

1. Discrete surface micelles or patches: If the surfactant is forming surface micelles or bilayer patches at the pore walls, the statistical average of all patches (at contrast-match of the matrix by the aqueous phase) corresponds to the geometry of a hollow cylinder. Hence the form factor of a hollow cylinder, $P_{HC}(q)$, shown as the full line in Fig. 5.1a was adopted in Eq. 5.4. This causes a modulation of the Bragg scattering pattern (shaded area) from that of the original structure factor $S_{Bragg}(q)$ (dotted). Since the primary minimum of $P_{HC}(q)$ is situated at a q value near the (10) Bragg peak, this peak is reduced in intensity

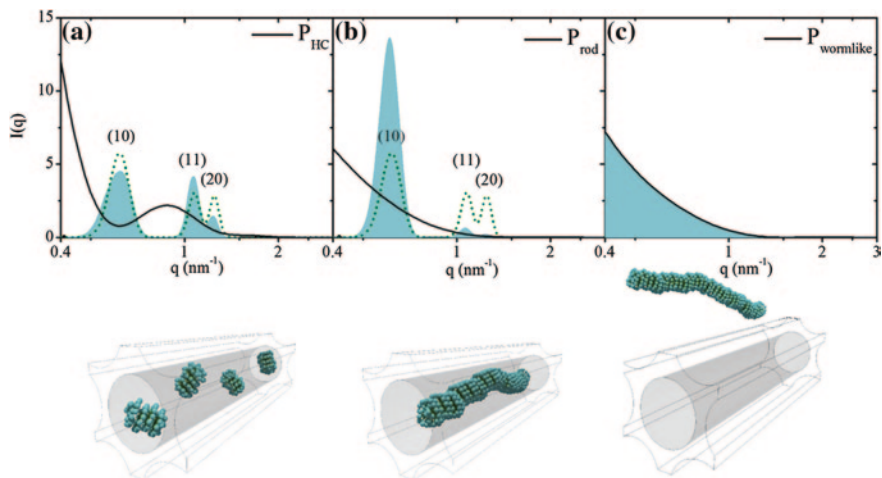


Fig. 5.1 Simulated scattering curves (filled region) and the cartoons corresponding for three plausible scenarios of $C_{12}E_5$ interaction with SBA-15 silica, where the surfactant forms **a** discrete patches adhering to the pore wall **b** isolated rod-like structures in the pores, and **c** free bulk wormlike micelles in the solution outside the pore. *Dotted lines* are the Gaussians curves implemented to mimic the Bragg peaks of ordered SBA-15 structure, where the numbers indicated in the brackets are the miller indices of the peaks. The *solid black lines* in **a**, **b** and **c** are the form factors of hollow cylinders, linear rods and wormlike [21] structures, respectively

Table 5.1 Parameters used in the simulation of the three surfactant scenarios of Fig. 5.1^a

| SBA-15 | $P_{HC}(q)$ | | $P_{rod}(q)$ | $P_{worm}(q)$ | |
|--------|-------------|------------|--------------|---------------|-------|
| a_0 | R_{HC} | ΔR | R_{rod} | R_{worm} | L_k |
| 11.6 | 2.5 | 2.5 | 2.5 | 2.5 | 10 |

^a a_0 , lattice parameter of the SBA-15 sample; R_{HC} and ΔR , radius and thickness of the cylinder shell; R_{rod} , radius of the cylindrical rod structure of surfactant aggregates in the pores; R_{worm} and L_k , radius and Kuhn length of the worm like surfactant aggregate in solution (all values in units of nm)

compared to that of the (11) and (20) peaks. The resulting distribution of peak intensities is a signature of a shell structure of the surfactant in the pores and was observed previously for the surfactant $C_{12}E_5$ in SBA-15 [14].

- Surfactant aggregates weakly interacting with the pore walls:** If the interaction between the surfactant and pore wall is weak, the self assembly of the surfactant in the pore may lead to aggregate structures similar to those in the bulk solution, which in the case of $C_{12}E_5$ is wormlike micelles. Such a scenario can be simulated by adopting the form factor of rods, $P_{rod}(q)$, in Eq. 5.4. The result of such a simulation is shown in Fig. 5.1b. It can be seen that the intensity of (10) Bragg peak is enhanced relative to (11) and (20) due to the superposition with the form factor of a rod-like aggregate structure.
- Micelles outside the pore space:** If the interaction of surfactant and pore wall is even weaker, formation of aggregates in the pores is disfavored against aggregation in the bulk solution for entropic reasons. Since no surfactant is

present in the pores, no Bragg scattering will occur in the contrast-match scenario ($I_{Bragg}(q) = 0$). Instead diffuse scattering from free micelles will occur, as shown in Fig. 5.1c for the case of wormlike micelles, based on the form factor of semi-flexible worms ($P_{worm}(q)$). Hence the absence of Bragg peaks is a signature for the case that no surfactant is adsorbed in the pore space.

In the simulations of Fig. 5.1a, b, the diffuse scattering contribution $I_{diff}(q)$ is neglected for simplicity. This is in accordance to Eq. 5.1, where the contributions from diffuse scattering and Bragg scattering are additive in good approximation, and thus will not affect the relative intensities of the Bragg peaks, which is characteristic for the different aggregate structures in the pores.

5.3 Experimental

5.3.1 Characterization of SBA-15

SBA-15 was synthesized as described previously [22] and characterized by nitrogen adsorption and Small-Angle X-ray Scattering (SAXS). Nitrogen adsorption measurements at 77 K were performed on a Gemini III 2,375 volumetric surface analyzer (Micromeritics). SAXS was performed on a SAXSess mc² instrument (Anton Paar, Austria), equipped with a Cu-K α , slit-collimated X-ray source operating at 40 kV (50 mA). Details of nitrogen adsorption and SAXS measurements are described elsewhere [23]. The lattice parameter (a_0) of the SBA-15 sample was determined from the SAXS data (see Appendix Fig. A.1a). The specific surface area (a_{BET}) was based on a BET plot of the nitrogen adsorption isotherm in the relative pressure range $0.05 < p/p_0 < 0.30$ (see Appendix Fig. A-1b). The diameter D of the cylindrical mesopores was determined from the mid-value of the pore condensation pressure $(p/p_0)_{pc}$ using the improved KJS prescription [24]. Characteristic parameters of the SBA-15 sample used in this study are given in Table 5.2.

5.3.2 Lysine Adsorption

The adsorption isotherm of lysine onto SBA-15 at 20 °C was determined by batch measurements using solution depletion analysis. Solutions of L-lysine monohydrate in water (10 ml) were adjusted to pH 8.0 and equilibrated with the SBA-15 powder (≈ 10 mg) in sealed plastic vials using a rotating mixer (12 h). After centrifugation (1 h at 9,500 g) the residual concentration of lysine in the supernatant was determined by reaction with ninhydrin to Ruhman's purple which was detected by its absorbance at 570 nm. The adsorption data was fitted with the *Langmuir* isotherm equation $n = n_m Kc / (1 + Kc)$, where n is the specific

Table 5.2 Characteristic parameters of the SBA-15 silica sample

| a_{BET} (m ² /g) | V_{sp} (cm ³ /g) | d (nm) | a_0 (nm) |
|-------------------------------|-------------------------------|----------|------------|
| 774 | 0.99 | 8.25 | 11.6 |

where a_0 is the lattice parameter, V_{sp} is the BJH desorption pore volume, a_{BET} is the BET specific surface area and d is the pore diameter

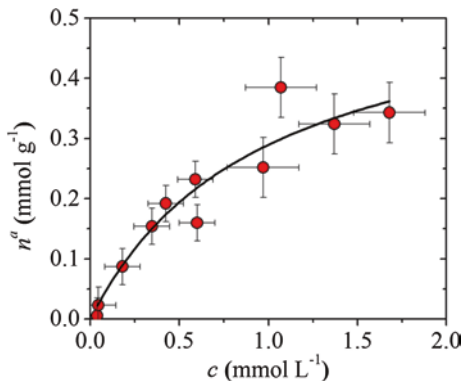
adsorption of lysine at equilibrium concentration c , n_m is the maximum adsorption, and K , the adsorption constant.

5.3.3 Sample Preparation and SANS Measurements

SANS measurements to determine the influence of lysine on the surfactant aggregate morphology in the pores of SBA-15 were performed with a H₂O/D₂O solvent mixture of 62.5 vol% D₂O, which in earlier studies was found to match the scattering length density of SBA-15 silica ($\rho_{silica} = 3.7 \times 10^{-4} \text{ nm}^{-2}$). A set of samples of fixed loading with surfactant, but increasing concentrations of lysine was prepared for the SANS measurements. Samples were prepared by adding SBA-15 powder (100 mg) to 10 ml of a solution of lysine of initial concentration c_0 in H₂O/D₂O at pH 6.5 and allowing time for adsorption of lysine in the pores. An amount of the surfactant nearly corresponding to the limiting adsorption n_m^S of C₁₂E₅ in SBA-15 (filling fraction $f = n^S/n_m^S \approx 0.95$) was then added. After equilibration (12 h in a rotating mixer) the supernatant was decanted and aliquots of the resulting silica slurry were transferred into the SANS sample cells. These specially designed cells [14] were made from aluminum with quartz glass windows (sample width 1 mm, sample volume, $V_{cell} = 0.1 \text{ cm}^3$). The sample cell was loaded with $30 \pm 3 \text{ mg}$ of SBA-15, with an associated mesopore volume of $30 \mu\text{L}$ (pore liquid) and $55 \mu\text{L}$ of extra-particle liquid. Variable amounts of silica directly affect the scattering intensity of the samples.

The limiting specific adsorption of C₁₂E₅ in the present SBA-15 material ($n_m^S = 1.15 \text{ mmol g}^{-1}$) was estimated from the measured value in the SBA-15 material used in the earlier work, and from the specific surface areas of the two silica materials. Due to the large surface area of SBA-15 and because the S-shaped adsorption isotherm reaches a plateau value shortly above the cmc, almost all surfactant is adsorbed in the pore space as long as the adsorbed amount remains below the plateau value. This limiting adsorption corresponds to a volume fraction of surfactant in the pore space [14] of $\phi \approx 0.40$. The fractional coverage of the SBA-15 surface with lysine was calculated from the experimental data as $\frac{n}{n_m} = \frac{V_l(c_0 - c)}{m_s n_m}$, with V_l the liquid volume, m_s the mass of silica, n_m the maximum adsorption per unit mass of silica, c_0 the initial concentration and c the equilibrium concentration of lysine in the sample volume. When expressing this concentration by the Langmuir isotherm, $c = \frac{\theta}{K(1-\theta)}$ (see Sect. 5.3.2), the fractional coverage θ is obtained from the equation

Fig. 5.2 Lysine adsorption isotherm (25 °C) at SBA-15 silica. The points are the measured experimental data and the solid line is fit according to *Langmuir* model



$$\theta^2 - \left(1 + ac_0 + \frac{a}{K}\right)\theta + ac_0 = 0 \quad (5.5)$$

where $a = V/m_s n_m$.

SANS measurements were made at the small-momentum-transfer diffractometer D16 at Institut Laue-Langevin (ILL, Grenoble). Two detector angles (0° and 12°) were chosen to access the scattering vector range $0.4 < q < 4 \text{ nm}^{-1}$, where $q = (4\pi/\lambda)\sin\theta$ and the scattering angle is 2θ at a neutron wave length $\lambda = 0.473 \text{ nm}$ (wavelength distribution $\Delta\lambda/\lambda = 0.01$). Due to technical problems the collimation of the neutron beam could not be optimized, which caused a loss of instrumental resolution as compared to the preceding experiments at D16.

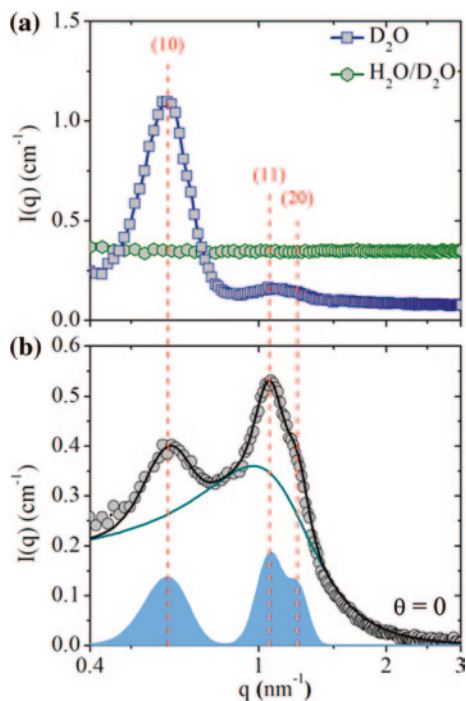
Data reduction and normalization was performed using the *LAMP* software [25], and *Scilab* [26] was used for the further data analysis and fitting. In the data analysis the uniform background I_b of Eq. 5.1 was first subtracted from the individual scattering curves, using the procedure described elsewhere [14]. In addition, a power-law term Aq^{-m} , with $A = 1.67 \times 10^{-3} \text{ cm}^{-1}$ and $m = 5.7 \pm 0.5$ was subtracted from the experimental $I(q)$ to account for the strong increase of the experimental scattering curves in the q range below the 10 Bragg peak ($q_{10} = 0.625 \text{ nm}^{-1}$), which we attribute to a superposition of Porod scattering from the outer surface of the silica granules (decorated with a surfactant bilayer) and the effect of imperfect masking of the primary neutron beam.

5.4 Results

5.4.1 Lysine Adsorption

The adsorption isotherm of lysine at the present SBA-15 sample at pH 8.0 is shown in Fig. 5.2, along with a fit of the data by the Langmuir equation. A maximum specific adsorption $n_m = 0.57 \text{ mmol g}^{-1}$ (corresponding to a surface concentration $\Gamma_m = n_m/a_s = 0.75 \text{ } \mu\text{mol m}^{-2}$) and adsorption constant $K = 1.0 \text{ mM}^{-1}$ was obtained.

Fig. 5.3 **a** SANS curves from SBA-15 immersed in pure D₂O (blue squares) and in the contrast-matching H₂O/D₂O mixture (green hexagons); the positions of the three leading Bragg reflections are indicated by dotted vertical lines. **b** Scattering profile from SBA-15 in H₂O/D₂O with the surfactant C₁₂E₅ at relative filling $f = 0.95$ in the absence of lysine ($\theta = 0$): the black line represents a fit to the data points (circles), with the diffuse scattering contribution $I_{\text{diff}}(q)$ according to Eq. 5.2 (green curve) and the Bragg scattering contribution $I_{\text{Bragg}}(q)$ according to Eq. 5.4 indicated by the contour of the shaded areas (see text)



The value of Γ_m is significantly lower than the adsorption of lysine at Ludox silica nanoparticles, for which a value $\Gamma_m = 1.8 \mu\text{mol m}^{-2}$ was reported in a recent study [18]. On the other hand, our result for SBA-15 silica is significantly higher than a value reported for lysine in a MCM-41 silica at pH 6 ($\Gamma_m = 0.23 \mu\text{mol m}^{-2}$) [27]. Possible reasons for these differences are discussed in Sect. 5.5.1.

5.4.2 SANS Results

The SANS profile of a slurry sample of pristine SBA-15 in D₂O is shown on a semi-logarithmic scale in Fig. 5.3a. Its main feature is the distinct (10) peak, while the (11) and (20) Bragg reflections appear as a combined peak, due to the limited instrumental resolution. This scattering profile was used to determine parameter b characterizing the effective width of the Gaussian peaks. A mean value $b = 175 \text{ nm}^2$ (for peaks $hk = 10, 11,$ and 20) was obtained as previously [13, 14], and this value was kept constant in the data analysis for all sample loadings. Also shown in Fig. 5.3a is $I(q)$ for a slurry sample of pristine SBA-15 in contrast-matching H₂O/D₂O. In this case no Bragg reflections appear but only a uniform background that results from incoherent scattering from H atoms in the sample.

The SANS profile from a SBA-15 slurry with high surfactant loading (filling factor $f \simeq 0.95$) is shown in Fig. 5.3b. Since this measurement was carried out in contrast-matching $\text{H}_2\text{O}/\text{D}_2\text{O}$, the scattering profile reflects the morphology of surfactant aggregates in the pores. It can be seen that in this sample the combined (11) and (20) peak is larger than the (10) peak. As discussed in Sect. 5.5.2, this is the signature of a cylindrical shell structure that will arise when the surfactant is forming some kind of adsorbed layer at the pore walls. A fit of the experimental scattering curve by a sum of diffuse scattering (Eq. 5.2) and Bragg scattering (Eq. 5.4) terms, and adopting the form factor of a hollow cylinder, $P_{\text{HC}}(q)$, in Eq. 5.4 gives a good fit to the experimental scattering curve. This result is fully consistent with our earlier study of the alkyl ethoxylate surfactants C_{12}E_5 and C_{10}E_5 in the pores of SBA-15 [14].

The effect of added lysine on the morphology of the surfactant aggregates in the pores of SBA-15 was studied by monitoring the SANS profiles at a constant surfactant filling factor $f = 0.95$ (nearly corresponding to the maximum adsorption), but different lysine concentrations. Scattering profiles of samples with lysine amounts corresponding to relative surface concentrations $\theta = 0.1, 0.7, 0.8,$ and 0.9 are shown in Fig. 5.4. The four graphs indicate systematic changes of the scattering behavior with increasing surface concentration of lysine. Whereas at low lysine adsorption ($\theta = 0.1$; Fig. 5.4a) the scattering profile resembles that of the surfactant in the absence of lysine (Fig. 5.3b), but grossly different scattering profiles arise at high lysine surface concentrations. At $\theta = 0.7$ (Fig. 5.4b), the (10) Bragg peak is very pronounced while the (11) and (20) peaks have decreased in magnitude relative to $\theta = 0.1$. Another change in scattering behavior occurs when the surface concentration of lysine is further increased. At $\theta = 0.8$ (Fig. 5.4c) the intensity of all Bragg peaks has decreased relative to $\theta = 0.7$, and at $\theta = 0.9$ (Fig. 5.4d), the Bragg peaks have entirely disappeared. These pronounced changes in the scattering profiles as a function of lysine surface concentration can even be seen in the primary 2D scattering patterns shown as insets in four graphs in Fig. 5.4. The results presented in Fig. 5.4 were obtained with samples in which the silica surface was pre-equilibrated with lysine before adding the surfactant (Sect. 5.3.3). In complementary measurements (not shown) it was found, however, that the scattering profiles do not depend on this pre-equilibration step but only on the chosen surfactant-to-lysine ratio.

For a quantitative analysis we consider the integrated scattering intensities resulting from Bragg scattering (\tilde{I}_{Bragg}) and diffuse scattering (\tilde{I}_{diff}). Integrated intensities of the individual diffraction peaks were determined from the Gaussian functions $S_{hk}(q)$ as [14]

$$\tilde{I}_{\text{Bragg}} = \sum_{hk} \tilde{I}_{hk} \quad (5.6)$$

The integrated diffuse scattering of the samples was determined from the fits with the Teubner-Strey function (Eq. 5.2) as

$$\tilde{I}_{\text{diff}} = \int I_{\text{diff}}(q) q^2 dq \quad (5.7)$$

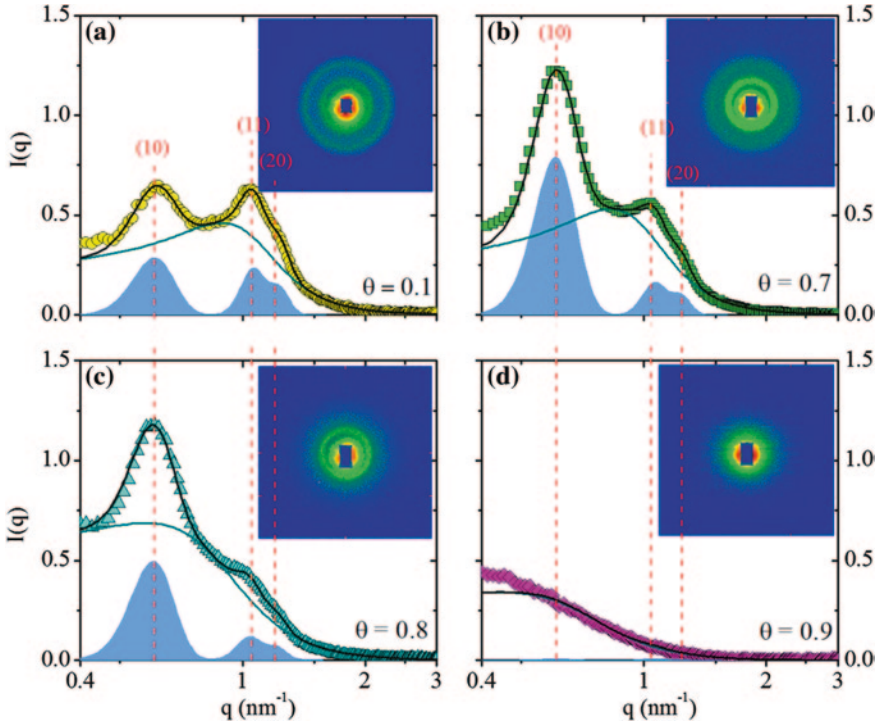


Fig. 5.4 SANS intensity profiles $I(q)$ from SBA-15 slurry samples in contrast-matching $\text{H}_2\text{O}/\text{D}_2\text{O}$ containing a fixed amount of C_{12}E_5 (corresponding to a relative filling $f = 0.95$) but different surface coverage with lysine: **a** $\theta = 0.1$, **b** $\theta = 0.7$, **c** $\theta = 0.8$, and **d** $\theta = 0.9$. The inserts show fits of the primary 2D scattering pattern. Also shown are fits of the 1D scattering profiles (black lines) based on a combination of a diffuse scattering term (green line) and Bragg scattering (contour of blue shaded area). In **d** the data are fitted by the form factor of worm-like micelles without Bragg scattering term

The integrated scattering intensities \tilde{I}_{Bragg} , \tilde{I}_{diff} and total integrated intensity $\tilde{I}_{\text{total}} = \tilde{I}_{\text{Bragg}} + \tilde{I}_{\text{diff}}$ are shown as a function of θ in Fig. 5.5a. In all samples, \tilde{I}_{diff} is the dominating contribution. For the two samples with lysine surface concentration up to $\theta = 0.7$, the two contributions \tilde{I}_{diff} and \tilde{I}_{Bragg} are nearly constant. As the lysine adsorption is increased to $\theta = 0.9$, \tilde{I}_{diff} falls off sharply to a low but finite value, while \tilde{I}_{Bragg} decays to zero.

The behavior of \tilde{I}_{diff} can be rationalized on the basis that the present samples can be regarded approximately as two-phase system consisting of aggregated surfactant and matrix. In this case the diffuse scattering intensity will follow the Porod relation [28] $\tilde{I}_{\text{diff}} \simeq \Phi(1 - \Phi)$, where Φ is the volume fraction of surfactant in the sample. Since the surfactant loading was kept constant for all these samples, \tilde{I}_{diff} should also remain constant if effectively all surfactant is adsorbed in the pores. The fact that \tilde{I}_{diff} falls off steeply at high $\theta > 0.7$ therefore indicates that above some threshold of the lysine surface concentration an increasing

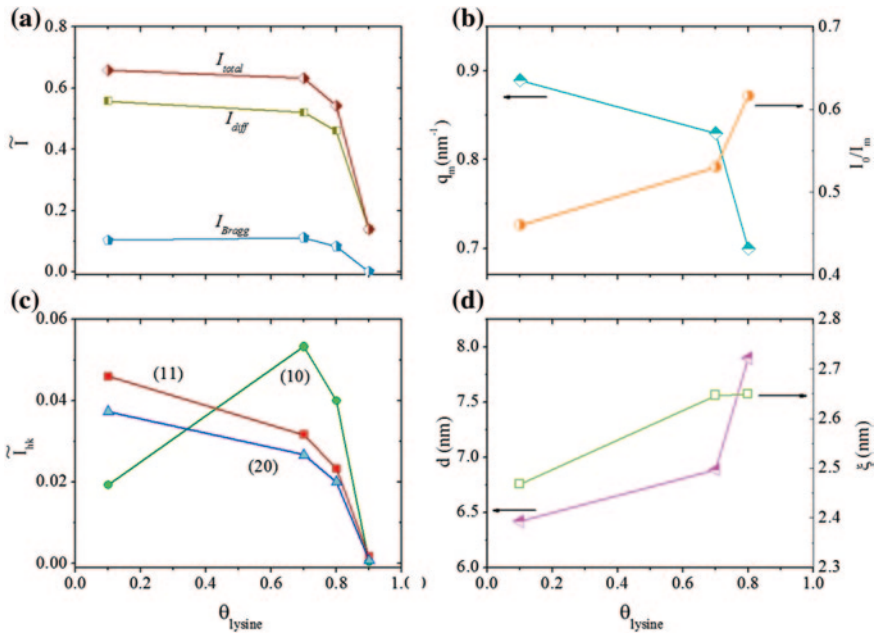


Fig. 5.5 **a** Portion of the intensity contribution coming from diffused (*circles*) and Bragg (*squares*) scattering towards the total experimental scattering intensity. **b** Integrated intensity of individual Bragg’s peaks (10)-*squares*, (11)-*circles* and (20)-*triangles* for SBA-15 in H₂O/D₂O with adsorbed C₁₂E₅ at different lysine amounts. **c** Peak maximum of the diffused scattering contribution and s (I_0/I_m) calculated from Eq. 5.2. **d** Quasiperiodic distance d and order ξ , respectively of the surfactant domain, calculated from Eq. 5.3

fraction of the surfactant was not contained in the silica slurry but remained in the supernatant.

The integral Bragg scattering intensity \tilde{I}_{Bragg} also remains nearly constant from $\theta = 0.1$ to $\theta = 0.7$ (Fig. 5.5a), but this does not apply to the individual contributions \tilde{I}_{hk} , as shown in Fig. 5.5b. Most remarkably, the intensity \tilde{I}_{10} increases by nearly a factor 3 in this range, while the intensities \tilde{I}_{11} and \tilde{I}_{20} decrease. This change in the relative peak intensities, combined with the fact that the amount of surfactant in the pore space has remained constant, can be taken as conclusive evidence of a morphological transition of the surfactant aggregates in the pore space, and the form factor simulations of Fig. 5.1 clearly indicate that at $\theta > 0.7$ the surfactant is no longer forming a shell geometry but some cylindrical geometry. As θ is further increased, the intensity of all Bragg peaks is decreasing and vanishing at $\theta > 0.9$, indicating that no surfactant is left in the pore space.

The diffuse scattering contribution of the samples with lysine surface concentrations up to $\theta = 0.8$ was represented by the Teubner-Strey model. Values of the primary parameters q_m and $s = I_0/I_m$ of Eq. 5.2 are given in Fig. 5.5c, and the characteristic lengths d and ξ derived from these parameters by Eq. 5.3 are shown in Fig. 5.5d. The values at low lysine concentration ($\theta = 0.1$) are similar to those

found previously for this surfactant in the absence of lysine. A weak increase of d and ξ is found as the lysine surface concentration increases up to $\theta = 0.7$. Above this threshold concentration, the quasiperiodic distance d exhibits a marked increase while the decay length ξ remains unchanged.

5.5 Discussion

5.5.1 Lysine Adsorption

Several adsorption studies of lysine onto silica surfaces have aimed to assess the nature of the adsorptive interactions [27, 29]. In aqueous solutions, lysine can exist in different dissociation states. In the pH range 6–9, which is of relevance in the present context, these are the cationic (Lys^+) and zwitterionic (Lys^\pm) form. With increasing pH, silica surface becomes increasingly negatively charged as a result of the dissociation of silanol groups. Since the adsorbed amount of lysine at silica surfaces is strongly increasing with pH it was concluded that electrostatic interactions with the negatively charged silica surface represent the main driving force for the adsorption of lysine. In a recent ATR-IR study [29] it was found that ca. 80 % of the adsorbed lysine was present in the cationic state ($\text{Si-O}^- \dots \text{Lys}^+$) and 20 % in the zwitterionic state ($\text{Si-O}^- \dots \text{Lys}^\pm$). In both cases the adsorptive bond to the surface is formed by the charged terminal amino group, such that the (zwitterionic or anionic) α -aminoacid moiety is exposed to the aqueous medium.

The diversity in values of the limiting adsorption of lysine silica surfaces reported in the literature [18, 27, 29] may be due in part to different pH conditions at which the measurements were performed, as the adsorption is strongly changing with pH. Another cause will be that different silica materials have different surface concentrations of silanol groups and thus a different concentration of binding sites for the aminoacid. In particular we expect that silica nanoparticles prepared and kept in the aqueous medium will have a higher silanol density than silica materials like SBA-15 or MCM-41, which have been calcined at 550 °C. Even for these two materials different concentrations of silanol groups at the surface of the pore walls have been reported, namely 2.9 nm^{-2} for MCM-41 and 3.7 nm^{-2} for SBA-15 [30]. The limiting surface concentration $\Gamma_m = n_m/a_s = 0.75 \text{ } \mu\text{mol m}^{-2}$ for lysine on the present SBA-15 material at pH 7 corresponds to a surface density 0.45 nm^{-2} , implying that at maximum about 1 in 10 silanol groups is binding a lysine molecule.

5.5.2 Lysine Induced Effects

For alkyl ethoxylate surfactants such as C_{12}E_5 it is generally accepted that hydrogen bonding of the silanol groups to oxygen atoms of the ethoxylate head groups represents the dominant binding mechanism of the surfactant to the silica

surface. The hydrogen bond can be formed either directly [31] or mediated with water molecules [32]. We find that lysine is more strongly bound to the silica surface than the surfactant molecules and thus the number of silanol groups available for adsorption of the surfactant will decrease as the surface concentration of lysine increases. Accordingly, the adsorptive binding of the surfactant to the surface will become weaker as the relative surface concentration θ of lysine increases, and this lowering of the adsorption energy eventually leads to the complete displacement of the surfactant from the surface. Such a behavior was recently found for the surfactant $C_{12}E_5$ at silica nanoparticles, where a gradual transition from surface micelles to detached wormlike micelles in the bulk solution was observed as the lysine concentration was increased [18]. The present work shows, however, that in the confined geometry of cylindrical pores the transition from bilayer patches attached to the pore wall ($\theta \leq 0.1$) to wormlike micelles in the extrapore space ($\theta \geq 0.9$) proceeds via an intermediate state (at $\theta \simeq 0.7$). From the intensities of the leading Bragg peaks (Fig. 5.5b) we see that in this intermediate state, the surfactant is no longer forming a cylindrical-shell structure as expected for an adsorbed (patchy) bilayer film, but a cylindrical structure as expected for cylindrical micelles. Simple geometric considerations show that the amount of surfactant in the pore space at the chosen filling factor corresponds to that of a cylindrical aggregate of radius $R_c = R\sqrt{\varphi} = 2.6$ nm, based on the pore radius $R = 4.1$ nm and the mean volume fraction of surfactant in the pore space $\varphi \simeq 0.4$. The resulting value of R_c is similar to that of cylindrical micelles of $C_{12}E_5$. Hence we propose that when the surfactant is gradually displaced from the pore wall by lysine, the intermediate state at $\theta \simeq 0.7$ represents a cylindrical micelle in the pore.

The observed surfactant aggregate morphologies are believed to represent equilibrium structures as they are formed independent of whether the silica sample was in contact first with lysine or with the surfactant. Accordingly, the displacement of surfactant by lysine is to be understood in a thermodynamic sense and not as a unidirectional reaction. Hence, when the silica is pre-equilibrated with lysine at surface concentration corresponding to the intermediate state ($\theta \simeq 0.7$), surfactant is being adsorbed into the pore space to form cylindrical micelles. Since this process is not favored entropically against micelles in the aqueous bulk phase, we conclude that the cylindrical aggregates must still keep in contact with the pore wall in some way. A somewhat similar conclusion emerged from our recent study of the lysine-induced displacement of $C_{12}E_5$ surface micelles from the surface of silica nanoparticles [18], where it was concluded that at intermediate lysine surface concentrations, the weakening of the binding of the surfactant to the surface may involve the formation of a water-rich layer between the surfactant aggregates and the surface. Further work is needed to elucidate this aspect. Regardless of this open point we believe that this is the first example to show that cylindrical surfactant micelles can form spontaneously in cylindrical pores.

As mentioned previously, a wide variety of aggregate morphologies was observed in DPD molecular simulations of a short-chain surfactant/water system confined to a nanotube [33]. Specifically, for model hydrophilic surfaces (when water was preferred by the pore wall) and surfactant concentrations comparable to those in the

present work, formation of threadlike micelles was observed in the central region of the nanopores. This aggregate morphology is consistent with the proposed aggregate structure at intermediate lysine concentrations of the present work.

5.6 Conclusion

The self-assembly of the surfactant of C₁₂E₅ in the cylindrical nanopores of SBA-15 silica has been tuned by co-adsorption of the basic aminoacid lysine. The adsorption behavior of lysine at SBA-15 was characterized by its single-component adsorption isotherm while the adsorption isotherm of C₁₂E₅ was taken from the earlier study. The aggregate morphologies of the surfactant in the pores in the absence and presence of lysine was then studied by SANS in contrast-matching H₂O/D₂O water. The SANS data were analysed along the lines described in our preceding studies [13, 14]. The main findings of this work are:

1. At low lysine adsorption levels the surfactant is forming patchy bilayer aggregates at the pore walls, as observed in the absence of lysine.
2. At high lysine adsorption levels, i.e. values approaching the limiting surface concentration ($0.75 \mu\text{mol m}^{-2}$), the surfactant is completely displaced from the pore space and forms cylindrical micelles in the extrapore bulk liquid.
3. At an intermediate lysine adsorption level (ca. 70 % of the maximum surface concentration) the surfactant is forming cylindrical micelles inside the tubular pores. Our conclusions rely on a quantitative analysis of the intensities of the Bragg reflections from the pore lattice peaks as a function of the lysine adsorption level. To our knowledge this is the first time that the formation of cylindrical surfactant aggregates by adsorption into the cylindrical nanopores has been verified experimentally. The driving force for this process is, however, not yet clear. We propose that the cylindrical micelles in the pores are stabilized by weak interactions with the surface, either by direct contact of surfactant head groups with the surface silanol groups at a few places along the pore, or mediated by lysine and a hydration shell of water at the pore wall.

References

1. Davis ME (2002) Ordered porous materials for emerging applications. *Nature* 417:813
2. Slowing II, Trewyn BG, Giri S, Lin S-Y (2007) Mesoporous silica nanoparticles for drug delivery and biosensing applications. *Adv Funct Mater* 17:1225
3. Scamehorn JF, Harwell JH (1989) Surfactant-based separation processes, vol 33. New York, USA
4. Ruiz-Angel MJS, Carda-Broch S, Torres-Lapasio JR, Garcia-Alvarez-Coque MC (2009) Retention mechanisms in micellar liquid chromatography. *J Chromatogr A* 1216:1798
5. Brumar C, Geng ML (2010) Interaction of surfactants with hydrophobic surfaces in nanopores. *Langmuir* 26:19091

6. Levitz P (1991) Aggregative adsorption of nonionic surfactants onto hydrophilic solid/water interface. Relation with bulk micellization. *Langmuir* 7:1595
7. Grant LM, Tiberg F, Ducker WA (1998) Nanometer-scale organization of ethylene oxide surfactants on graphite, hydrophilic silica, and hydrophobic silica. *J Phys Chem B* 102:4288
8. Tyrode L, Rutland MW, Bain CD (2008) Adsorption of CTAB on hydrophilic silica studied by linear and nonlinear optical spectroscopy. *J Am Chem Soc* 130:17434
9. Dietsch O, Eltekov A, Bock H, Gubbins KE, Findenegg GH (2007) Crossover from normal to inverse temperature dependence in the adsorption of nonionic surfactants at hydrophilic surfaces and pore walls. *J Phys Chem C* 111:16045
10. Perret E, Nygård K, Satapathy DK, Balmer TE, Bunk O, Heuberger M, van der Veen J (2010) Molecular liquid under nanometer confinement: density profiles underlying oscillatory forces. *J Phys: Conds Matter* 22:235102
11. Nygård K, Satapathy DK, Perret E, Padeste C, Bunk O, David C, van der Veen JF (2010) Surface-specific ordering of reverse micelles in confinement. *Soft Matter* 6:4536
12. Qiao Y, Schönhoff M, Findenegg GH (2003) ²H NMR investigation of the structure and dynamics of the nonionic surfactant C₁₂E₅ confined in controlled pore glass. *Langmuir* 19:6160
13. Müter D, Shin T, Demé B, Fratzl P, Paris O, Findenegg GH (2010) Surfactant self-assembly in cylindrical silica nanopores. *J Phys Chem Lett* 1:1442
14. Shin T, Müter D, Meissner J, Paris O, Findenegg GH (2011) Structural characterization of surfactant aggregates adsorbed in cylindrical silica nanopores. *Langmuir* 27:5252
15. Zhao DY, Feng JL, Huo QS, Melosh N, Fredrickson GH, Chmelka BF, Stucky GD (1998) Triblock copolymer syntheses of mesoporous silica with periodic 50 to 300 angstrom pores. *Science* 279:548
16. Jähnert S, Müter D, Prass J, Zickler GA, Paris O, Findenegg GH (2010) Pore structure and fluid sorption in ordered mesoporous silica. I. Experimental study by in situ small-angle X-ray scattering. *J Phys Chem C* 113:15201
17. Findenegg GH, Jähnert S, Müter D, Prass J, Paris O (2010) Fluid adsorption in ordered mesoporous solids determined by in situ small-angle X-ray scattering. *Phys Chem Phys* 12:7211
18. Bharti B, Meissner J, Gasser U, Findenegg GH (2012) Surfactant adsorption and aggregate structure at silica nanoparticles: effects of particle size and surface modification. *Soft Matter* 8:2573
19. Lugo D, Oberdisse J, Karg M, Schweins R, Findenegg GH (2009) Surface aggregate structure of nonionic surfactants on silica nanoparticles. *Soft Matter* 5:2928
20. Teubner M, Strey R (1987) Origin of the scattering peak in microemulsions. *J Chem Phys* 87:3195
21. Kholodenko AL (1993) Analytical calculation of the scattering function for polymers of arbitrary flexibility using the Dirac propagator. *Macromolecules* 26:4179
22. Akcakayiran D, Mauder D, Hess C, Sievers TK, Kurth DG, Shenderovich I, Limbach H-H, Findenegg GH (2008) Carboxylic acid-doped SBA-15 silica as a host for metallo-supramolecular coordination polymers. *J Phys Chem B* 112:14637
23. Bharti B, Meissner J, Findenegg GH (2011) Aggregation of silica nanoparticles directed by adsorption of lysozyme. *Langmuir* 27:9823
24. Jaroniec M, Solovyov LA (2006) Improvement of the Kruk-Jaroniec-Sayari method for pore size analysis of ordered silicas with cylindrical mesopores. *Langmuir* 22:6757
25. <http://www.ill.eu/html/instruments-support/computing-for-science/cs-software/all-software/lamp/>
26. Consortium Scilab–Digiteo (2011) Scilab: free and open source software for numerical computation (Windows, Version 5.3.3). Available from: <http://www.scilab.org>
27. O'Connor AJ, Hokura A, Kisler JM, Shimazu S, Stevens GW, Komatsu Y (2006) Amino acid adsorption onto mesoporous silica molecular sieves. *Sep Purif Technol* 48:197
28. Porod G (1967) Small-angle scattering of X-rays, Gordon & Breach, New York, London, Paris

29. Kitadai N, Yokoyama T, Nakashima S (2009) ATR-IR spectroscopic study of L-lysine adsorption on amorphous silica. *J Colloid Interface Sci* 329:31
30. Shenderovich IG, Mauder D, Akcakayiran D, Buntkowsky G, Limbach H-H, Findenegg GH (2007) NMR provides checklist of generic properties for atomic-scale models of periodic mesoporous silicas. *J Phys Chem B* 111:12088
31. Trens P, Denoyel R (1993) Conformation of poly (ethylene glycol) polymers at the silica/water interface: a microcalorimetric study. *Langmuir* 9:519
32. Matsson MK, Kronberg B, Claesson PM (2004) Adsorption of alkyl polyglucosides on the solid/water interface: equilibrium effects of alkyl chain length and head group polymerization. *Langmuir* 20:4051
33. Arai N, Yasuoka K, Zeng XC (2008) Self-assembly of surfactants and polymorphic transition in nanotubes. *J Am Chem Soc* 130:7916

Part III

Adsorptive and Aggregative Effects of Proteins on Silica Nanoparticles

Part III of the thesis presents the studies of the interactions between silica nanoparticles (20 nm) with two globular proteins, cytochrome C and lysozyme. Chapter 6 deals with the effects of pH on the adsorption of lysozyme to silica nanoparticles and the protein-induced aggregation of the silica particles. In direct continuation to these studies, Chap. 7 focuses on the effect of ionic strength on the adsorption and the concomitant aggregation of the protein/silica system. Chapter 8 highlights the differences in the aggregation-induced behavior observed for lysozyme and cytochrome C with silica.

Chapter 6

Aggregation of Silica Nanoparticles Directed by Adsorption of Lysozyme

6.1 Introduction

Interaction of biomolecules with nanoscale materials has attracted much attention in recent years, triggered by promising new developments in pharmaceutical and biomedical technology. Nanoparticles are used as carriers in biomolecular transport and drug delivery, regenerative medicine, biosensing, imaging and related applications [1–4]. Immobilization of proteins on nanoscale materials is usually based on adsorption [5–8], entrapment [9–11], or covalent binding [12, 13]. Adsorption from aqueous media onto hydrophilic surfaces can in many cases be controlled by pH and ionic strength and in this way allows controlled binding and release of the protein molecules. Fundamentals of the adsorption equilibrium and kinetics of proteins have been studied at well-defined flat model surfaces, using surface-sensitive spectroscopic techniques [14, 15], ellipsometry or optical reflectometry [16, 17], and neutron reflectometry [18]. Adsorption onto nanoscale surfaces introduces a higher level of complexity, as their high surface curvature can influence the adsorption as well as the structure and biological activity of the protein [5, 6, 19–22]. On the other hand, the growing importance of nanosize particles in everyday life makes studies of their interaction with biomolecules a matter of high importance [23–25].

Aqueous dispersions of oxide nanoparticles containing globular proteins also represent interesting model systems for studying fundamentals of colloidal interaction. Globular proteins such as lysozyme exhibit the major characteristics of colloids that interact via a short-range attractive potential superimposed with repulsive electrostatic interactions [26]. Under certain conditions the short-range attraction may cause the formation of small clusters which are stabilized against further growth by electrostatic repulsion. However, the physical nature of these protein clusters is still not fully understood and remains an active field of current research [27–30]. Oxide particles such as silica are prototypical for colloid systems interacting by van der Waals

Reprinted with permission from Bharti, B., Meissner, J., Findenegg, G. H., *Langmuir*, 2011, 27, 9823. Copyright 2011 American Chemical Society.

and electrical double layer forces. Ionic strength and pH are affecting the aggregation of these particles in a way predicted by the Derjaguin–Landau–Verwey–Overbeek (DLVO) theory [31, 32]. The adsorption of globular proteins onto colloidal oxide particles is attributed to electrostatics, dispersion forces and solvation forces. Electrostatic interaction will promote protein adsorption in the pH range between the isoelectric point (IEP) of protein and of the surface, and impede adsorption outside this pH range, where the net charge of the protein is equal to that of the particles [17]. Accordingly, pH will have a pronounced effect on the strength of adsorption of the protein at the particle surface. Many studies have been devoted to the adsorption of proteins on nanoparticles and the effect of adsorption on the protein structure and activity [5, 6, 19–22]. On the other hand, rather little is known about how protein adsorption is affecting the interaction of the nanoparticles. Recently, Kendall et al. [23] studied the aggregation behavior of nanoparticles induced by fibrinogen, in order to assess the toxicity of the particles in relation to the proteins. In a different context, Ang et al. [33] studied the interaction of silica nanoparticles with β -casein at air-water interface and its effect on the surface activity of the silica-protein complexes. Bridging attraction and hetero-aggregation of silica nanoparticles was also found under the influence of adsorbed polyethylene oxide [34] and of thermo-responsive polymer chains [35]. This kind of behavior contrasts with the more familiar situation in which aggregation is prevented by grafting of an organic layer onto the surface of the particles [36, 37].

Here we study the adsorption of a globular protein on silica nanoparticles and the protein-induced interaction between the nanoparticles from a colloid science point of view. Lysozyme (molecular mass 14.3 kDa, isoelectric point near pH 11) was chosen as the protein because of its high structural stability which makes it a good model for “hard” proteins. The molecules are of roughly prolate shape and have a radius of gyration of 1.64 nm [38]. The silica nanoparticles used in this study were synthesized by a variant of the classical Stöber method, using lysine instead of ammonia as the catalyst. This allows to prepare samples of low polydispersity for particle sizes near 20 nm, and the particles have lower chemical reactivity and better biocompatibility than Ludox particles [25]. We determined the adsorption isotherm of lysozyme on these particles over a wide pH range, and studied the effect of lysozyme adsorption on the aggregation of the silica particles as a function of pH. A combination of analytical centrifugation, cryo-TEM and small-angle X-ray scattering was used to characterize the properties and structure of the hetero-aggregate over the pH range from the IEP of the silica to the IEP of lysozyme.

6.2 Results

6.2.1 Characterization of Silica Nanoparticles

Silica nanoparticles were characterized by SAXS and nitrogen adsorption. SAXS was used for estimating the mean particle size and size distribution in the dispersion. Figure 6.1 shows the scattering profile of 1 wt% silica dispersion at pH 9.

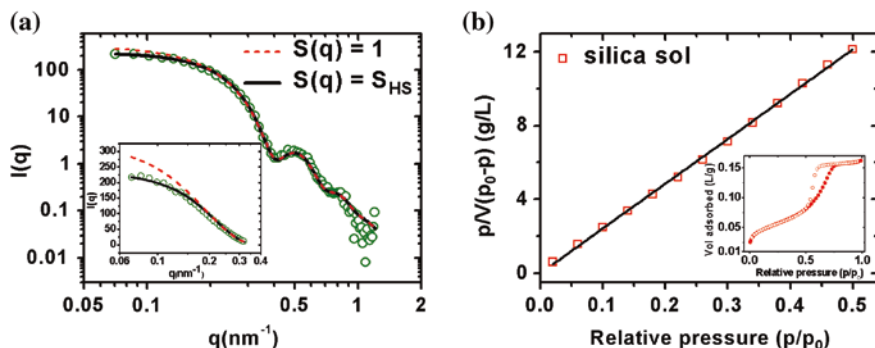


Fig. 6.1 Characterization of silica particles: **a** SAXS intensity $I(q)$ of 1 wt% dispersion (circles) and fits of the data with the form factor of polydisperse spheres (full curve) and with consideration of a hard-sphere structure factor S_{HS} (dashed); the low- q region is also shown on a linear scale (inset); **b** BET plot of the nitrogen adsorption isotherms on the dry silica; the full adsorption isotherm is shown in the inset

Table 6.1 Characterization of silica particles by SAXS and nitrogen adsorption

| SAXS | | | Nitrogen adsorption | | |
|---------------------|-------|-----------|-------------------------------|-----------|-------------------|
| $\langle D \rangle$ | s | φ | a_{BET} (m ² /g) | C_{BET} | a_{BET}/a_{geo} |
| 6.5 | 0.115 | 0.0050 | 293 | 116.5 | 1.45 |

Mean particle diameter $\langle D \rangle$, polydispersity s , particle volume fraction φ , specific surface area a_{BET} and adsorption constant C_{BET} based on the BET model, and geometric surface area a_{geo} derived from the mean particle

The form factor of spheres with polydispersity $s = 0.115$ gives a good fit of the data at $q > 0.2 \text{ nm}^{-1}$. The negative deviations from this function occurring at lower q , shown on linear scale in the inset of Fig. 6.1a, which can be accounted for, by a hard-sphere structure factor (see Sect. 3.1). Fit parameters are given in Table 6.1. The appearance of a structure factor can be attributed to electrostatic repulsion between the particles caused by their negative excess charge. The specific surface area of the silica was determined by nitrogen adsorption on the basis of the BET model (see Fig. 6.1b; Table 6.1). The resulting value a_{BET} was compared with the geometric surface area a_{geom} of silica particles of diameter $\langle D \rangle$ as derived from SAXS, based on a silica density $\rho = 2.2 \text{ g cm}^{-3}$. This yields a ratio of the two areas $a_{BET}/a_{geom} = 1.45$. This is a typical value for silica nanoparticles in this size range and can be attributed to surface roughness [39].

6.2.2 Lysozyme Adsorption

The adsorption of lysozyme on the silica nanoparticles was studied over a wide pH range. Adsorption isotherms at pH values from 5 to 9 are shown in Fig. 6.2, where adsorption is expressed by Γ , the mass of protein per unit area of silica (based on

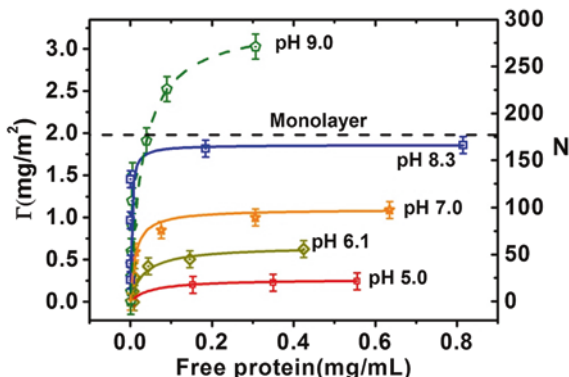


Fig. 6.2 Adsorption isotherms of lysozyme on the silica nanoparticles, expressed as protein mass per unit area (Γ) and as mean number of protein molecules per silica particle (N), at different pH values: experimental data (*symbols*) and fits by the Langmuir model (*lines*). The monolayer capacity based on a cross-sectional area $A_0 = 12 \text{ nm}^2$ is indicated by the *dashed line*

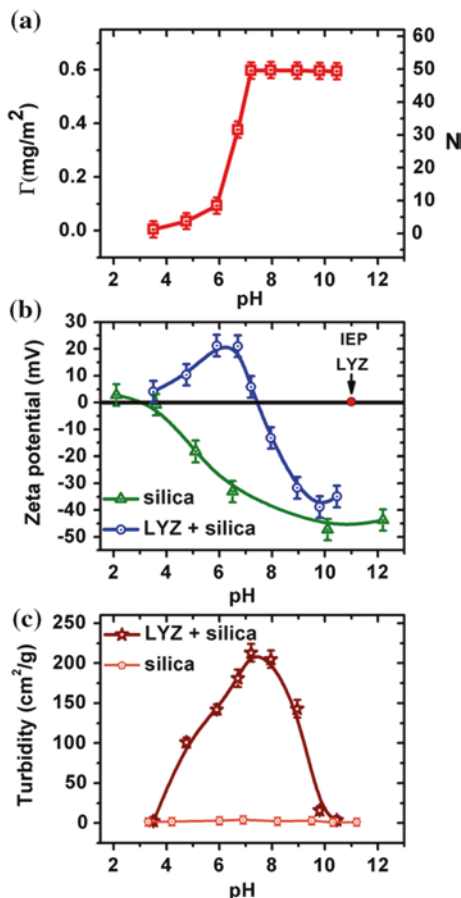
Table 6.2 Langmuir parameters for lysozyme on silica

| pH | K_H (10^{-6} m) | Γ_m (mg/m^2) | A_m (nm^{-2}) | N_m |
|-----|-------------------------------|--------------------------------|----------------------------|-------|
| 5.0 | 5 | 0.27 | 88 | 24 |
| 6.1 | 20 | 0.66 | 36 | 59 |
| 7.0 | 91 | 1.10 | 22 | 96 |
| 8.3 | 740 | 1.86 | 13 | 162 |
| 9.0 | – | >3.0 | <8 | >260 |

K adsorption equilibrium constant; Γ_m maximum adsorption (protein mass per unit area); A_m nominal area per adsorbed protein molecule; N_m number of adsorbed protein molecules per silica particle

a_{BET}), and by N , the mean number of protein molecules per silica particle (based on the particle size from SAXS and $a_{\text{BET}}/a_{\text{geom}}$). From the cross-sectional area of lysozyme molecules adsorbed side-on ($A_0 \approx 4 \text{ nm} \times 3 \text{ nm} = 12 \text{ nm}^2$) we expect a maximal adsorbed amount of 2.0 mg/m^2 in a monolayer. This estimated monolayer capacity of the protein is indicated by the dashed line in Fig. 6.2. It can be seen that this level is nearly reached in the plateau region of the isotherm at pH 8.3. The adsorption data for pH up to 8.3 can be represented by the Langmuir equation, $\Gamma = \Gamma_m bc / (1 + bc)$. Here, c is the equilibrium concentration of free protein in solution, Γ_m is the plateau value of the surface concentration, and the parameter b is related to the thermodynamic equilibrium constant of the protein-surface interaction (Henry's law constant), $K_H = (\Gamma/c)_{c \rightarrow 0}$, as $K_H = b\Gamma_m$. Best-fit values of K_H and Γ_m are given in Table 6.2. Both parameters are progressively increasing with pH. The adsorption isotherm at pH 9 exhibits a very steep initial increase up to $\Gamma \approx 1.5 \text{ mg/m}^2$, as at pH 8.3, but a further increase to values well beyond a dense monolayer is observed at higher protein concentrations. This indicates the formation of a second layer of protein molecules on top of the first layer at pH 9. From our experimental data we cannot decide if the adsorption at this pH reaches a limiting value at higher concentrations, as it is found for lower pH.

Fig. 6.3 Results of pH titration experiments for a 1 wt% dispersion with fixed overall amount of lysozyme, corresponding to $N = 50$ protein molecules per silica particle: **a** adsorbed amount expressed as protein mass per unit area (Γ) and number of lysozyme molecules adsorbed per silica (N); **b** zeta potential of the silica particles in the absence (*triangles*) and in the presence of lysozyme (*circles*); **c** turbidity of the dispersion in the absence (*squares*) and in the presence of lysozyme (*stars*). The curves in the three graphs are drawn as a guide to the eye



A correlation of the adsorption data for pH 9 on the basis of the Langmuir equation yields $\Gamma_m = 3.05 \text{ mg/m}^2$. Table 6.2 also gives values of the mean area per protein molecule at maximum adsorption, $A_m = M/N_A\Gamma_m$ (where M is the molar mass and N_A the Avogadro constant), and the maximum number of protein molecules per silica particle, $N_m = A_p/A_m$ (where $A_p = \pi D^2 a_{\text{BET}}/a_{\text{geo}}$ is the surface area per silica particle based on the mean particle diameter and surface area ratio from Table 6.1).

6.2.3 pH Effects at a Constant Protein-to-Silica Ratio

The effect of pH on the protein binding and excess charge of the silica particles, and on the protein-induced aggregation of the silica particles in the dispersion, was studied by measuring the amount of bound protein, the zeta potential and the turbidity as a function of pH for a dispersion containing fixed amount of silica and protein. Results for 1 wt% silica dispersion with 1.1 mg/mL lysozyme are shown in Fig. 6.3.

The chosen amount of protein corresponds to a surface concentration of 0.60 mg/m^2 (ca. 50 lysozyme molecules per silica particle). The pronounced increase of the protein binding capacity of the silica particles at $\text{pH} > 4$ is demonstrated in Fig. 6.3a. The plateau of Γ reached near $\text{pH} 7$ is a manifestation of the fact that the solution has become depleted of protein, i.e., the fraction of bound protein is close to 1 at $\text{pH} > 7$. Note that this limiting value ($\Gamma \simeq 0.60 \text{ mg/m}^2$) is lower than the plateau value of the adsorption isotherms (Γ_m) at $\text{pH} > 7$ (Table 6.2), and less than one third of the estimated monolayer capacity of the protein on the silica surface (ca. 2 mg/m^2 ; see Fig. 6.2). pH titration experiments performed with higher overall amounts of protein in the system yield higher plateau values of Γ which are reached at somewhat higher pH than in Fig. 6.3a.

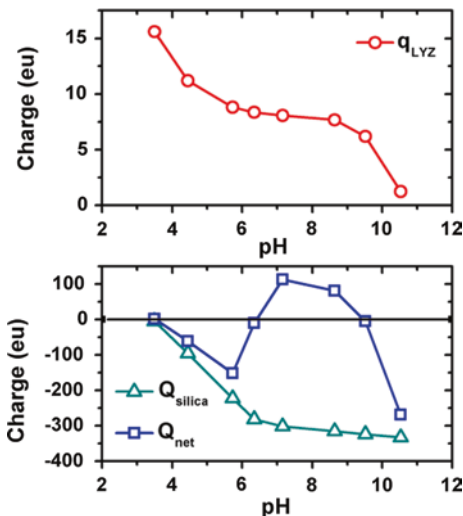
Results for the zeta potential of silica particles in the absence and presence of protein are shown in Fig. 6.3b. The bare silica particles have their IEP at $\text{pH} \simeq 3.0$, i.e. higher than values between $\text{pH} 1.2$ and 2.5 reported in the Refs. [37, 40, 41]. Presumably this difference is due to chemisorbed lysine used during the synthesis of silica nanoparticles. In the presence of the protein, the zeta potential of the silica particles at low pH is similar to that of the plain particles, as to be expected from the fact that almost no adsorption of the protein takes place below $\text{pH} 4$. In the pH range in which binding of the protein occurs the zeta potential increases to values up to $+20 \text{ mV}$ at $\text{pH} 6\text{--}7$, indicating that the adsorption of positively charged protein is outweighing the increase in negative charge of silica particles. At $\text{pH} > 7$ all protein is bound. The pronounced decrease of the zeta potential in this regime is attributed to the decrease in net charge of the adsorbed protein molecules. Finally, when the IEP of the protein is reached, the zeta potential of the silica with adsorbed protein becomes similar to that of the plain particles (ca. -45 mV).

In order to see how the observed pH dependence of the zeta potential is reflecting the net charge of the composite particles, we have estimated the net charge of the silica particles and the protein. The net charge of the bare silica particles as a function of pH was estimated from the electrophoretic mobility μ_e on the basis of the Hückel equation $Q_{\text{silica}} = 6\pi\eta R\mu_e$, which is applicable when $\kappa R < 1$, where κ denotes the inverse Debye length [42]. This condition was met in the absence of the protein. The ionic strength in the presence of lysozyme was estimated to reach 2 mM (mostly due to the salt contents of the lysozyme sample), corresponding to $1/\kappa = 6.8 \text{ nm}$ ($\kappa R = 1.6$), and thus the Hückel equation is strictly not applicable. The net charge on lysozyme molecules as a function of pH was calculated using the expression [43]

$$q_{\text{lyz}} = \sum_{iA} n_{iA} \left(1 + 10^{-(\text{pH} - \text{pK}_{a_{iA}})}\right)^{-1} + \sum_{iB} n_{iB} \left(1 + 10^{-(\text{pH} - \text{pK}_{a_{iB}})}\right)^{-1} \quad (6.1)$$

here, n_{iA} and n_{iB} represent the numbers of acidic and basic amino acids of type i in the molecule, $\text{pK}_{a_{iA}}$ and $\text{pK}_{a_{iB}}$ denote their respective acidity constants, and the summations extend over all types of acidic and basic amino acids of the molecule. According to this relation, the net charge q_{lyz} of lysozyme molecules is about $+8$

Fig. 6.4 pH dependence of the net charge as a function of pH: lysozyme molecule (q_{LYZ}) according to Eq. 6.2 (*upper graph*); bare silica particles (Q_{silica} , triangles) and algebraic sum of bare silica plus N adsorbed lysozyme molecules according to Eq. 6.2 (Q_{net} , squares) (*lower graph*)



at pH 7 and becomes zero at pH 10 (see Fig. 6.4). The effective net charge of silica particles with adsorbed protein depends on the number of adsorbed protein molecules, N , and on the net charge of the protein molecules. In the absence of charge regulation effects it will be given by

$$Q_{\text{net}}(N) = Q_{\text{silica}} + Nq_{\text{lyz}} \quad (6.2)$$

where Q_{silica} , q_{lyz} , and N all vary with pH. Results for the pH dependence of q_{lyz} , Q_{silica} , and $Q_{\text{net}}(N)$ for the 1 wt% silica dispersion with 1.1 mg/mL lysozyme are shown in Fig. 6.4. It can be seen that $Q_{\text{net}}(N)$ reproduces the transition from positive to negative net charge as observed for the zeta potential at pH > 7 (Fig. 6.3b), indicating that this behavior can be attributed to the increasingly negative charge of the bare silica particle, while N remains constant and q_{lyz} decreases. At lower pH, $Q_{\text{net}}(N)$ underestimates the increasing charge of the adsorbed protein, which in this regime is dominated by the increase of N with pH. Hence the model based on an algebraic sum of the charges (6.2) oversimplifies the situation of the particles with adsorbed protein but may be seen as a starting point for a more quantitative modeling of the complex behavior. The observed crossover from positive to increasingly negative values of the zeta potential for pH titrations of silica nanoparticles in the presence of lysozyme is in qualitative agreement with the work of Rezwani et al. [40] who also found that the associated IEP of the particles shifts in the direction of the IEP of the protein when the protein concentration in the system is increased. Our observation of a maximum in the zeta potential versus pH is in line with a similar behaviour observed for composite particles of β -casein with lysozyme by Pan et al. [44].

The influence of pH on the turbidity of the dispersion is shown in Fig. 6.3c. At pH ≤ 4 where protein is not adsorbed, the dispersion has a low turbidity. In the regime of increasing protein binding by the silica particles ($4 < \text{pH} < 7$) the

turbidity increases steeply and remains high up to pH 9. Since the turbidity of the silica dispersion without protein is low in this pH regime, this behaviour indicates that lysozyme is causing flocculation of the silica. However, when pH is approaching IEP of lysozyme the turbidity sharply decreases, indicating a decreasing floc size and possibly re-dispersion of the silica. Since the protein remains strongly adsorbed at the silica particles, this de-flocculation must be a consequence of charge stabilization as the net charge of the silica particles is now becoming strongly negative (Fig. 6.3c).

6.2.4 Characterization by Analytical Centrifuge

Analytical centrifugation was used to characterize the properties of the hetero-flocculate as a function of pH for the same protein-to-silica ratio as in Sect. 6.2.3. At the onset of protein binding to the silica particles (pH 4.2) a low turbidity and no significant change of the transmission profile with time was detected, indicating that only small aggregates exist. At a somewhat higher pH (5.5) but still in the low protein binding regime (Fig. 6.3a), an initial polydisperse sedimentation is observed in which the particles settle with different velocities according to differences in floc size. Whereas initially small flocs have enough room to settle individually, later they combine to a flocculated network as at higher pH. In the complete protein-binding regime (pH 7–9) the samples exhibit the typical zone sedimentation behavior of flocculated networks. However, as pH is further increased to pH 10, the behavior changes sharply to a polydisperse sedimentation. The sedimentation and compression kinetics of the samples as a function of pH is shown in Fig. 6.5. The initial sedimentation velocity measured at 36 g (Fig. 6.5-left) increases from pH 5.5 to 8.7 but the sediment volume at pH 5.5 is significantly smaller than at pH 7–9. The sedimentation velocity at pH 10.2 is much smaller than for the other samples at 36 g. However, at a higher acceleration (2,300 g) the sample at pH 10.2 reaches a sediment volume almost as low as at pH 5.5, indicating a denser floc structure than at intermediate pH. Values of the sedimentation velocity at 36 g and of the floc volumes before and after compression at 2,300 g are summarized in Table 6.3. The volume-weighted size distribution of the protein/silica flocs was derived by analysing the time evolution of the transmission at fixed heights and then averaging. The resulting particle size represents the equivalent diameter according to the hydrodynamic diameter of rigid-sphere particles. Results are shown in Fig. 6.6. Samples in the pH range 5.5–8.7 exhibit a bimodal size distribution, with a fine fraction of 500–700 nm and a coarse fraction of 3–4 μm diameter. With increasing pH the fraction of larger aggregates increases, and at pH 8.7 the fraction of the smaller aggregates amounts to less than 5 %. However, when pH is increased to 10.2 a monomodal distribution of aggregates in a size range from 100 to 300 nm is found, indicating that the larger aggregates have split up into much smaller aggregates.

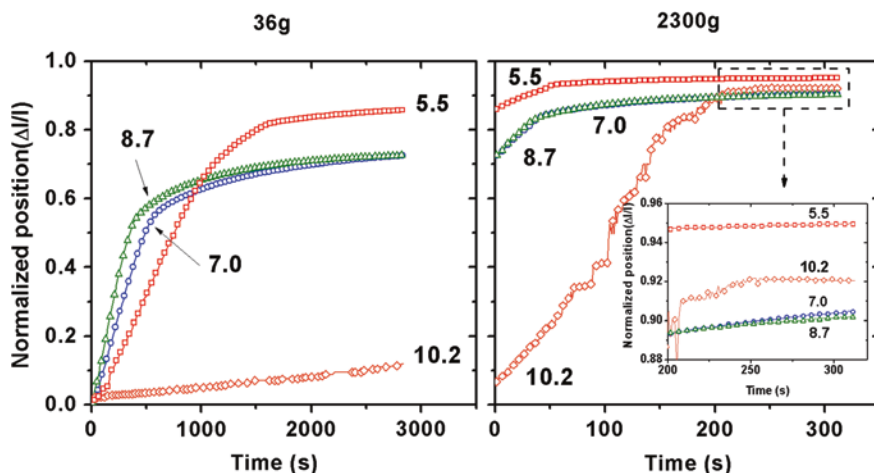


Fig. 6.5 Sedimentation kinetics of the silica/lysozyme hetero-flocculate at different pH values (20 °C) expressed by the normalized position ($\Delta l/l$) of the flocculate/supernatant boundary (traced at a limiting transmission value of 75 %) at constant centrifugal acceleration 36 g (*left*) and 2,300 g (*right*); the *inset* shows the results for times >200 s at 2,300 g on an expanded scale

Table 6.3 Sedimentation velocity, sediment volume and equivalent aggregate size of silica/protein flocculate

| pH | c_s ($\mu\text{m s}^{-1}$) | V_s (mm^3) | V_c (mm^3) | D_{equiv} (μm) |
|------|--------------------------------|-------------------------|-------------------------|--------------------------------------|
| 5.5 | 13.9 | 63 | 24 | 0.7 ± 0.6 |
| 7.0 | 26.6 | 121 | 43 | 1.9 ± 0.5 |
| 8.7 | 37.6 | 121 | 44 | 2.8 ± 2.2 |
| 10.3 | 0.81 | – | 36 | 0.17 ± 0.1 |

c_s sedimentation velocity (36 g); V_s sediment volume (after 3,000 s at 36 g); V_c compressed sediment volume (after 300 s at 2,300 g); D_{equiv} volume-weighted median particle size of silica/protein

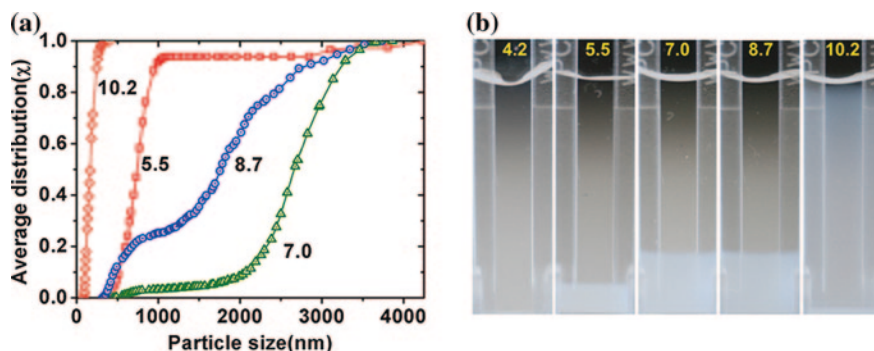


Fig. 6.6 **a** Cumulative volume-weighted distribution (χ) of floc sizes of the silica/lysozyme aggregates at different values of pH; **b** sample cells showing the floc volume appearance of the samples after 2,800 s at centrifugal acceleration 36 g

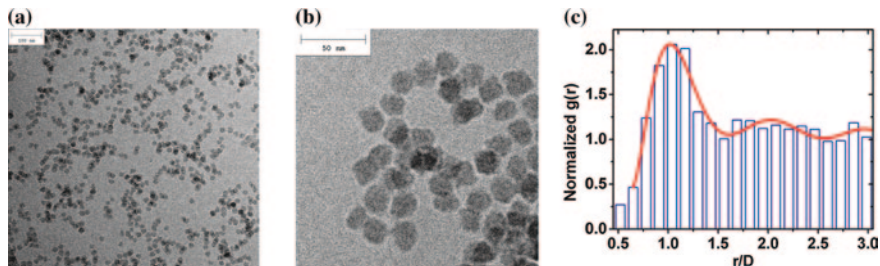


Fig. 6.7 Cryo-TEM images of silica/lysozyme flocs at pH 8.3 at different magnifications: **a** scale bar 100 nm; **b** scale bar 50 nm; **c** pair correlation function $g(r)$ derived from cryo-TEM image

6.2.5 Cryo-TEM Study of Flocculation

Solution cryo-TEM was used to directly image the structure of the silica flocs formed in the presence of lysozyme. Micrographs for a silica dispersion containing 0.46 mg/mL lysozyme ($\Gamma = 0.25 \text{ mg/m}^2$) at pH 8.3 are shown in Fig. 6.7. Micrographs at higher magnification, as in Fig. 6.7b, indicate the presence of gaps between the silica particles. The gap width (surface-to-surface distance) is typically $2.5 \pm 1 \text{ nm}$, consistent with the cross-sectional dimension of the lysozyme molecules. This suggests that lysozyme molecules are bridging the silica particles by adsorption to both surfaces. However, this is no conclusive evidence, since the protein molecules are not directly visible in the cryo-TEM graphs. Repulsive electrostatic interaction between the silica particles, or artifacts from edge effects, cannot be ruled out a priori as possible reasons for the observed gaps.

The cryo-TEM images were analyzed quantitatively to determine the pair correlation function $g(r)$ for silica particles. Pair correlations $g(r)$ between the silica particles were extracted for complete analysis of cryo-TEM image. All coordinates of the individual particle in the image were extracted using the software *Image J*.

A *Scilab* code was prepared for calculating all the possible distances between each pair of particles. $g(r)$ was determined using the relation

$$g(r) = \frac{\delta N}{2\pi N \delta r} \quad (6.3)$$

where r is distance between silica particle, δr is the increment in r , δN is the number of particles in the distance range δr . Initially, all the distances were in the units of pixels. Normalized distances r/D were obtained by dividing the distances with average silica diameter (in pixels). A typical example is shown in Fig. 6.7c. A good fit of the correlation plot for $g(r)$ was obtained by a polynomial of 9°. The function shows a distinct maximum at a pair distance equal to the diameter of the particle ($r/D = 1$) and a further weak maximum at a pair distance $r/D = 2$, indicating some tendency for the formation of linear chains. However, from the present results we cannot rule out that the secondary maximum is an artifact of the cryo-TEM procedure and image analysis.

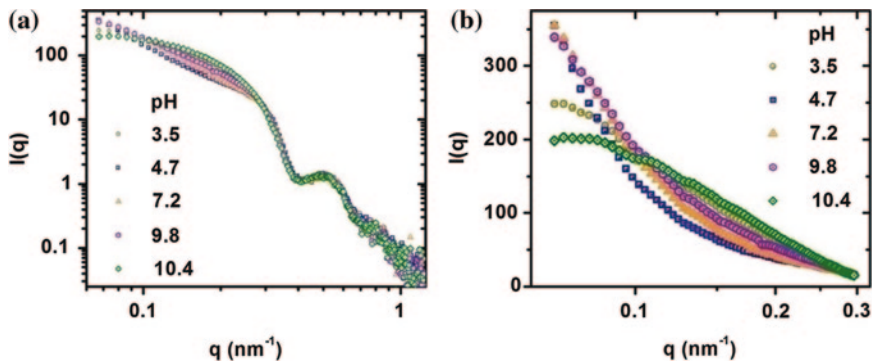


Fig. 6.8 SAXS intensity profiles $I(q)$ for a silica/lysozyme samples at different pH values indicated in the graphs: **a** logarithmic scale; **b** low- q region of scattering profiles on a linear intensity scale

6.2.6 SAXS Study of Flocculate

SAXS was used to study the structure of the silica-protein aggregates in the aqueous medium free of artifacts inherent in the sample preparation for cryo-TEM. Scattering intensity profiles $I(q)$ for a 1 wt% silica dispersion containing 1.1 mg/mL of lysozyme at different pH values are shown in Fig. 6.8. In the large- q region ($q > 0.5 \text{ nm}^{-1}$), which reflects structural features of the individual particles, the profiles recorded at different pH values coincide within the experimental error limits (Fig. 6.8a). They also coincide with the $I(q)$ data for the silica without protein (Fig. 6.1a). This behavior is expected because in the present systems the scattering contrast of the protein against the solvent is negligibly small compared to that of silica. Hence the structural information from SAXS relates to the silica particles embedded in a uniform matrix. Differences in the aggregate structure of the silica particles are indicated by the low- q region of the scattering curves. Significant differences in $I(q)$ for the samples of different pH appear at $q < 0.3$. This low- q region of the scattering curves is shown on a non-logarithmic scale in Fig. 6.8b. Analysis of the scattering curves is based on the general relation [45]

$$I(q) = N(\Delta\rho)^2 |F(q)|^2 S(q) \quad (6.4)$$

where N is the number of particles in the scattering volume, $\Delta\rho = \rho_s - \rho_m$ the difference in electron density between the particles (s) and the matrix (m), $F(q)$ is the scattering amplitude of the individual particles, and $S(q)$ the structure factor describing the spatial correlations of the N particles, which is the information of interest in the present context. $S(q)$ was derived from the experimental scattering intensity data $I(q)$ by taking the contrast factor $(\Delta\rho)^2$ and the parameters of the form factor $\langle |F(q)|^2 \rangle$ of spheres with polydispersity s from the scattering curves of dilute silica dispersion in the absence of protein (Table 6.1). As mentioned in Sect. 6.2.1, weak repulsive interactions between silica nanoparticles exist in the

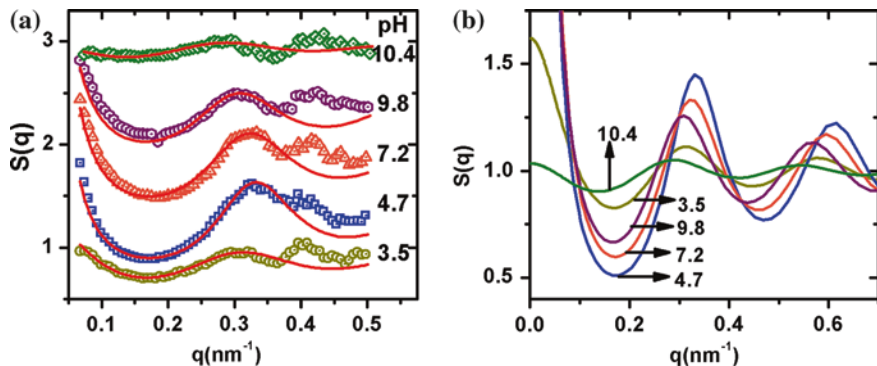


Fig. 6.9 Structure factor $S(q)$ for silica/lysozyme samples at different pH values: **a** data derived from the SAXS profiles of Fig. 6.8 (points) and fits by the SWPY model (lines); **b** comparison of the model $S(q)$ functions for the different pH values

absence of the protein due to the negative charge of the particles. In the analysis of the data of pure silica these interactions were taken into account by introducing a structure factor of a hard sphere system. In this way systematic errors in the determination of the single particle form factor (which would affect the determination of the structure factor in the silica/protein system) can be avoided. Results for the structure factor $S(q)$ of the silica/protein aggregates derived from the scattering curves at pH values from 3.5 to 10.4 are shown in Fig. 6.9a. Over the entire pH range, except the highest pH, the $S(q)$ curves exhibit a distinct peak at $q^* \simeq 0.30 \text{ nm}^{-1}$, as expected for the nearest-neighbor distance of hard particles of diameter $d = 2\pi/q^* \simeq 21 \text{ nm}$. A further characteristic feature of the samples at intermediate pH is the pronounced increase of $S(q)$ for $q \rightarrow 0$ at $q < 0.1$. This is a signature of systems exhibiting particle aggregation. Hence the structure factor results suggest that at intermediate pH values the silica particles with adsorbed protein behave like spheres with short-range attractive interactions which are causing particle aggregation.

The data in Fig. 6.9a indicate the existence of a secondary maximum in $S(q)$ at $q = 0.41 \text{ nm}^{-1}$. This feature is believed to be an artifact resulting from a slightly too high value of polydispersity s of the silica particles that is used in the evaluation of $S(q)$ from the scattering curves of the silica dispersion in the presence and absence of the protein (see Sect. 6.2.7). Accordingly, this feature of the experimental $S(q)$ data was neglected in the data analysis. The structure factor data were analyzed on the basis of a theoretical model for hard particles interacting by a short-range attractive potential [46]. A square-well potential was used to model hard spheres with an adhesive surface layer accounting for the adsorbed protein. The pair potential is defined as

$$U(r) = \begin{cases} +\infty & 0 < r < \sigma \\ -u & \sigma < r < \sigma + \Delta \\ 0 & r > \sigma + \Delta \end{cases} \quad (6.5)$$

where σ is the hard-core particle diameter, Δ is the well width and u the well depth. The Ornstein–Zernike equation in the Percus–Yevick (PY) approximation for this square-well potential can be solved analytically to the first order in a series expansion for small $\varepsilon = \Delta/(\sigma + \Delta)$, and the result for $S(q)$ can be expressed as a function of the four parameters σ , Δ , u and particle volume fraction φ . This square-well Percus–Yevick (SWPY) model transforms into Baxter’s sticky–hard–sphere (SHS) model in the combined limit $u \rightarrow \infty$ and $\Delta \rightarrow 0$. In the SHS model the pair interactions are characterized by a single parameter, the stickiness τ^{-1} , which is related to the parameters ε and u by Eq. 6.6.

$$\tau = \left(\frac{1}{12\varepsilon} \right) \exp \left(-\frac{u}{k_B T} \right) \quad (6.6)$$

with k_B , the Boltzmann constant and T , the temperature. τ has the significance of a dimensionless temperature and its inverse, $1/\tau$, is a measure of the stickiness of the particles. The case $1/\tau = 0$ corresponds to non-sticky hard spheres.

The numerical analysis of the $S(q)$ data in terms of the SWPY model was performed with the SASfit software package [47]. The hard-core particle diameter σ was taken from the form factor fit of the silica dispersion without protein ($\sigma = D = 21.5$ nm; see Table 6.1) and kept constant throughout the data analysis, while ε , τ , and φ were taken as adjustable parameters. Best-fit values of τ , $\Delta = \sigma\varepsilon/(1 - \varepsilon)$, and volume fraction φ , for a series of pH values of the sample are given in Table 6.4. As can be seen in Fig. 6.9a, the model reproduces the main features of the experimental $S(q)$ data, viz. the position and height of the nearest-neighbor peak at $q^* \approx 0.3$ nm⁻¹ and the sharp upward turn for $q \rightarrow 0$ below $q = 0.1$ which is observed at intermediate pH. These features can be attributed to a high stickiness of the particles, viz., $1/\tau > 10$ over a range of pH from 5 to 9. This high stickiness arises from the bridging of silica particles by lysozyme molecules. Table 6.4 indicates that the well-width Δ of the interparticle potential varies in a systematic way with pH, with rather low values in the region of pH 4–6 and higher values both at lower and higher pH. This pH dependence of the parameter Δ can be traced back to a variation of the position q^* of the next-neighbor peak in $S(q)$, which passes a maximum in the same pH range (Table 6.4). This trend of the peak position indicates that aggregate formation in the incomplete protein binding regime (pH 4–6) leads to a closer packing of silica particles than at lower and higher pH. Table 6.4 also reveals a drastic change in the aggregation behavior occurring in the narrow pH range from 9.8 to 10.4, as can be seen from the pronounced decrease of the potential-depth parameter $u/k_B T$ and increase in the well-width Δ . The stickiness parameter τ^{-1} , which is affected by both $u/k_B T$ and Δ , decreases to nearly one half of its value in this narrow pH range.

6.2.7 Influence of Polydispersity on the Evaluation of $S(q)$

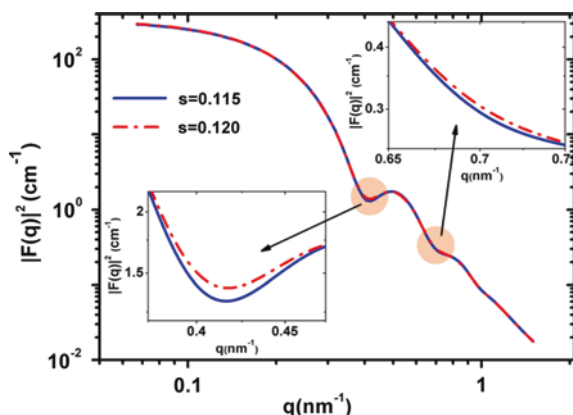
The structure factor $S(q)$ as determined from the experimental SAXS data is shown in Fig. 6.9a. In addition to the nearest-neighbor peak at $q \approx 0.3$ nm⁻¹, the data indicate a further peak at $q \approx 0.41$ nm⁻¹. Here we show that this second peak

Table 6.4 SWPY parameters from fits of the $S(q)$ data of the silica/lysozyme dispersion as a function of pH

| pH | u/kT | Δ (nm) | τ^{-1} | | q^* (nm^{-1}) |
|------|--------|---------------|-------------|------|----------------------------|
| 3.5 | 1.9 | 2.5 | 8.5 | 0.03 | 0.308 |
| 4.7 | 2.7 | 1.3 | 10.1 | 0.13 | 0.331 |
| 5.9 | 2.8 | 1.2 | 10.3 | 0.15 | 0.329 |
| 6.7 | 2.6 | 1.5 | 10.3 | 0.13 | 0.330 |
| 7.2 | 2.4 | 1.9 | 10.4 | 0.07 | 0.323 |
| 7.9 | 2.3 | 2.1 | 10.2 | 0.08 | 0.317 |
| 8.9 | 2.2 | 2.4 | 10.5 | 0.06 | 0.315 |
| 9.8 | 2.0 | 3.0 | 11.0 | 0.04 | 0.308 |
| 10.4 | 0.9 | 3.9 | 4.6 | 0.02 | 0.283 |

u and Δ represent the well depth and width of the particle–particle square-well potential, τ^{-1} is the stickiness parameter defined by Eq. 6.6, and φ is the volume fraction of particles resulting from the fit

Fig. 6.10 Simulated SAXS curves for 21.5 nm silica particles of polydispersities $s = 0.115$ (solid blue line) and $s = 0.120$ (dashed red line); the insets show the q -ranges of the first and second local minimum in the form factor on an enlarged scale. Different polydispersities are causing a significant effect in these regions



can be an artifact resulting from using a slightly too high value of polydispersity of the silica particles in the evaluation of the structure factor. Polydispersity is strongly affecting the form factor curve in the q -range of the first (and second) local minimum, but not elsewhere. This is illustrated in Fig. 6.10, where the scattering curves of isolated particles of polydispersities $s = 0.115$ and 0.120 are shown. In this case (mean particle diameter 21.5 nm) the first local minimum in $I(q)$ is located at 0.41 nm^{-1} . Figure 6.11 shows $S(q)$ functions calculated from simulated scattering curves of the aggregated system at pH 7.2 and 3.5 and scattering curves for isolated particles of polydispersity values from 0.115 to 0.135. In the simulation for pH 7.2 a shoulder in the nearest-neighbor peak, located around $q = 0.41 \text{ nm}^{-1}$ appears and becomes more pronounced with increasing polydispersity. In the simulation for pH 3.5, where the nearest-neighbor peak is smaller than at pH 7.2, a secondary peak located around $q = 0.41 \text{ nm}^{-1}$ appears, again increasing in magnitude with increasing polydispersity. These simulations strongly

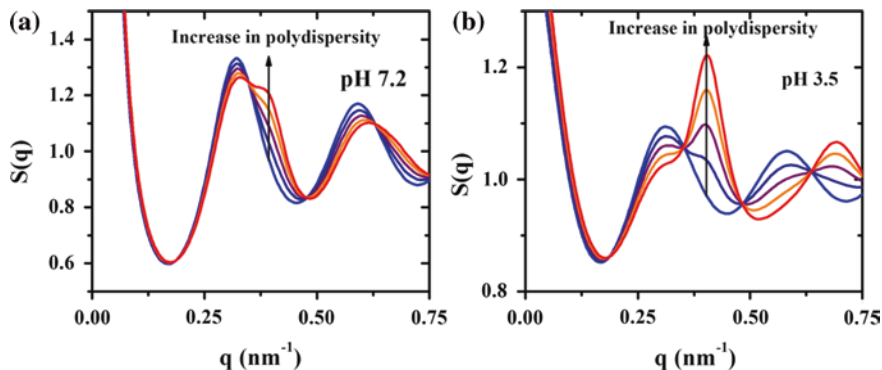


Fig. 6.11 Evolution of a secondary peak in $S(q)$ at $q \approx 0.41 \text{ nm}^{-1}$ with increasing values of polydispersity ($s = 0.115\text{--}0.135$): **a** pH 7.2; **b** pH 3.5

suggest that the feature at $q = 0.41 \text{ nm}^{-1}$ in the structure factor curves of Fig. 6.9a are indeed artifacts caused by slightly overestimating the particle polydispersity in the calculation of $S(q)$.

6.3 Discussion

The results presented in the preceding section show that the protein-mediated aggregation of the silica particles can be controlled to a large extent by pH. Here we attempt to account for these phenomena in terms of the complex interactions acting between the two types of particles in these systems. We first analyze the interactions responsible for the adsorption of the protein on isolated silica particles (Sect. 6.3.1) and then turn to the interaction between silica particles in the presence of the protein (Sect. 6.3.2). Finally we turn to the large-scale structure of the hetero-flocculate and the effect of pH on it and discuss the significance of the present work in relation to recent work of other groups (Sect. 6.3.3).

6.3.1 Nature of Adsorptive Interaction

The observed enhancement of the adsorption of lysozyme on silica nanoparticles with increasing pH is consistent with similar findings of Vertegel et al. [6] but at variance with a report that pH did not influence the surface concentration of lysozyme adsorbed at silica nanoparticles [22]. Henry's law constant K_H is a measure of the interaction of individual protein molecules with the surface. Its increase by two orders of magnitude in the pH range from 5 to 8.3 (Table 6.2) can be attributed to the increasing strength of attractive protein-surface electrostatic

interactions as the silica surface attains an increasingly negative charge with increasing pH. Figure 6.3a shows that the protein is not adsorbed at the silica particles under electrostatically repulsive conditions below pH 4, when the silica particles become positively charged. Our value of Henry's law constant at pH 7, $K_H \approx 10^{-4}$ m is smaller by a factor 10 than the value reported by Roth and Lenhoff [14] for lysozyme on a hydrophilic quartz surface at low ionic strength. The deviation can be attributed in part to errors inherent in our determination of K_H and differences in the surface chemistry of the two silica materials, but a more fundamental cause for the lower K_H may be the weaker dispersion interactions of the protein with the finite-size nanoparticles as compared with a semi-infinite flat substrate.

The progressive increase of the adsorption plateau value Γ_m with increasing pH (Table 6.2) can be attributed to the decreasing strength of repulsive protein–protein electrostatic interactions as the net charge of the molecules is gradually decreasing on approaching the isoelectric point. This result is in agreement with the work of van der Venn et al. [17], who presented convincing experimental evidence for the dominating influence of electrostatic interactions in the adsorption of lysozyme on a flat silica surface. We conclude that the same applies to the adsorption of the protein on the silica nanoparticles.

6.3.2 Protein-Induced Aggregation

In the pH range between the isoelectric points of the silica particles and lysozyme ($3 < \text{pH} < 11$) the adsorption of the protein is causing aggregation of the silica particles. Generally, bridging of two silica particles by protein molecules based on electrostatic interactions can be expected for proteins of high positive excess charge density but low dipole moment, i.e., when the excess charge is distributed more or less uniformly over their entire surface. Lysozyme (average surface charge density $+0.26e \text{ nm}^{-2}$, dipole moment 72 D at pH 7) [14] meets both of these conditions. Quantitative information about the protein-mediated interaction between the silica particles comes from the structure factor $S(q)$ (Fig. 6.9). In the pH range from 4.7 to 9.8, $S(q)$ exhibits a distinct nearest-neighbor peak and a strong increase for $q \rightarrow 0$ below 0.1 nm^{-1} . The combination of these features is a signature of systems interacting by a short-range attractive pair potential. From the fits of $S(q)$ with the SWPY model we find that the depth of the interparticle potential well is between $2k_B T$ and $3k_B T$, in line with the observation that aggregate formation is reversible with changes in pH. Closer inspection of the data in Table 6.4 indicates that the highest values of the pair interaction parameter $u/k_B T$ and lowest values of the well-width Δ are found in the pH range 4–6. In this regime of short-range interactions the sticky-hard-sphere model is well applicable to the present systems. For higher pH, somewhat lower values of interaction parameter $u/k_B T$ but larger values of the well-width are obtained. This suggests that the nature of the interactions responsible for the protein-mediated aggregation is gradually

changing with increasing pH, i.e., when the negative charge on the silica particles increases; the positive net charge of the protein molecules decreases. However, the stickiness parameter τ^{-1} does not reflect these changes but is nearly independent of pH in the range from pH 5 to 9, presumably due to the mutual compensation of the changes in $u/k_{\text{B}}T$ and Δ . Further work is needed to confirm these observations.

The remarkable fact that the scattering data can be represented by models with short-range attractive interactions leads to an interesting interpretation of the protein-induced aggregation of the silica particles. It is well-known that the SHS model fluid exhibits a critical point, the coordinates of which are $\tau_{\text{c}} \approx 0.098$ and $\varphi_{\text{c}} \approx 0.121$ [44]. The region $\tau > \tau_{\text{c}}$ represents the single-phase region, while for $\tau < \tau_{\text{c}}$ there is a domain of densities in which a gas-like phase coexists with a liquid-like phase. For the present system we find that τ^{-1} is nearly equal to the critical value $\tau_{\text{c}}^{-1} = 10.2$ in the pH range from 5 to 9 in which flocculation is observed (Table 6.4). In this pH range, the silica dispersion can be considered to be in a near-critical state, characterized by a high osmotic compressibility, in agreement with the observed sharp rise of $S(q)$ for $q \rightarrow 0$ below $q = 0.1 \text{ nm}^{-1}$. The drastic change in the aggregation behavior occurring between pH 9.8 and pH 10.4 is also reflected in $S(q)$ (Fig. 6.9). At pH 10.4, $S(q)$ exhibits only a small hump in the q range of nearest-neighbor distances and is nearly flat at lower q . A fit by the SWPY model yields a shallow attractive potential corresponding to a much lower stickiness than at pH below 10 (Table 6.4). Qualitatively, this behavior can be attributed to the sharp decrease in positive net charge of lysozyme in the pH range close to its IEP (see Fig. 6.4), which implies that the attractive bridging energy will sharply decrease in this pH range.

6.3.3 Interparticle Bonds and Flocculate Structure

The average coordination of a silica particle in the aggregates can be assessed from the height of the nearest-neighbor peak in $S(q)$. The fits of the $S(q)$ data with the SWPY model indicate that this nearest-neighbor peak is most pronounced in the pH range 4–6, where it reaches a maximum of about 1.5 (Fig. 6.9b). At higher pH values, the nearest-neighbor peak becomes less pronounced, indicating a somewhat lower coordination number of the silica particles in the aggregates. One expects that a high coordination number of the particles in the aggregates will lead to a lower mean volume of the aggregate. The sediment volumes V_{c} , resulting from the centrifugation study (Table 6.3) are indeed showing this trend, i.e. lower sediment volumes at pH 5.5 than at higher pH. These findings imply that the coordination number of the silica particles in the aggregates is highest at pH values at which only a fraction of the protein molecules is bound to the silica surface. This may be rationalized by the argument that a bridging contact between two silica particles requires just one (or a few) protein molecules, while protein molecules adsorbed vis-à-vis on neighboring particles but not involved in a bridging contacts will repel each other due to their net positive charge. This repulsive

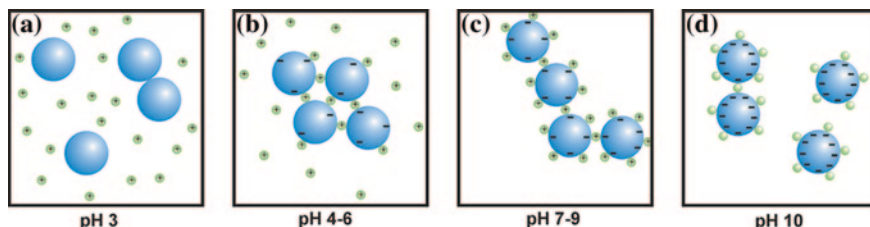


Fig. 6.12 Sketch of aggregate structures formed by silica nanoparticles with the protein in different pH regimes: **a** At pH 3 (near the IEP of silica) no protein adsorption but weak aggregation of silica particles due to lacking charge stabilization; **b** in the partial protein binding regime (pH 4–6) bridging aggregation leads to fairly compact aggregates; **c** in the complete protein binding regime (pH 7–9) a loosely aggregated network is formed due to repulsive interactions of non-bridging protein molecules on neighboring silica particles and the increasingly negative charge of the silica particles; **d** at pH 10 (near the IEP of the protein) silica particles with adsorbed protein become charge stabilized and only small aggregates persist

protein–protein interaction may indeed favor structures of lower coordination number of the silica particles, as such open structures will minimize the repulsive interaction between pairs of non-bridging protein molecules adsorbed near the contact point on the two particles. The drastic change in the aggregation behavior in the narrow pH range from 9.8 to 10.4 represents one of the most remarkable findings of this work. This change is evidenced by the sharp decrease of the sedimentation velocity and aggregate size as derived from the centrifugation experiments (Table 6.3), as well as the sharp change in the low- q behavior of the SAXS scans (Fig. 6.8). As mentioned above, this can be attributed qualitatively to a relatively sharp decrease of the attractive bridging energy of lysozyme and a concomitant increase of the repulsive electrostatic interaction between the protein-decorated silica particles.

The proposed evolution of aggregate structures of silica particles induced by lysozyme as a function of pH is sketched in Fig. 6.12. At a pH close to the IEP of silica, protein is not adsorbed and the absence of charge stabilization will cause a weak aggregation of silica particles (Fig. 6.12a). In the regime of incomplete protein binding to the silica particles (pH 4–6), protein adsorption will cause bridging aggregation. Initially, the number of bonds should increase with the number of adsorbed protein molecules per silica particle. This may lead to aggregates of relatively high mean coordination number of the silica particles, and thus high packing density in the flocculate (Fig. 6.12b). In the complete protein-binding regime (pH 7–9), adsorption of further protein that is not involved in particle bridging may cause repulsive interactions which may lead to aggregates of lower coordination number of the silica particles, and thus a looser packing of the flocculate (Fig. 6.12c). Finally, at a pH close to the IEP of the protein, the flocculate is redispersed to monomers and small aggregates due to charge stabilization of the silica (Fig. 6.12d). Further work is needed to confirm this proposed evolution. Specifically, the transition from dense to loose aggregate structures (Fig. 6.12c, d)

may be elucidated by studying the effect of ionic strength, which affects the range of repulsive interactions between non-bridging protein molecules. SAXS data covering a q range to $<0.01 \text{ nm}^{-1}$ (real space distances on the order of 600 nm) would be needed to gain a better understanding of the large-scale structure of the aggregates as a function of pH.

The protein-mediated aggregation of silica nanoparticles studied here bears some analogy with the aggregation of silica nanoparticle induced by the addition of Al_{13} polycations as reported by Parneix et al. [48] In that case, however, the situation is complicated by the fact that the interaction of Al_{13} with the silica surface takes place in two stages: in the first, Al_{13} polycations react with the surface silanols and the Al atoms change their coordination to form a layer of negatively charged aluminosilicate sites. When more Al_{13} is added, then in a second step these Al_{13} polycations adsorb to the negative aluminosilicate surface and may induce aggregation of the silica by bridging of particles by Al_{13} polycations. Hence the Al_{13} polycations added in the second step take the role of the protein in the present case. Parneix et al. [48] submitted their samples to osmotic compression and studied the structural changes induced by the compression by small-angle neutron scattering. Significant differences in the compression law were found depending on the way in which the samples were prepared. It would be of interest to perform a similar study with our samples in which pronounced structural changes can be induced by small changes in pH.

6.4 Conclusions

This study has demonstrated the important role of electrostatic interactions in the adsorption of lysozyme on silica nanoparticles and in the protein-mediated aggregation of the silica particles. It was found that the adsorption capacity for lysozyme increases progressively from the isoelectric points of silica to the isoelectric point of the protein. If the amount of protein per silica particle is limited, the zeta potential first increases to positive values with increasing pH but later turns to negative values and approaches the zeta potential of the bare silica particles near the isoelectric point of the proteins. These trends of the zeta potential qualitatively reflect the changes in the overall charge of the protein-decorated silica particles, even though the electrophoretic mobility cannot be represented quantitatively by a simple algebraic summation of charges of the protein decorated particles.

The study provides strong evidence that the aggregation of silica nanoparticles is due to a bridging by lysozyme molecules, although direct imaging of the protein was not achieved by cryo-TEM. Concordant information about the structure of the silica-protein hetero-aggregates could be derived from the sedimentation study and the SAXS measurements. It was found that the local structure of the aggregates as well as the large-scale structure of the flocculate depends on the number of bound lysozyme molecules. The size of the nearest-neighbor peak in the structure factor

indicates that the number of nearest neighbors in the aggregate decreases when the number of bound protein molecules increases. This is consistent with a higher sediment volume of the flocculates under these conditions and may be rationalized from the fact that away from their isoelectric point protein molecules adsorbed vis-a-vis on neighboring silica particles are repelling each other and thus may favor a less dense packing of the silica particles.

References

1. Moyano DF, Rotello VM (2011) Nano meets biology: structure and function at the nanoparticle interface. *Langmuir* 27:10376
2. Nam JM, Thaxton CS, Mirkin CA (2003) Nanoparticle-based bio-bar codes for the ultrasensitive detection of proteins. *Science* 301:1884
3. Brigger I, Dubernet C, Couvreur P (2002) Nanoparticles in cancer therapy and diagnosis. *Adv Drug Deliv Rev* 54:631
4. Vivero-Escoto JL, Slowing II, Wu C-W, Lin VSY (2009) Photoinduced intracellular controlled release drug delivery in human cells by gold-capped mesoporous silica nanosphere. *J Am Chem Soc* 131:3462
5. Roach P, Farrar D, Perry CC (2006) Surface tailoring for controlled protein adsorption: effect of topography at the nanometer scale and chemistry. *J Am Chem Soc* 128:3939
6. Vertegel AA, Siegel RW, Dordick JS (2004) Silica nanoparticle size influences the structure and enzymatic activity of adsorbed lysozyme. *Langmuir* 20:6800
7. Peng ZG, Hidajat K, Uddin MS (2004) Adsorption and desorption of lysozyme on nano-sized magnetic particles and its conformational changes. *Colloids Surf B: Biointerfaces* 35:169
8. Henzler K, Haupt B, Lauterbach K, Wittemann A, Borisov O, Ballauff M (2010) Adsorption of β -lactoglobulin on spherical polyelectrolyte brushes: direct proof of counterion release by isothermal titration calorimetry. *J Am Chem Soc* 132:3159
9. Janes KA, Calvo P, Alonso MJ (2001) Polysaccharide colloidal particles as delivery systems for macromolecules. *Adv Drug Deliv Rev* 47:83
10. Cardoso MB, Luckarift HR, Urban VS, O'Neill H, Johnson GR (2010) Protein localization in silica nanospheres derived via biomimetic mineralization. *Adv Funct Mater* 20:3031
11. Slowing II, Trewyn BG, Lin VS-Y (2007) Mesoporous silica nanoparticles for intracellular delivery of membrane-impermeable proteins. *J Am Chem Soc* 129:8845
12. Lee DW, Park KM, Banerjee M, Ha SH, Lee T, Suh K, Paul S, Jung H, Kim J, Selvapalam N, Ryu SH, Kim K (2011) Supramolecular fishing for plasma membrane proteins using an ultrastable synthetic host-guest binding pair. *Nat Chem* 3:154
13. Rana S, Yeh Y-C, Rotello VM (2010) Engineering the nanoparticle-protein interface: applications and possibilities. *Curr Opin Chem Biol* 14:828
14. Roth CM, Lenhoff AM (1995) Electrostatic and van der Waals contributions to protein adsorption: comparison of theory and experiment. *Langmuir* 11:3500
15. Czeslik C, Royer C, Hazlett T, Mantulin W (2003) Reorientational dynamics of enzymes adsorbed on quartz: a temperature-dependent time-resolved TIRF anisotropy study. *Biophys J* 84:2533
16. Wahlgren M, Arnebrant T, Lundström I (1995) The adsorption of lysozyme to hydrophilic silicon oxide surfaces: comparison between experimental data and models for adsorption kinetics. *J Coll Interface Sci* 175:506
17. van der Veen M, Norde W, Cohen Stuart M (2004) Electrostatic interactions in protein adsorption probed by comparing lysozyme and succinylated lysozyme. *Colloids Surf B* 35:33
18. Hollmann O, Steitz R, Czeslik C (2008) Structure and dynamics of α -lactalbumin adsorbed at a charged brush interface. *Phys Chem Chem Phys* 10:1448

19. Lundqvist M, Sethson I, Jonsson BH (2004) Protein adsorption onto silica nanoparticles: conformational changes depend on the particles' curvature and the protein stability. *Langmuir* 20:10639
20. Asuri P, Karajanagi SS, Yang HC, Yim TJ, Kane RS, Dordick JS (2006) Increasing protein stability through control of the nanoscale environment. *Langmuir* 22:5833
21. Shang W, Nuffer JH, Muniz-Papandrea VA, Colon W, Siegel RW, Dordick JS (2009) Cytochrome c on silica nanoparticles: influence of nanoparticle size on protein structure, stability, and activity. *Small* 5:470
22. Wu X, Narsimhan G (2008) Effect of surface concentration on secondary and tertiary conformational changes of lysozyme adsorbed on silica nanoparticles. *Biochim Biophys Acta* 1784:1694
23. Kendall M, Ding P, Kendall K (2011) Particle and nanoparticle interactions with fibrinogen: the importance of aggregation in nanotoxicology. *Nanotoxicology* 5:55
24. Dutta D, Sundaram SK, Teeguarden JGB, Riley J, Fifield LS, Jacobs JM, Addleman SR, Kaysen GA, Moudgil BM, Weber TJ (2007) Adsorbed proteins influence the biological activity and molecular targeting of nanomaterials. *Toxicology Sci* 100:303
25. Thomassen LCJ, Aerts A, Rabolli V, Lison D, Gonzalez L, Kirsch-Volders M, Napierska D, Hoet PH, Kirschhock CEA, Martens JA (2010) Synthesis and characterization of stable monodisperse silica nanoparticle sols for in vitro cytotoxicity testing. *Langmuir* 26:328
26. Stradner A, Sedgwick H, Cardinaux F, Poon WCK, Egelhaaf SU, Schurtenberger P (2004) Equilibrium cluster formation in concentrated protein solutions and colloids. *Nature* 432:492
27. Liu Y, Fratini E, Baglioni P, Chen WR, Chen SH (2005) Effective long-range attraction between protein molecules in solutions studied by small angle neutron scattering. *Phys Rev Lett* 95:118102
28. Cardinaux F, Stradner A, Schurtenberger P, Sciortino F, Zaccarelli E (2007) Modeling equilibrium clusters in lysozyme solutions. *Europhys Lett* 77:48004
29. Shukla A, Mylonas E, Cola ED, Finet S, Timmins P, Narayanan T, Svergun DI (2008) Absence of equilibrium cluster phase in concentrated lysozyme solutions. *Proc Natl Acad Sci* 105:5075
30. Porcar L, Falus P, Chen WR, Faraone A, Fratini E, Hong K, Baglioni P, Liu Y (2010) Formation of the dynamic clusters in concentrated lysozyme protein solutions. *J Phys Chem Lett* 1:126
31. Schaefer DW, Martin JE, Wiltzius P, Cannell DS (1984) Fractal geometry of colloidal aggregates. *Phys Rev Lett* 52:2371
32. Bian SW, Mudunkotuwa IA, Rupasinghe T, Grassian VH (2011) Aggregation and dissolution of 4 nm ZnO nanoparticles in aqueous environments: influence of pH, ionic strength, size, and adsorption of humic acid. *Langmuir* 27:6059
33. Ang JC, Lin JM, Yaron PN, White JW (2010) Protein trapping of silica nanoparticles. *Soft Matter* 6:383
34. Wong K, Lixon P, Lafuma F, Lindner P, Charriol-Aguerre O, Cabane B (1992) Intermediate structures in equilibrium flocculation. *J Colloid Interface Sci* 153:55
35. Babayan D, Chassenieux C, Lafuma F, Ventelon L, Hernandez J (2010) Formation of rodlike silica aggregates directed by adsorbed thermoresponsive polymer chains. *Langmuir* 26:2279
36. Bagwe RP, Hilliard LR, Tan W (2006) Surface modification of silica nanoparticles to reduce aggregation and nonspecific binding. *Langmuir* 22:4357
37. Goller MI, Barthet C, McCarthy GP, Corradi R, Newby BP, Wilson SA, Armes SP, Luk SY (1998) Synthesis and characterization of surface-aminated polypyrrole-silica nanocomposites. *Colloid Polym Sci* 276:1010
38. Arai S, Hirai M (1999) Reversibility and hierarchy of thermal transition of hen egg-white lysozyme studied by small-angle X-ray scattering. *Biophys J* 76:2192
39. Lugo DM, Oberdisse J, Lapp A, Findenegg GH (2010) Effect of nanoparticle size on the morphology of adsorbed surfactant layers. *J Phys Chem B* 114:4183
40. Rezwani K, Studart AR, Vörös J, Gauckler LJ (2005) Change of ζ potential of biocompatible colloidal oxide particles upon adsorption of bovine serum albumin and lysozyme. *J Phys Chem B* 109:14469

41. Wu Z, Xiang H, Kima T, Chun MS, Lee K (2006) Surface properties of submicrometer silica spheres modified with aminopropyltriethoxysilane and phenyltriethoxysilane. *J Colloid Interface Sci* 304:119
42. Hunter R (1981) *Zeta potential in colloid science*. Academic Press, New York
43. Posse E, Vitals AL, de Arcuri BF, Farias RN, Morero RD (1990) Lysozyme induced fusion of negatively charged phospholipid vesicles. *Biochim Biophys Acta* 1024:390
44. Pan X, Yu S, Yao P, Shao Z (2007) Self-assembly of β -casein and lysozyme. *J Colloid Interface Sci* 316:405
45. Glatter O, Kratky O (1983) *Small-angle X-ray scattering*. Academic Press, New York, USA
46. Regnaut C, Ravey JC (1989) Application of the adhesive sphere model to the structure of colloidal suspensions, *J Chem Phys* 91:1211
47. <http://kur.web.psi.ch/sans1/SANSSoft/sasfit.html>
48. Parneix C, Persello J, Schweins R, Cabane B (2009) How do colloidal aggregates yield to compressive stress? *Langmuir* 25:4692

Chapter 7

Effect of pH and Salinity on Silica–Lysozyme Hetero-Aggregation

7.1 Introduction

The interactions of nanomaterials with biological entities have been the focus of many recent studies [1–4]. The attachment of biochemical quantities like proteins to synthetic functional materials have found their applicability in protein-purification strategies, bacterial detections [5], protein fibrillation [6], biosensors and drug delivery systems [7]. There have been a number of attempts to study the interaction of globular proteins with hydrophilic surface [8, 9]. These interactions form the basis for studying the complex interactions occurring between nanoscale materials with biological matter like living cell [10, 11]. Protein adsorption on a flat or a curved surface is a complex process in which the structural stability of a protein, the ionic strength, the pH of the solution and the hydrophobicity or hydrophilicity of the interacting surfaces are known to influence the protein binding affinity to the given interface [12]. The adsorption of proteins to nanoparticles not only brings about the changes in the protein secondary and tertiary structures but also affects the surface properties and stability of the sorbent particle solution. Hence, studying the changes induced in a nanoparticle dispersion by protein adsorption is of great relevance, both in industrial and medical processes. The interactions of hydrophilic silica surface with entities such as proteins and polymers have been the center of attraction in the recent times, for example, Aggregation of the human platelets by amorphous silica has been reported by Corbalan et al. [13] Larsericsdotter et al. [14] have systematically studied the effects of electrostatic interactions on the adsorption of lysozyme, ribonuclease A, and R-lactalbumin on silica surface by varying the ionic strength. Wong et al. [15] have studied the bridging flocculation of highly charged silica nanoparticles by long poly(ethylene oxide) polymer chains. This study revealed that the range of the electrostatic repulsive forces, controlled by the ionic strength, strongly affects the shape of the floccs. When the ionic strength is sufficiently low, for example, 1 mM, the floccs are linear and their fractal

Modified with permission from Bharti, B., Meissner, J., Gasser, U., Findenegg, G. H., *Soft Matter*, **2012**, 8, 2573. Copyright 2014. The Royal Society of Chemistry.

dimension increases with the ionic strength. Long range repulsive forces are therefore, a key feature in tuning the colloidal floccs structure. In our previous study [16] we have reported the bridging hetero-aggregation of silica nanoparticles by lysozyme. The pH responsive aggregation phenomenon was studied in association with the binding affinity of lysozyme molecules to the silica surface. The aggregation behavior proved to be completely switchable with pH. In this work, we dig deeper to have a better understanding of the electrostatically driven heteroaggregation process of protein with nanoparticles.

In the present study, we explore the effects of dispersion salinity on the lysozyme binding to silica surface within a wide pH regime (3–11). We use adsorption measurements to characterize the amount of protein bound to the silica at a given pH and salinity condition. The nature of protein induced silica aggregation was strongly dependent on the dispersion salinity. The protein/silica composite aggregates formed were characterized by turbidity, Small Angle X-ray Scattering (SAXS) and analytical centrifugation measurements. We interpret the results on the basis of different forces involved in the adsorption and aggregation process. In Sect. 7.2 we present the results obtained by studying the silica/lysozyme system at various pH/salinity and protein concentration. In Sect. 7.3, we try to explain the observed behavior and compare our results with some previously reported theoretical and experimental work.

7.2 Results

7.2.1 Adsorption Isotherms

The effect of ionic strength on the binding affinity of lysozyme to silica nanoparticles was investigated by adsorption isotherms. The details for the adsorption isotherm measurements are given elsewhere [16]. Protein-nanoparticle binding was studied at pH = 8.3 in bicine buffer, over a wide NaCl concentration (c_{NaCl}) range (Table 7.1). Figure 7.1a shows such adsorption isotherms at ionic strengths varying from 0 to 100 mM. In the figure, the amount of lysozyme bound to silica is expressed as milligrams of protein adsorbed per unit surface area of silica nanoparticles (Γ) as a function of unbound or free protein in the dispersion. The lines in Fig. 7.1a are the fits to the experimental data by Langmuir adsorption model, $\Gamma = \Gamma_m Kc / (1 + Kc)$, where, c is the free protein concentration in solution, Γ_m is the maximum surface excess concentration, and the parameter K is the binding constant. At constant temperature, the value of K increases with the increase in binding energy of adsorption. The isotherms at all the salinities show a rather rapid accumulation of the protein on the surface of nanoparticles which is followed by the plateau, where no more lysozyme is further adsorbed. The plateau values at different ionic strengths were obtained by fitting the individual data set to the Langmuir adsorption model. Figure 7.1b represents the plot of Γ_m (best fit values) as a function of c_{NaCl} . Here the Γ_m (triangles) shows a sudden decrease with the

Fig. 7.1 a Adsorption isotherms of lysozyme on silica at different salinities, the concentration of NaCl (mM) (c_{NaCl}) are indicated next to each adsorption curve. Scattered points are the experimentally measured data set and *solid lines* are the best fit obtained by *Langmuir*-adsorption model (see text), **b** maximum amount of lysozyme bound (Γ_m) to silica nanoparticle (*right triangles*) decreases with increasing NaCl amount (c_{NaCl}), where as nominal surface area per lysozyme molecule shows an increase indicative of lesser crowding at the surface at higher salinities

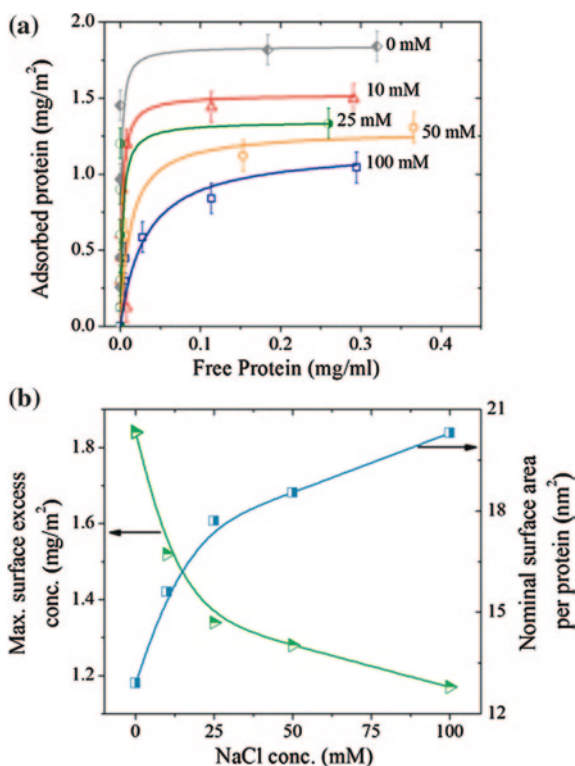


Table 7.1 *Langmuir*-adsorption-model fit parameters for adsorption isotherms with increasing dispersion salinities (Fig. 7.1)

| c_{NaCl} | Γ_m | K | A_m |
|-------------------|------------|-----|-------|
| 0 | 1.84 | 760 | 13 |
| 10 | 1.52 | 427 | 16 |
| 25 | 1.34 | 353 | 18 |
| 50 | 1.28 | 80 | 19 |
| 100 | 1.17 | 32 | 20 |

c_{NaCl} is the concentration of salt in millimoles per litre, Γ_m is the maximum surface excess concentration (mg/m^2), K is the Langmuir adsorption constant and A_m is the nominal surface area per lysozyme adsorbed

increasing c_{NaCl} i.e. the maximum protein (in mg/m^2) that can be loaded on the silica nanoparticles decreases over 30 % as the amount of salt in dispersion was increased from 0 to 100 mM. This finding is in agreement with the recent ellipsometry and neutron reflection study of salinity effect on the lysozyme adsorption to a flat hydrophilic silica surface [17, 18]. Figure 7.1b also shows the dependence of nominal surface area occupied per lysozyme (A_m) on the silica surface (squares) as the function of NaCl concentration. Clearly, increase in the salinity results in the decrease of protein crowding on the silica surface.

7.2.2 *pH Driven Lysozyme Binding*

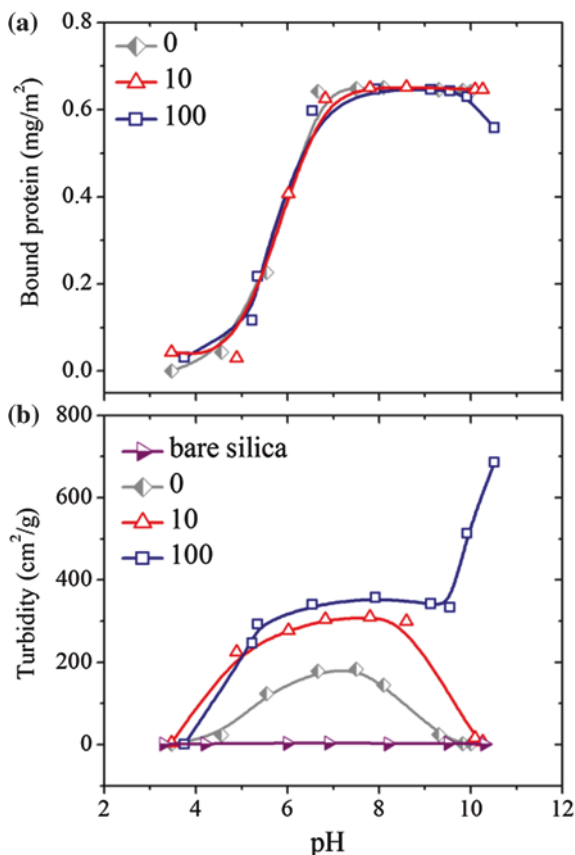
The tedious task of understanding the role of electrostatic interactions in protein adsorption onto silica nanoparticles and thus induced aggregation of silica particles was achieved by the detour of pH titrations. The pH titrations were carried out at fixed amounts of silica (1 wt%) and lysozyme. The concentration of lysozyme used in the pH titrations corresponds to the surface coverage of 0.65 mg/m^2 which estimates to be 40 lysozyme molecules adsorbed per silica particle (γ). pH change of a silica/lysozyme dispersion results in the variation of surface charges both on silica as well as on lysozyme. In order to manipulate the electrostatic interactions at fixed silica and lysozyme surface charges (fixed pH), a 1:1 monovalent electrolyte NaCl was added which results in the screening of charges and suppresses the active electrostatic forces between all existing inter- and intra-particle charged species. The amount of salt in the dispersion determines the extent of screening of electrostatic interactions. For manipulating the electrostatic interactions over a large scale, up to 100 mM NaCl was added to the pH titrations dispersions keeping a fixed silica and protein concentration. The experimental results of such protein binding experiments (Γ vs. pH) at different medium salinities are presented in Fig. 7.2a. The protein binding behavior at low ionic strengths is similar to our previously reported data of pH titration [16]. The momentous increase in the binding capacity of protein on silica particles above pH 4 was attributed to the rapid increase of surface charge on silica. The monotonous behavior observed above pH 7 was explained by the fact that beyond this pH, whole protein has been locked at the silica surface and the medium is deprived of any protein. As can be seen in Fig. 7.2a, the curves for 3 different ionic strengths of solutions are alike and pose no major variations. The observation can be correlated with the adsorption isotherms in Fig. 7.1, since the concentration of lysozyme used in the experiments was 1.2 mg/ml , which corresponds to a surface excess of 0.65 mg/m^2 , this value is below the Γ_m for all salinities. Hence up to this surface loading of lysozyme, the binding affinity and the adsorption behavior of the protein is independent of pH, i.e. a sharp increase in adsorption at $\text{pH} > 4$ followed by the flat region at $\text{pH} > 7$ where all protein is in bound state.

7.2.3 *Aggregation of Protein/Silica Core-Shell Composite*

7.2.3.1 *Turbidity*

The adsorption of lysozyme was accompanied by the aggregation of silica nanoparticles. The observed aggregation was quantified by monitoring the changes in the turbidity values of the samples at different ionic strengths and pH values. Turbidity of the samples were estimated by the transmittance values (T_r) at 800 nm wavelength by the relation, $\text{Turbidity} = -(\log_{10} T_r)/l c_{\text{si}}$, where l is the optical path length of the transmitted beam and c_{si} is the concentration of silica

Fig. 7.2 **a** Amount of lysozyme bound (Γ) per unit surface area of silica in pH titration experiments for 1 wt% dispersion with fixed amount of lysozyme (1.2 mg/mL) at different salinities, the numbers in the graph are the ionic strengths of the dispersion in mM. **b** Change in turbidity of the pH titration experiments, containing no lysozyme (*right triangles*), added lysozyme with 0 (*diamond*), 10 (*up triangles*) and 100 mM (*squares*) NaCl



in the dispersion. The turbidity values obtained at different pH for solutions having different amounts of NaCl are given in Fig. 7.2b. No change in turbidity was observed for the pH titration of only silica dispersion. However, for the samples with added protein at low salinities i.e. no externally added NaCl, there was an increase in the turbidity when the $\text{pH} > 4$, which passes through the maximum and goes to lower values at $\text{pH} > 9$. The increase in turbidity at intermediate pH regime was the signature of lysozyme mediated aggregation [16, 19]. In the presence of 10 mM NaCl, although the qualitative behavior of the sample during the course of pH change remains the same, but the absolute magnitude of turbidity increases in comparison to the sample with no added salt. The increase in the absolute value of turbidity at a constant silica and protein concentration is the indicative of the formation of larger aggregates. Despite of the similar aggregation behavior at $\text{pH} < 9$, the aggregation response with $\text{pH} > 9$ at higher salinities is far different. For the samples above pH 9 at a 50 and 100 mM NaCl dispersion concentration, instead of decrease in turbidity (as is the case with lower salt concentrations), it increases for rest of the studied pH range. The plausible implications of the observed behavior of the dispersion salinity are discussed in the Sect. 7.3.2.

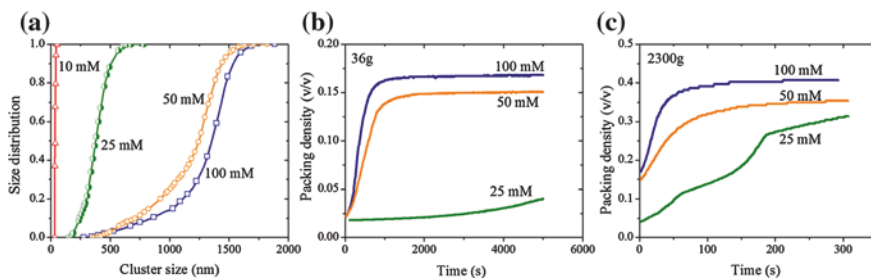


Fig. 7.3 **a** Cumulative size distribution for silica-lysozyme aggregates at four different salinities indicating the increase in average floc size with NaCl concentration. **b** and **c** The packing density of the silica/lysozyme aggregates at different dispersion salinities deduced by the sedimentation kinetics measured at 36 g and 2,300 g respectively

Table 7.2 Statistical size distribution of the aggregates formed at $\text{pH} \approx 11$ at different salinities

| c_{NaCl} | θ | ω | $\leq 10\%$ | $\leq 50\%$ | $\leq 90\%$ |
|-------------------|----------|----------|-------------|-------------|-------------|
| 10 | 37 | 4 | 33 | 36 | 42 |
| 25 | 350 | 99 | 243 | 377 | 510 |
| 50 | 1,056 | 282 | 712 | 1,245 | 1,440 |
| 100 | 1,167 | 289 | 828 | 1,362 | 1,547 |

c_{NaCl} is the concentration of NaCl used (mM), θ is the mean cluster size (nm) and ω is the standard deviation (nm) of the distribution from the mean size

7.2.3.2 Analytic Centrifuge

The silica/lysozyme aggregate structure and their size distribution was obtained by analytical ultra-centrifugation technique (LUM GmbH, Berlin Germany) [20, 21]. The particle size distribution was determined by time evolution of transmission at fixed sample height as explained elsewhere [22]. Figure 7.3a represents the cumulative volume weighted size distributions obtained for the samples at $\text{pH} \approx 11$ at four dispersion ionic concentrations. At low salinities (10 mM), narrow aggregate size distribution between 30 and 40 nm was obtained with a small fraction of particles upto 80 nm. On increasing the salt concentration, the cumulative size distributions are shifted to larger values. Increase in the salt concentration from 50 to 100 mM leads to only a small increase in size of the aggregate. Table 7.2 summarizes the percentage of cluster size distribution in different length scales. A ten-fold increase in the dispersion salinity (10 \rightarrow 100 mM) resulted in the increase of aggregate size by a factor 40. Growth of the aggregate with ionic strength is in complete agreement with the observed increase in turbidity values at corresponding salinities (Fig. 7.2b).

Sedimentation kinetics of the silica/lysozyme aggregates at pH 11 was used to estimate the fractional volume occupied by the flocs (so called the “*packing density*”). During the process of centrifugation, the intensity of transmitted light over the whole sample length was monitored as a function of time. Sedimentation experiments performed at different salt concentrations (at pH 11) demarcates the

lysozyme/silica aggregates from the dispersion medium (75 % limiting transmission value) by a phase boundary. The evolution and the shifts in the phase boundaries at 36 and 2,300 g of centrifugal force were obtained as the function of elapsed time (not shown). Average packing density (d_{agg}) of the aggregates at two centrifugation speeds was estimated from the total mass of silica (m) in the sample by the relation [23].

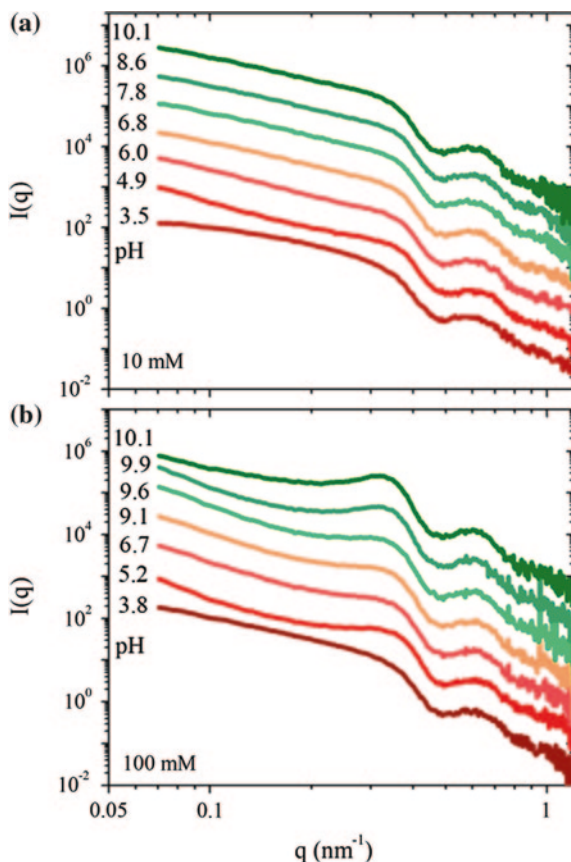
$$d_{agg} = \frac{m}{\rho_{mass}V_{sed}} \quad (7.1)$$

where ρ_{mass} is the difference in the mass densities of silica and water and V_{sed} is the sediment volume estimated from sedimentation experiments. Here, for the simplicity reasons, we assume that upon the phase separation whole silica exists as aggregate i.e. it is present only in the denser phase Fig 7.3b and c show the calculated packing densities of silica/lysozyme composites at pH 11 at different NaCl concentration. Since the silica/lysozyme dispersion at 10 mM NaCl and pH 11 was stable (no phase separation), sedimentation kinetics study of the same was not performed. The packing density profiles of aggregates obtained for 25, 50 and 100 mM NaCl at 36 g centrifugal force is depicted in Fig. 7.3b. As can be observed from the figure, at constant stress of 36 g, the packing density increases steeply over time for dispersions at high salt concentrations whereas, at 25 mM NaCl the packing density remains low at prolonged exposure to the constant compressive stress. Higher packing density of the dispersion at constant silica concentration is the indicative of larger and compact aggregates at higher salt concentrations. Interestingly, the limiting packing density at 50 and 100 mM was observed to be 0.14 and 0.16, respectively and this value is attained rapidly whereas, for 25 mM no sharp boundary in the separation existed even after a prolonged centrifugation time. This result reconfirms the particle size distribution presented in Fig. 7.3a. The samples were also subjected to extended compression stress of 2,300 g leading to the higher packing density of the flocs. Here again the limiting packing density of 0.4 and 0.34 for 50 and 100 mM NaCl respectively was attained but in the experimental time scale this limiting value was never achieved for dispersions at 25 mM NaCl. Here we would like to point out that because of the weaker aggregation the error in the determination of the phase boundary and thus packing density for aggregate at 25 mM is higher than in the case of strongly aggregated dispersions (50 and 100 mM).

7.2.3.3 Small Angle X-ray Scattering

To relate the protein-induced silica nanoparticle aggregation with the interaction potential between silica nanoparticles, Small Angle X-ray Scattering (SAXS) measurements were performed for the pH titration at different ionic strengths. Typical scattering profiles of the samples containing 10 and 100 mM NaCl are shown in Fig. 7.4a, b respectively. The scattering intensity is plotted as the function of scattering vector q , given by $(4\pi/\lambda)\sin\theta$; where λ is the wavelength of

Fig. 7.4 Radial averaged SAXS intensity $I(q)$ profile as the function of scattering vector q on log-log scale, for a silica dispersion containing 1.1 mg/ml of lysozyme at different pH at **a** 10 mM; and **b** 100 mM dispersion salinity. For better visualization each scattering curve has been shifted upwards by the constant factor of 5 and the equilibrium pH has been indicated next to the curve



X-ray beam and 2θ is the scattering angle. In the case of X-ray scattering, it needs to be kept in mind that the scattering solely arises from silica nanoparticles and its aggregate structure and the contribution of the lysozyme towards the overall scattering is negligible. The oscillation appearing in the scattering curves (Fig. 7.4a, b) is the signature of spherical shaped silica nanoparticles. The scattering curves in Figs. 7.4a, b are identical at $q > 0.3 \text{ nm}^{-1}$ (on a non-shifted scale; not shown), indicating the absence of any change in the local spherical structure (shape) of the silica nanoparticles during the aggregation process. However, an increase in the intensity can be observed in low- q regions of the scattering profiles, which is typical for the aggregating nanoparticle systems [16]. In the case of 10 mM NaCl pH titration (Fig. 7.4a), the SAXS profile at pH 3.5 represents the flattening of the profile in low- q Guinier regime, characteristic of the stable silica dispersion and is analogous to the profile of bare silica nanoparticle. Because of the lack of any attractive electrostatic interaction between protein and silica surface at this pH, no protein molecule binds to the silica particle and the silica dispersion remains stable against aggregation. As the pH is increased, the charge on the silica surface increases resulting into an attractive interaction between silica and protein, and

at $\text{pH} > 4$, lysozyme binds to silica surface and initiates the aggregation process, resulting into an increase of scattering intensity in Guinier regime which in turn originates from the large aggregate structure evolved during the aggregation process.

The samples at low pH and 100 mM added NaCl (Fig. 7.4b) show similar behavior to 10 mM pH titration set. However, as pH is increased to 9 and beyond, SAXS profiles show significant difference from the aggregates at 10 mM NaCl. At 100 mM electrolyte concentration, instead of disappearance of the rise in low- q intensity, a steep increase in the slopes at higher salinity can be noticed. At 100 mM ionic strength, the slope of low- q intensity for $\text{pH} \approx 10$ varies as $q^{-3.5}$ compared to $q^{-1.5}$ for 10 mM sample at corresponding pH. Silica/lysozyme aggregates with no externally added salt redisperses itself at $\text{pH} > 9.8$, whereas, the flocs formed at 50 and 100 mM salt remain densely aggregated at the higher end of the experimental pH region (10.5). At pH 10.1 with 100 mM NaCl, the SAXS intensity profile at $q < 0.2 \text{ nm}^{-1}$ (Fig. 7.4b) indicates a decrease in the intensity slope in comparison to pH 9.9. This observation can be attributed to the fact that at this pH the mean aggregate size increases to an extent that a small fraction of the floc separates from the incident x-ray beam.

For accessing the finer details and quantitative information about the aggregation phenomena, structure factors ($S(q)$) for the samples at different salinities were extracted. Figure 7.5a shows the typical $S(q)$ obtained as a function of scattering vector q for different salt concentration (c_{NaCl}) at $\text{pH} \approx 10$. For better visualization, curves have been shifted upwards by the factor 1. The $S(q)$ obtained at all ionic strengths has the primary peak at $q = 0.35 \text{ nm}^{-1}$ and a secondary oscillation at $q = 0.65 \text{ nm}^{-1}$. Both the observed oscillations are well reproduced by *Sticky-Hard-Sphere* (SHS) model [24]. The lack of agreement between the experimental data and the fit for $q = 0.42\text{--}0.6 \text{ nm}^{-1}$ is due to the lack of precision in the determination of absolute value of polydispersity for bare silica nanoparticles [16]. It can be perceived from the plots that the absolute magnitude of the primary oscillation increases with increase in c_{NaCl} from 0 to 100 mM. The increase in the absolute magnitude of the primary oscillation corresponded to the higher coordination number of silica in the aggregate itself, thus compact aggregation. The number of nearest neighbors and particle density of an aggregate is related to overall attraction between two interacting bodies (silica spheres) by a parameter called stickiness ($1/\tau$). SHS model is congruent to the square-well potential model with the constraint that the well depth (u) tends to infinity and the well width (Δ) is significantly smaller than the diameter of the particle. $1/\tau$ obtained by fitting the structure factor of the SAXS measurements is related to u and Δ by the following equation

$$1/\tau = \left(\frac{12\Delta}{D + \Delta} \right) e^{u/kT} \quad (7.2)$$

where, D is the diameter of silica nanoparticles, k is the Boltzmann constant and T is the temperature. Figure 7.5b shows the variation of stickiness parameter obtained by the best fit to experimental $S(q)$ by SHS model. According to

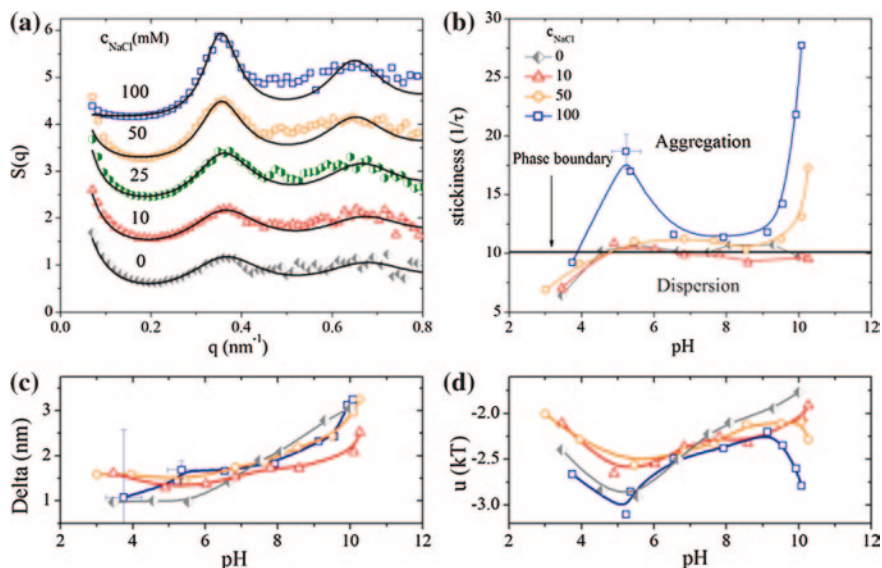


Fig. 7.5 **a** The structure factor $S(q)$ extracted from the scattering intensity profiles at pH 10 with 0–100 mM externally added NaCl. The *scattered points* are the extracted $S(q)$ and the *solid lines* are the best fits obtained by sticky-hard-sphere (SHS) at a given salt concentration. **b** Stickiness values (Eq. 7.2) obtained by fitting $S(q)$ by SHS model for pH titration with known amounts of added NaCl. The *horizontal line* marks the phase boundary predicted by SHS model. **c** and **d** are the well-width and the well-depth respectively for the SHS square-well inter-particle interaction potential for samples represented in (**b**)

the SHS model, the horizontal line drawn in the Fig. 7.5b is the phase boundary ($1/\tau = 10.2$) between single and dual phase regions, i.e. the samples with stickiness parameter below the phase boundary ($1/\tau < 10.2$) remain dispersed (stable), whereas for $1/\tau > 10.2$, they exist as suspended aggregates (unstable) [25]. Stickiness values obtained as the function of pH at different amounts of added salts are shown in Fig. 7.5b. Initial rise in stickiness with the increase in pH from 3 to 4 for all salinities can be observed. The stickiness of silica nanoparticles remains constant in the region pH 6–9 for low ionic strengths. These observations are in agreement with our previously reported stickiness ($1/\tau$) values [16] for silica/lysozyme aggregates in the absence of any externally added electrolyte. But for 100 mM sample there is a sudden increase in stickiness at $\text{pH} \approx 4$, with higher degree of silica aggregation at this pH. A pronounced salinity dependent aggregation was observed at $\text{pH} > 9$, and a rapid increase in the stickiness values was detected for high ionic strengths. The observed high stickiness values for 100 mM ionic strength are in agreement with the high turbidity observed for corresponding floccs. Figure 7.5c, d show the obtained values of u and Δ respectively. As can be observed from the plots, there is a gradual increase in Δ with the increase in pH regardless of the ionic strength of the dispersion. However, the magnitude of attractive interaction potential (u) shows larger values for aggregated samples than for the dispersed ones. The lysozyme induced attractive pair potential (u) for high

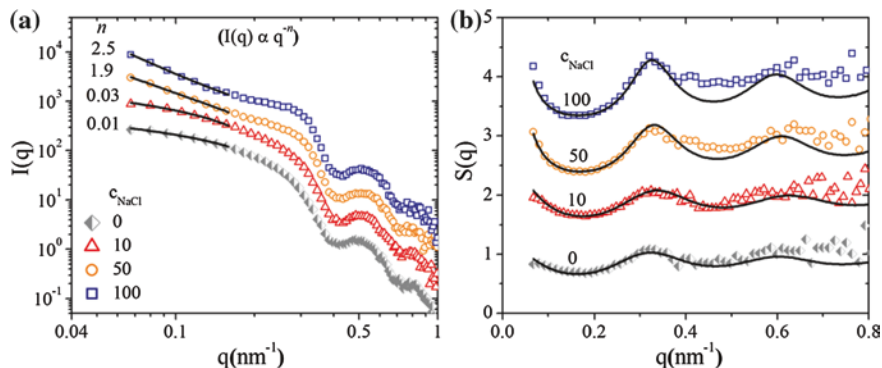


Fig. 7.6 **a** SAXS intensity $I(q)$ versus q profile is plotted on a log-log scale, for a silica dispersion having increasing salt concentration having same amount of protein ($y = 10$) at pH 8.3. Here the number shown next to the curves indicates slope of scattering intensity in the Guinier regime (low- q region) at four different salinities. **b** Extracted structure factor $S(q)$ from the intensity profiles in (a) and their corresponding fits according to SHS model

salinities are higher in magnitude in comparison to the samples at low salinities (at comparable pH), indicating that binding force between the silica particles is larger for higher salinities. In the acidic range (pH < 4) a significant amount of lysozyme remains in the unbound state (Fig. 7.2a) and hence protein mediated aggregation is less and the SHS is strictly not valid, which results into significant errors in the estimation of SHS model parameters.

7.2.3.4 Aggregation of Patchy Nano-Silica ($y = 10$)

Until this point, we have presented the effects of dispersion salinity at a fixed but relatively high surface loading of protein ($y = 40$) per silica particle. With the aim to study the effect of salt at low lysozyme concentration ($y = 10$), samples at pH 8.3 with 10–100 mM NaCl concentrations were prepared using organic buffer (bicine). The change in the aggregation behavior was monitored by SAXS. Fig. 7.6a, b present the SAXS profiles and thus extracted structure factors $S(q)$ for different salinities at pH 8.3. The numbers given next to the SAXS curves in Fig. 7.6a are the low- q (0.07–0.15 nm⁻¹) slopes (n) of scattering intensity, varying proportional to q^{-n} . As indicated by the values of n for $y = 10$, the magnitude of the slopes increased from $n \approx 0$ to 2.5, when the ionic strength was varied from 0 to 100 mM. As mentioned earlier, this increase in low- q intensity is the signature of the aggregation of scattering entities i.e. silica nanoparticles. Structure factors extracted from the scattering curves and their corresponding fits from SHS model are given in Fig. 7.5b. The fitting parameters obtained and the turbidity values for the aggregates are given in Table 7.3. Low turbidity values for the samples with 0 and 10 mM salt, indicate the absence of any observable aggregation of silica nanoparticles i.e. lysozyme is not able to glue the silica particles at $y = 10$ and at low

Table 7.3 Turbidity and $S(q)$ fit parameters stickiness ($1/\tau$), volume fraction (φ), well width (Δ), well depth (u) at surface concentration of 10 protein molecules per silica (γ) with increasing NaCl concentration c_{NaCl}

| c_{NaCl} | Turbidity | $1/\tau$ | φ | Δ | u |
|-------------------|-----------|----------|-----------|----------|------|
| 0 | 1 | 5.4 | 0.08 | 1.2 | -2.1 |
| 10 | 4 | 6.5 | 0.09 | 1.5 | -2.1 |
| 50 | 163 | 9.7 | 0.16 | 1.3 | -2.7 |
| 100 | 183 | 10.2 | 0.15 | 1.7 | -2.5 |

All measurements were carried out at 25 °C

ionic strengths and nanoparticles remain in dispersed form. As the ionic strength is raised to 50 and 100 mM the turbidity increases to 163 and 183 cm^2/g respectively. The increase in turbidity values is complemented by the high stickiness values given by SHS fit to the $S(q)$.

7.3 Discussion

As presented in the previous section, adsorption of lysozyme and the induced aggregation of silica nanoparticles is highly dependent on pH and the ionic strength of the dispersion. Here we account for the observed differences in adsorption and aggregation behaviour on the basis of the complex interactions between hydrophilic silica particles and lysozyme.

7.3.1 Role of Electrostatic Interactions

In our previous study of the interaction of silica nanoparticles with lysozyme we presented evidence for the important role of electrostatic interactions in this system, based on the pH dependence of the lysozyme adsorption at the silica particles and the lysozyme-induced flocculation [16]. Following up this work we have now focused on the combined influence of pH and salinity on the adsorption and aggregation behaviors. The screening of electrostatic interactions between all pairs of charged species, i.e., protein-silica, particle-particle and protein-protein, causes a decrease of the maximum protein adsorption at the silica particles (Fig. 7.1). The decrease in the surface crowding of protein molecules at the silica surface is an indication that the protein-particle attractive pair interactions, although screened, are still dominating over the protein-protein repulsive interaction. These results are in agreement with the previously reported reduction in lysozyme binding to silica nanoparticles [14, 15, 26]. Lundin et al. [17] have studied the adsorption of lysozyme at pH 8.5 on the flat silica surface by QCM and ellipsometry and have found a pronounced dependence of adsorption on the concentration of added salt. The generic behavior of the protein adsorption is the same with the decrease of

the bound protein by the factor of ≈ 1.3 from 10 \rightarrow 100 mM NaCl. However, the differences in the absolute amounts of bound protein can be attributed to the probable dissimilarity in the surface charge density between our aqueous silica nanoparticle dispersion and the flat surface used by Lundin et al.

7.3.2 Protein Induced Silica Aggregation

As shown in Fig. 7.2a, b, in the course of pH change the adsorption of protein is accompanied by aggregation of the silica particles. Although, the binding behavior of the protein to silica remains similar at different tested salinities, significant differences can be observed in the corresponding sample turbidities. The increase in the concentration of monovalent salt from 1 to 100 mM decreases the Debye length of colloidal silica from about 10 to about 1 nm. The Debye length determines the length scale at which electrostatic interactions between the silica nanoparticles are screened, and therefore is of immediate relevance for the structuring and stability of the dispersion [27]. For low dispersion salinities (large Debye lengths) the dispersion remains stable against aggregation due to electrostatic inter-particle repulsions. In the presence of lysozyme higher turbidity is solely due to the formation of protein-bridged-silica aggregates. In the absence of any externally added salt at $\text{pH} < 4$, the silica surface is weakly charged and proteins remains unadsorbed and hence the silica nanoparticles remain in completely dispersed form. At the intermediate pH regime, silica-lysozyme forms oppositely charged pair and form hetero-aggregates. Whereas, in the weak protein binding regime $\text{pH} 4\text{--}5$, SAXS structure factor fits show a high stickiness (Fig. 7.5b), which can be explained by the following two cooperative effects (i) lack of silica dispersion stability because of vicinity of its IEP and high ionic strength, [28] and (ii) effective gluing of silica nanoparticles by protein molecules. Too high value of stickiness parameter is obtained at 100 mM NaCl (Fig. 7.5b), which is due to the reduction in the screening length of the particles.

At intermediate $\text{pH} 5\text{--}9$, the aggregation is the typical hetero-aggregation between highly charged silica and lysozyme molecules, resulting into the formation of less dense flocculated networks [16]. The aggregation occurring in this pH range is independent of the dispersion salinity, the possible reason for this observation is discussed later in this section. For the $\text{pH} > 9$, the positive charge density on the lysozyme surface decreases because of its approaching IEP ($\text{pH} 11$) resulting in the weaker bridging capability of lysozyme and hence weaker aggregation. At this point we should also keep in mind that with the increase in salinity, there is an increase in the screening of charged entities i.e. the local charges both on lysozyme and silica. At $\text{pH} > 9$, at a known NaCl concentration, the surface charge of silica particles remains constant and highly negative [16]. The changes occurring in the silica/lysozyme composite system are solely because of the change in the surface charge density of the protein. As the IEP of lysozyme is approached, the charge on the surface of protein diminishes resulting into the release of bound counter ions (Cl^- from NaCl) on the surface. As a result, the surface of the protein is dehydrated

leading to the increase in attractive Hamaker dispersion forces (salting out). The aggregation of lysozyme itself has been reported earlier in various theoretical and experimental studies [29, 30]. In their work, Velev et al. [30] have found that for lysozyme increasing salt concentration results in the decrease in the second virial coefficient. The net positive charge on protein decreases with increasing pH and the repulsive-attractive interactions approach a balance at $\text{pH} \approx 9$ for lysozyme increasing the importance of van der Waals forces [30]. For our silica-lysozyme composite, on addition of monovalent 1:1 electrolyte (NaCl) the turbidity (Fig. 7.2b) as well as stickiness (Fig. 7.5b) show a sudden increase. Tentatively, we attribute the increase in turbidity at higher pH and salinity samples to the decrease in the Debye length of the silica dispersion and with the approaching IEP of lysozyme, the net charge on lysozyme approaches zero, but there exist local charges on the surface of proteins, which are further screened by high salt concentrations. Under these screened charge interactions, the hydrophobic groups on the surface of protein molecules tend to lose their water of hydration, in order to gain entropy in the form of released water molecules. Dehydration results in the exposure of hydrophobic surface patches of the protein to the solution which then tend to precipitate out by attaching to the protein molecule sitting on the surface of another silica nanoparticle. Hence, strong hydrophobic protein-protein interactions now drive aggregation phenomenon. This behavior is similar to the salting-out effect of only protein dispersions. In the present case, we can say that the salting-out phenomenon for protein is taking place which incorporates the silica nanoparticles into the phase separating domain. These effects get stronger with the increase in the NaCl concentration resulting in the increase in the mean aggregate size and decrease in the packing density of the floc (Fig. 7.3).

7.3.3 Lysozyme/Silica Patchy Particles

At low protein concentration, only a small fraction of the silica surface is occupied by the protein, i.e. the silica surface has only a handful patched of lysozyme adhering to the surface by electrostatic attraction. At this low surface coverage with protein the silica/protein dispersions showed a pronounced salinity-dependent aggregation. The volume fraction of silica in the floccs obtained by SHS model fitting shows an increase of around 80 % with the increase in c_{NaCl} from 0 to 100 mM (Fig. 7.6). The jump in the turbidity values for the aggregated solution at $y = 10$ was also observed (not shown) and was proportional to the concentrations of NaCl. Analytic centrifugation also shows an increase in aggregate size with salinity. This increase in the aggregation is again attributed to the collaborative function of suppression of silica-silica repulsions and increase in protein-protein hydrophobic attractions. The reason of the present effect gets pronounced only at low surface which is discussed here. High protein concentration at pH 8.3 results into a larger number of bridges between the silica particles resulting into a high aggregation in the system. However, when the protein concentration is sufficiently lower at the same pH, there are not enough number of lysozyme molecules available to form the junction between silica nanoparticles. The decrease in the Debye length by the adding salt results into a less repulsive

interaction between silica/protein patchy particle and now, in the screened interacting system smaller number of bonds are actually capable of gluing the silica particles together. Here we just presented the effects, more systematic studies are needed to quantify the results in terms of the minimum number of protein particles necessary to aggregate the silica dispersion at a given pH.

7.4 Conclusions

In this work we have demonstrated the importance of dispersion salinity and pH on the binding affinity of lysozyme to silica nanoparticles. Increase in ionic strength of dispersion at pH 8.3 results in a gradual decrease in the maximum surface excess of lysozyme adsorption onto silica nanoparticles. In the set of experiments at a constant ratio of silica and protein and fixed values of salinity we have studied the turbidity of the samples as a function of pH. These measurements show that an increase in salinity does not have a very pronounced effect on the turbidity for $\text{pH} < 9$, i.e., at pH values well below the isoelectric point of lysozyme. However, a further increase in the pH results in a very pronounced increase in turbidity, indicating a strong increase of the aggregate size. SAXS measurements show an increase of the scattering intensity in the low- q regime, indicating the presence of silica aggregates. From measured SAXS data, the structure factor of aggregates could be determined. As before, [16] we have analyzed the structure factor data on the basis of the sticky-hard sphere model. A strong increase in stickiness of the silica beads with increasing salinity was observed at $\text{pH} > 9$, in accordance with the high turbidity values in this regime. The high stickiness of the beads was attributed to the presence of dominant hydrophobic interactions between the protein molecules attached to different silica particles. Furthermore, we have found that salinity also changes the aggregation behavior of protein with the silica particles at very low protein loadings (10 lysozyme per silica). All the studies prove that salinity and pH play a major role in the lysozyme-induced aggregation of the silica particles. The interactions can be tuned by adjusting the charges on the individual particles by changing pH, and the charges can be screened by addition of salt to the dispersion. Above some limiting value of salinity the hydrophobic interactions between lysozyme molecules become a dominant factor. Hence, we conclude that depending upon the extent of surface charge screening, the aggregation behavior is governed either by the electrostatic interactions or by short-range hydrophobic interactions between the protein molecules.

References

1. Walkey CD, Chan WCW (2012) Understanding and controlling the interaction of nanomaterials with proteins in a physiological environment. *Chem Soc Rev* 41:2780
2. Niemeyer CM (2001) Nanoparticles, proteins, and nucleic acids: biotechnology meets materials science. *Angew Chem Int Ed* 40:4129

3. Cedervall T, Lynch I, Lindman S, Berggard T, Thulin E, Nilsson H, Dawson KA, Linse S (2007) Understanding the nanoparticle–protein corona using methods to quantify exchange rates and affinities of proteins for nanoparticles. *Proc Natl Acad Sci* 104:2050
4. Wu J, Silvent J, Coradin T, Aimé C (2012) Biochemical investigation of the formation of three-dimensional networks from DNA-grafted large silica particles. *Langmuir* 28:2156
5. Gao J, Gu H, Xu B (2009) Multifunctional magnetic nanoparticles: design, synthesis, and biomedical applications. *Acc Chem Res* 42:1097
6. Colvin VL, Kulinowski KM (2007) Nanoparticles as catalysts for protein fibrillation. *Proc Natl Acad Sci* 104:8679
7. Farokhzad OC, Langer R (2009) Impact of nanotechnology on drug delivery. *ACS Nano* 3:16
8. Shemetov AA, Nabiev I, Sukhanova A (2012) Molecular interaction of proteins and peptides with nanoparticles. *ACS Nano* 6:4585
9. Aubin-Tam M-E, Schifferli KH (2008) Structure and function of nanoparticle–protein conjugates. *Biomed Mater* 3:034001
10. Chen SH, Li FC, Souris JS, Yang CS, Tseng FG, Lee HS, Chen CT, Dong CY, Lo LW (2012) Visualizing dynamics of sub-hepatic distribution of nanoparticles using intravital multiphoton fluorescence microscopy. *ACS Nano* 6:4122
11. Lynch I, Salvati A, Kenneth DA (2009) Protein-nanoparticle interactions: What does the cell see? *Nat Nanotechnol* 4:546
12. Haynes CA, Norde W (1994) Globular proteins at solid/liquid interfaces. *Colloids Surf B* 2:517
13. Corbalan JJ, Medina C, Jacoby A, Malinski T, Radomski MW (2012) Amorphous silica nanoparticles aggregate human platelets: potential implications for vascular homeostasis. *Int J Nanomed* 7:631
14. Larsericsdotter H, Oscarsson S, Buijs J (2001) Thermodynamic analysis of proteins adsorbed on silica particles: electrostatic effects. *J Colloid Inter Sci* 237:98
15. Wong K, Cabane B, Somasudaran P (1988) Highly ordered microstructure of flocculated aggregates. *Colloids Surf* 30:355
16. Bharti B, Meissner J, Findenegg GH (2011) Aggregation of silica nanoparticles directed by adsorption of lysozyme. *Langmuir* 27:9823
17. Lundin M, Elofsson UM, Blomberg E, Rutland MW (2010) Adsorption of lysozyme, β -casein and their layer-by-layer formation on hydrophilic surfaces: effect of ionic strength. *Colloid Surf B* 77:1
18. Su TJ, Lu JR, Thomas RK, Cui ZF, Penfold J (1998) The adsorption of lysozyme at the silica–water interface: a neutron reflection study. *J Colloid Inter Sci* 203:419
19. Kumar S, Aswal VK, Kohlbrecher J (2011) SANS and UV–vis spectroscopy studies of resultant structure from lysozyme adsorption on silica nanoparticles. *Langmuir* 27:10167
20. Lerche D, Sobisch T (2007) Consolidation of concentrated dispersions of nano- and micro-particles determined by analytical centrifugation. *Powder Technol* 174:46
21. Sobisch T, Lerche D (2008) Thickener performance traced by multisample analytical centrifugation. *Colloids Surf A* 331:114
22. Detloff T, Sobisch T, Lerche D (2006) Particle size distribution by space or time dependent extinction profiles obtained by analytical centrifugation. *Part Part Syst Charact* 23:184
23. Sobisch T, Lerche D, Detloff T, Beiser M, Erk A (2006) Tracing the centrifugal separation of fine-particle slurries by analytical centrifugation. *Filtration* 6:313
24. Baxter RJ (1968) Percus–Yevick equation for hard spheres with surface adhesion. *J Chem Phys* 49:2770
25. Regnaut C, Ravey JC (1989) Application of the adhesive sphere model to the structure of colloidal suspensions. *J Chem Phys* 91:1211
26. Nezu T, Masuyama T, Sasaki K, Saitoh S, Taira M, Araki Y (2008) Effect of pH and addition of salt on the adsorption behavior of lysozyme on gold, silica, and titania surfaces observed by quartz crystal microbalance with dissipation monitoring. *Dent Mater J* 27:573

27. Zeng Y, Grander S, Oliveria CLP, Thünemann AF, Paris O, Pederson JS, Klapp SH, Klitzing RV (2011) Effect of particle size and Debye length on order parameters of colloidal silica suspensions under confinement. *Soft Matter* 7:10899
28. Metin CO, Lake LW, Miranda R, Nguyen PQ (2011) Aggregation kinetics and shear rheology of aqueous silica suspensions. *J Nanopart Res* 13:839
29. Lund M, Jungwirth P, Woodward CE (2008) Ion specific protein assembly and hydrophobic surface forces. *Phys Rev Lett* 100:258150
30. Velev OD, Kaler EW, Lenhoff AM (1998) Protein interactions in solution characterized by light and neutron scattering: comparison of lysozyme and chymotrypsinogen. *Biophys J* 75:2682

Chapter 8

Protein-Specific Effects of Binding to Silica Nanoparticles

8.1 Introduction

In the past decades, promising new applications of nanoscience in the biomedical field have emerged, including drug delivery, imaging and biosensing [1, 2]. Since a wide variety of materials have been considered for such applications, a basic understanding of their interactions with biomolecules is imperative. The interaction of proteins with hydrophobic or hydrophilic surfaces has been studied extensively in the past and giving evidence of the complexity of the phenomena involved [3–5]. Here we present some results of a comparative study of the interaction of two small globular proteins lysozyme and cytochrome C with silica nanoparticles of 22 nm diameter in an aqueous environment. The study focuses on the adsorption of proteins at the silica particles and the hetero-flocculation of the silica particles induced by the adsorption of the protein. Turbidity and Small Angle X-ray Scattering (SAXS) has been used for studying the hetero-aggregates formed in different pH regimes between the isoelectric point of the silica particles and of the protein.

8.2 Results

8.2.1 Characterization of Proteins

The globular proteins used in the present study belong to the class of hard proteins. They have similar molar mass, a similar radius of gyration [6, 7] and also a similar isoelectric point (IEP). However, the two proteins differ with regard to their surface charge distribution and, as a consequence, the magnitude of the permanent dipole moments of the two proteins is quite different, cytochrome C

Modified from the article: Bharti, B., Findenegg, G. H., *Chem. Lett.*, **2012**, *41*, 1122. Copyright 2012 The Chemical Society of Japan.

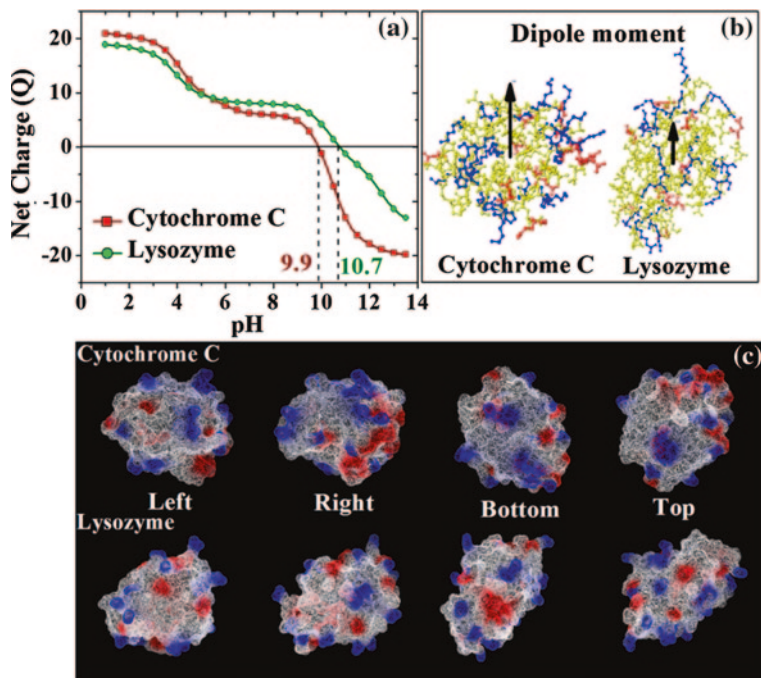


Fig. 8.1 Characterization of the proteins cytochrome C and lysozyme. **a** Calculated net charge per molecule (Q) as a function of pH; the *dotted lines* are inactive for IEP's for two proteins. **b** Structure of the two proteins (basic residues in *blue*, acidic residues in *red*, neutral residues in *yellow*); the *arrows* indicate the direction and magnitude of the net dipole moment of the molecules. **c** Four-sided schematic representation of the surface electrostatic potential of the two proteins (positive potential in *blue*, negative potential in *red*)

(185D) has a much higher value than lysozyme (94D) [8]. The net charge Q of the two proteins as a function of pH was calculated by Eq. 8.1, [9]

$$Q = \sum_A n_A \left(1 + 10^{-(\text{pH} - \text{p}K_a(A))}\right)^{-1} + \sum_B n_B \left(1 + 10^{-(\text{pH} - \text{p}K_a(B))}\right)^{-1} \quad (8.1)$$

where n_A and n_B represent the numbers of acidic and basic residues in the peptide chain, while $\text{p}K_a(A)$ and $\text{p}K_a(B)$ relate to the acid dissociation constants of the acidic and basic residues, respectively.

The resulting dependence of the net charge on pH is shown in Fig. 8.1a. It can be seen that the curves are quite similar in the acidic and neutral pH range, but at higher pH, the net charge of cytochrome C tends to negative values more steeply and has a somewhat lower IEP than lysozyme. Figure 8.1b shows the structure of two proteins along with the direction of the resulting dipole moment (vertical arrows) at neutral pH. Basic residues (+) are indicated in blue, acidic residues (−) in red, and neutral residues in yellow color. The structures and resulting dipole moment presented in Fig. 8.1b were obtained by using the protein data bank lysozyme (PDB: 2LYZ) and

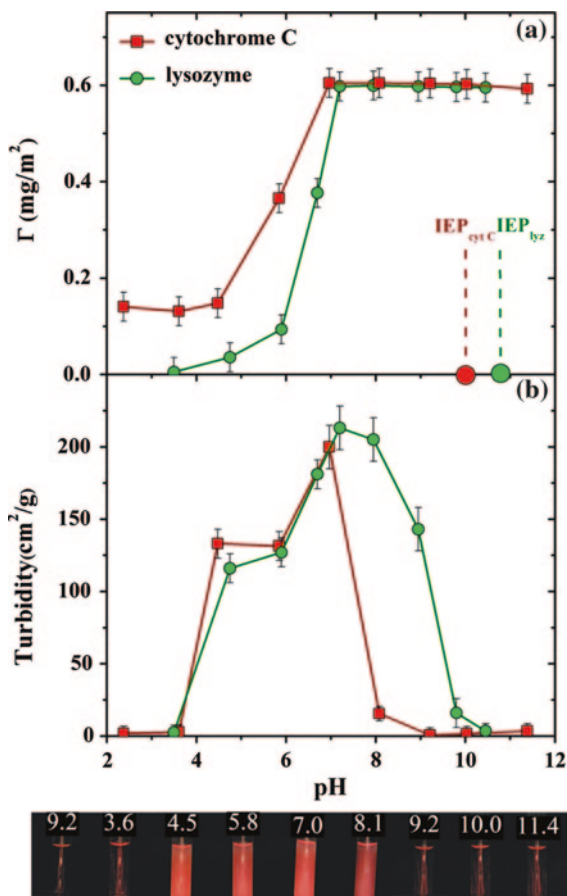
cytochrome C (PDB: 1HRC) structures. The calculations were done by online protein dipole moment server [10]. Only the non-hydrogen atoms of the standard amino acids of the protein itself were included in the dipole moment calculations. The exact electrostatic potentials and its distribution at the surfaces of the two proteins as calculated by the CCP4MG [11] software package are shown in Fig. 8.1c. The images show the four faces of the protein corresponding to a rotation of the molecule in steps of 90° as indicated in the figure. For lysozyme molecule, the partial areas of positive and negative potential are similar on the four faces, a more dissimilar distribution is observed for cytochrome C, in agreement with the higher dipole moment of the cytochrome C. We have studied the effect of this difference in charge distribution on the adsorption of the proteins at silica nanoparticles and the protein-induced flocculation of the silica.

Silica nanoparticles used in this study were synthesized by the method of Davis et al. [12], using lysine as the basic catalyst for the hydrolysis of the silica precursor, and characterized by SAXS and nitrogen adsorption. They had a mean diameter of 22 nm (polydispersity 10 %), a specific surface area of $180 \text{ m}^2/\text{g}$, and an isoelectric point near 3 (somewhat higher than the pure silica surface, presumably due to the adsorption of lysine [13]). Accordingly, in a wide pH range between the isoelectric points of silica and the protein, the silica particles are negatively charged while the protein molecules carry a positive net charge. As was shown earlier for the case of lysozyme, this opposite charge dominates the adsorption behavior of the protein and the hetero-flocculation behavior of the silica nanoparticles [14].

8.2.2 Protein-Binding to Silica Surface

In order to investigate the effects of dissimilar dipole moment of two proteins, pH titrations experiments were carried out for protein/silica dispersions of fixed concentration of silica (1 wt%) and protein (1 mg/mL, corresponding to a surface concentration of $0.6 \text{ mg}/\text{m}^2$ in the complete adsorption regime). Details of the experiments are given elsewhere [14]. A comparison of the results obtained for the two proteins under these experimental conditions is shown in Fig. 8.2. In both cases the fraction of adsorbed protein increases with pH and reaches a plateau, corresponding to (almost) complete adsorption at about pH 7 (Fig. 8.2a). At pH 4 and below we find effectively no adsorption of lysozyme, but a nonzero and pH independent level of adsorption of cytochrome C. Over a wide pH regime the observed adsorption behavior of the proteins can be rationalized by a dominant role of attractive electrostatic interactions between the negative silica surface and the positively charged protein molecules, as discussed in the previous work [14]. The persistence of high adsorption level near the IEP of the proteins can be attributed to the interaction of remaining positively charged patches of the protein surface with the strongly negative silica surface, and the diminished electrostatic repulsion between adsorbed protein molecules and increasing role of hydrophobic interactions between adsorbed protein.

Fig. 8.2 Behavior of the proteins, lysozyme and cytochrome C with silica nanoparticles. **a** The amount of protein bound in mg/m^2 of silica surface as the function of solution pH. **b** Turbidity of silica dispersion containing fixed amount of protein over a wide pH range. Also shown is the photograph of the silica/cytochrome C binary dispersion at different pH values (indicated *above* each sample)



8.2.2.1 Protein-Induced Silica Aggregation

The turbidity of the protein/silica dispersions and its dependence on pH (Fig. 8.2b) can be attributed to silica aggregation due to adsorbed protein. At pH 3 when little or no protein is adsorbed, only weak aggregation of the silica particle occurs due to the missing charge stabilization. The sharp increase in turbidity from pH 3 to 4 and the further increase up to pH 7 is attributed to the protein mediated bridging of silica nanoparticles [14]. The low turbidity of the systems in the pH region near the IEP of the protein can be attributed to charge stabilization of the strongly negatively charged silica particles coated with a layer of nearly uncharged protein. Interestingly, significant differences in the pH-dependence of the turbidity are found in the pH range 7–10. For the dispersion with cytochrome C, the strong decrease in turbidity occurs at a significantly lower pH than for the dispersion with lysozyme. This shows that cytochrome C although being strongly adsorbed as lysozyme has a significantly lower ability to induce aggregation of the silica particles in this pH regime. It is also of interest to note that at low pH some cytochrome C remains adsorbed at the

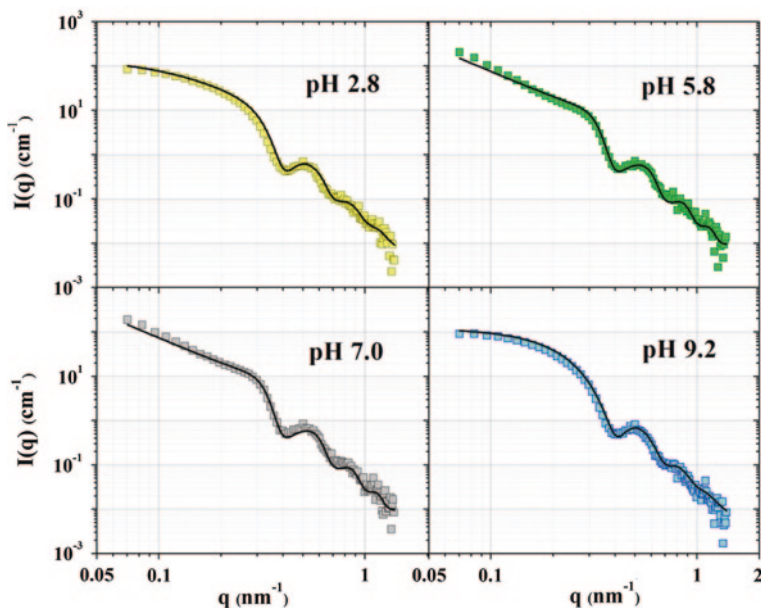


Fig. 8.3 SAXS profiles for silica dispersion (1 wt%) with cytochrome C (1.0 mg/mL) at different pH values. Experimental data and fits with the sticky hard sphere structure factor

silica particles but here too this does not lead to enhanced aggregation of the silica nanoparticles. We return to this point later.

The aggregate structure of the silica hetero-flocculate with cytochrome C was characterized by SAXS. Figure 8.3 shows SAXS profile where the radially averaged scattering intensity, $I(q)$ is plotted as a function of momentum transfer q . It needs to be kept in mind that the proteins due to their low electron density remain effectively invisible to the X-ray beam. The profiles were obtained for a 1 wt% silica dispersion containing on average 50 cytochrome C molecules per silica particle. The profiles for pH 5.8 and 7.0 exhibit a pronounced increase in $I(q)$ in the low- q region (Guinier regime), which is missing or much weaker in the profiles for pH 9.2 and 2.8. The increase in scattering intensity in the Guinier regime is a signature of strong particle aggregation [15, 16]. The scattering profiles were analyzed in terms of the relation

$$I(q) = N\Delta\rho^2 P(q)S(q) \quad (8.2)$$

where N represents the number density of the scattering particles, $\Delta\rho$ their scattering contrast against the aqueous phase, $P(q)$ the form factor of the particles, and $S(q)$ the inter-particle structure factor. The form factor of the silica nanoparticles was determined from a dilute dispersion of the plain particles without protein and was then used in the evaluation of the structure factor. The structure factor data were analysed with the sticky hard sphere (SHS) model [17, 18] which is based on a square-well pair potential in the limit of large well

Table 8.1 Stickiness parameter characterizing the interaction of silica nanoparticles in the presence of a proteins in a wide range of pH

| S No. | Cytochrome C | | Lysozyme | |
|-------|--------------|------------|----------|------------|
| | pH | Stickiness | pH | Stickiness |
| 1 | 3.6 | 6.6 | 3.5 | 8.5 |
| 2 | 4.5 | 10.3 | 4.7 | 10.1 |
| 3 | 5.8 | 10.3 | 5.9 | 10.3 |
| 4 | 7.0 | 10.3 | 7.2 | 10.4 |
| 5 | 8.1 | 10.1 | 8.9 | 10.5 |
| 6 | 9.2 | 0.2 | 9.8 | 11.0 |
| 7 | 10.0 | 0.2 | 10.4 | 4.6 |

depth and small well width. Fitting the scattering curves to the SHS model with the form factor of polydisperse spheres yields the stickiness parameter expressed as

$$\tau = \left(\frac{1}{12\varepsilon} \right) \exp \left(-\frac{u}{kT} \right); \quad \varepsilon = \frac{\Delta}{\sigma + \Delta} \quad (8.3)$$

where σ is the silica hard sphere radius, Δ is the width of square-well potential, $1/\tau$ is the stickiness of the protein decorated silica bead, k is the Boltzmann constant, T is the temperature and u is the well depth of the pair potential. The solid lines in Fig. 8.3 represent the fit of the SHS model (with the form factor of silica) to the experimental data. The resulting values of the stickiness parameter of the silica particles in the presence of protein are given in Table 8.1. According to the SHS model, a system of sticky hard spheres will separate in a dilute and a dense phase when the stickiness parameter exceeds a value of about 10. We find that in the present case, the condition is satisfied by the dispersions in a pH range from 4 to 8 (for cytochrome C) and from 4 to 10 (for lysozyme), i.e. in the given pH ranges the silica particles are forming large floccs, in agreement with the results of turbidity measurements.

8.3 Discussion

Turbidity and SAXS measurements are both highlighting the similarities and differences in the aggregation behavior of silica nanoparticles in the presence of cytochrome C and lysozyme. In the pH range 4–7, the two proteins behave similar by inducing strong hetero-aggregation with the negatively charged silica nanoparticles (Figs. 8.2b and 8.3). At high pH (above the IEP of the protein), absence of aggregation can be attributed to a low bridging ability of the (net uncharged) protein and the concomitant increase of the repulsive electrostatic interaction between the protein-decorated silica. Since the IEP of the two proteins differs by less than 1 pH unit, one would expect that dispersions with the two proteins behave similar up to nearly the IEP of cytochrome C. However, redispersion of the system with cytochrome C has already occurred below

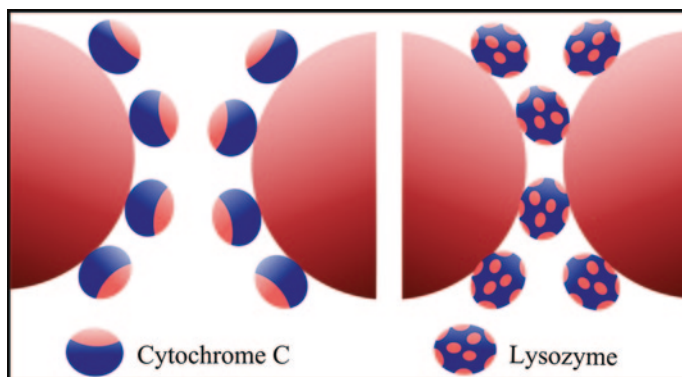


Fig. 8.4 Schematic representation of the proposed mode of adsorption of lysozyme and cytochrome C (*small ellipsoids*) on silica particles (*big hemi-spheres*). Positive and negative surface patches of the protein are indicated by *blue* and *red* color, respectively

pH 8.0, as is to be seen from Figs. 8.2b and 8.3. This shift in the redispersing pH value is one of the remarkable findings of this work and indicates that the high dipole moment, resulting from the non-uniformity of surface charge distribution on cytochrome C may play a vital role in the aggregation process. Whereas for lysozyme, the patches of positive and negative charge are distributed more or less uniformly on its surface (low dipole moment), the higher dipole moment of cytochrome C implies a bipolar distribution of the charge. Hence there will be a tendency for the cytochrome C molecules to adsorb in an orientation with the positive charge pointing toward the negatively charged silica surface and the negative charge pointing outwards (Fig. 8.4).

In this orientation the protein molecules have lost their ability to bridge two negatively charged silica particles. This effect may explain the lack of hetero-aggregation for cytochrome C at pH 8 and greater. The effect becomes relevant only in the regime close to the IEP and can be attributed to the fact that, at lower pH, the positive net charge density of the protein becomes higher and attractive bridging of the negatively charged silica particle can occur in many orientations of the adsorbed protein. Another interesting point concerns the difference in adsorption affinity of the two proteins at the silica particles at pH < 6 (Fig. 8.2b). For lysozyme the fraction of adsorbed protein falls off steeply below pH 7 and no adsorption is detectable below pH 3. This is strong evidence that electrostatic interactions between oppositely charged particles represent the main driving force of adsorption. For cytochrome C, on the other hand, a certain level of adsorption prevails down to the lowest experimental pH, where the silica surface is uncharged or even positively charged. Hence, non-electrostatic interactions must play a role in the adsorption of cytochrome C to the silica nanoparticles in this acidic pH regime. However, the silica aggregation is still governed by the electrostatic effects of the hetero-aggregating system.

8.4 Conclusions

In summary, these findings indicate that the adsorption behavior of lysozyme on the silica particles is dominated by electrostatic interactions while for cytochrome C non-coulombic contributions (presumably hydrophobic interactions) also play a role. In the hetero-aggregation of silica with proteins, it is the distribution of positively and negatively charged patches over the surface of the protein that tunes the aggregation behavior. Because of the bipolar distribution of surface charge at cytochrome C, this molecule is less effective to induce hetero-aggregation with silica particles in the pH regime approaching the IEP of the protein.

References

1. Farokhzad OC, Langer R (2009) Impact of nanotechnology on drug delivery. *ACS Nano* 3:16
2. Asuri P, Bale BSS, Karajanagi SS, Kane RS (2006) The protein–nanomaterial interface. *Curr Opin Biotechnol* 17:562
3. Lynch I, Dawson KA (2008) Protein-nanoparticle interactions. *Nanotoday* 3:40
4. Klein J (2007) Probing the interactions of proteins and nanoparticles. *Proc Natl Acad Sci USA* 104:2029
5. Li N, Zeng S, He L, Zhong W (2010) Probing nanoparticle-protein interaction by capillary electrophoresis. *Anal Chem* 82:7460
6. Parmar AS, Muschol M (2009) Hydration and hydrodynamic interactions of lysozyme: effects of chaotropic versus kosmotropic ions. *Biophys J* 97:590
7. Morar AS, Olteanu A, Young GB, Pielak GJ (2001) Solvent-induced collapse of α -synuclein and acid-denatured cytochrome c. *Protein Sci* 10:2195
8. Takashima S (2002) Electric dipole moments of globular proteins: measurement and calculation with NMR and X-ray databases. *J Non-Cryst Solids* 305:303
9. Posse E, Vitals AL, de Arcuri BF, Farias RN, Morero RD (1990) Lysozyme induced fusion of negatively charged phospholipid vesicles. *Biochim Biophys Acta* 1024:390
10. <http://bioinfo.weizmann.ac.il/dipol/>
11. McNicholas S, Potterton E, Wilson KS, Noble MEM (2011) Presenting your structures: the CCP4mg molecular-graphics software. *Acta Cryst D* 67:386
12. Davis TM, Snyder MA, Krohn JE, Tsapatsis M (2006) Nanoparticles in lysine-silica sols. *Chem Mater* 18:5814
13. Bharti B, Meissner J, Gasser U, Findenegg GH (2012) Surfactant adsorption and aggregate structure at silica nanoparticles: effects of particle size and surface modification. *Soft Matter* 8:2573
14. Bharti B, Meissner J, Findenegg GH (2011) Aggregation of silica nanoparticles directed by adsorption of lysozyme. *Langmuir* 27:9823
15. Muratov A, Moussaid A, Narayanan T, Kats EI (2009) A Percus–Yevick description of the microstructure of short-range interacting metastable colloidal suspensions. *J Chem Phys* 131:054902
16. Parneix C, Persello J, Schweins R, Cabane B (2009) How do colloidal aggregates yield to compressive stress? *Langmuir* 25:4692
17. Baxter RJ (1968) Percus–Yevick equation for hard spheres with surface adhesion. *J Chem Phys* 49:2770
18. Regnaut C, Ravey JC (1989) Application of the adhesive sphere model to the structure of colloidal suspensions. *J Chem Phys* 91:1211

Part IV

Field Directed Assembly of Hetero-Aggregating Microparticles

Part IV of the thesis reports the formation of permanent long chains made up of positively and negatively charged latex particles. In Chap. 9 we demonstrate how the heteroaggregation phenomenon and DEP can be combined to assemble permanent linear structures. We provide a complete characterization of the chains formed for two different particle size ratios and different number of ratios of the positive and negative particles. We also present an analysis of the data according to a new statistical model.

Chapter 9

Permanent Supracolloidal Biparticle Assembly Triggered by an Electric Field

9.1 Introduction

The colloidal assembly is a major route to making materials with tailored functionality resulting from the organization of the particles [1–3]. While much attention has been focused on colloidal crystals with potential photonics applications [4], permanently bound linear structures are a somewhat overlooked material with a broad range of applications. For example, linear arrays of magnetic nanoparticles can be used as flexible artificial flagellum [5], whereas linear chains of polystyrene nanoparticles in polymer solution can cause interesting viscosity anomalies [6]. In addition, the linear arrays of colloidal particles could find applications in structures for single-nanowire light emitting diodes [7], single electron transistors [8] and in microfluidics [9]. Colloidal assembly can be achieved by internal fields (induced by surfactants [10] and by dynamic self-assembly [11]) or by applying an external field (e.g., magnetic [12], or electric [13], or light [14]). DEP induces a long-range dipolar interaction between randomly distributed particles [10, 15, 16] which forces them to align into long chains along the direction of the applied field [17]. This effect has been used for one-dimensional [18] or two-dimensional [19] assembly, as well as for particle (or cell) capturing [20]. However, DEP-induced structures formed from a single type of particles will disassemble by thermal motion as soon as the field is switched off, due to the repulsive interaction caused by the surface charges.

We report here a facile, in-situ single-step, method of assembling permanent chains of micron-sized particles by applying AC electric fields to dispersions containing positive and negative particles. In contrast to biparticle assembly into crystalline arrays [21, 22], where the charge on the particles has to be tuned to low values to avoid irreversible aggregation, we use highly charged particles of opposite charge, with attractive interaction energies well in excess of the thermal energy, so that the particles stick irreversibly when they come in contact. The

Modified from the article: Bharti, B., Findenegg, G. H., Velev, O. D., *Sci. Rep.*, **2012**, 2, 1004. Copyright 2012 Nature Publishing Group.

hetero-aggregation between positive and negative particles in water is governed by short range attractive electrostatic interactions [23, 24]. The aggregation kinetics are commonly driven by Brownian dynamics and result in disordered, fractal like clumps of particles. The added deployment of an external electric field enables us to align the particles to chains by the long-range induced polarization interaction. By combining the hetero-aggregation with DEP we achieve the formation of linear structures of unprecedented length and order. We characterize the permanent chaining tendency of biparticle systems composed of particles of equal size as well as different sizes, we propose an explanation for the pronounced effects of different particle size and number ratio of the particles, and formulate assembly rules for tailoring the length of permanent chains formed.

9.2 Methods

The polystyrene particles used in this study were washed with milli-Q water several times in order to minimize the ionic strength of the dispersion and to avoid any trace of surfactant. pH of the dispersions was adjusted to 3.0 using 0.01 M HCl. The biparticle dispersion was prepared by mixing pre-sonicated aliquots of the constituent single-particle dispersions in a vial; it was then rapidly transferred into the hydrophobically sealed chamber (<10 s) and the electric field was employed instantaneously. The particle dispersion was subjected to a square wave AC electric field (40 V/mm, 10 kHz), using parallel electrodes. The assembly process of colloidal particles was observed using an Olympus BX-61 microscope both in bright-field and fluorescence mode. Several images of the linear chain structures were taken for further analysis. The chain length of a linear aggregate was defined by counting the number of constituent particles of a given chain. The chain length distribution was determined by analyzing at least 5 microscope images for given values of $D_{\text{small}}/D_{\text{large}}$ and r .

9.3 Results and Discussion

The on-chip setup used for assembling microparticles in the presence of electric field is shown in Fig. 9.1a. It consists of coplanar gold electrodes 2 mm apart connected to a function generator and an amplifier. The water-borne biparticle dispersion is placed in a microchamber (of thickness 100 μm) over the electrodes. The assembly patterns of two pairs of latex microparticles of opposite surface charge were investigated by bright-field and fluorescence microscopy. Their sizes, surface functional groups, fluorescence absorption and emission, and zeta potential (at pH 3) are given in Table 9.1. The charge of the particles at a particular pH is dependent on the nature of their surface functional groups. The zeta potential (ζ) provided in Table 9.1 is a proxy of the charge on the aqueous latex colloid's surface.

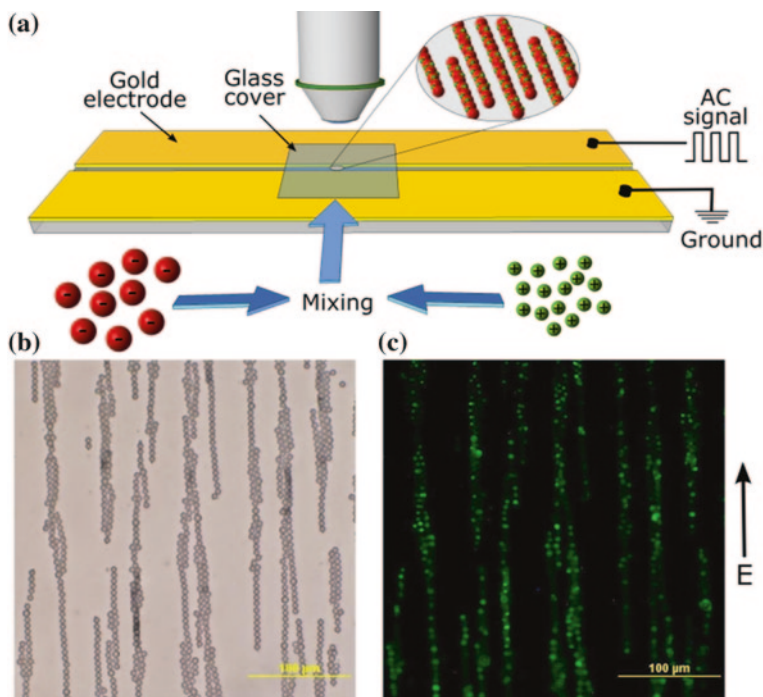


Fig. 9.1 Experimental setup and microscope images of assembled arrays. **a** Schematic representation of the setup used in the DEP experiments; **b** bright-field image of composite structures formed between 4 μm and 0.9 μm latex particles of system 2 (Table 9.1) upon application of a 45 V, 10 kHz AC electric field; **c** the same composite structures viewed in the fluorescence mode, showing the location of 0.9 μm particles (*green*) in the assembled structures

Table 9.1 Physical and surface chemical properties of the latex particles used in the study

| System | Diameter (μm) | Surface groups | ζ at pH 3 (mV) | Fluorescence (λ_{ab} , λ_{em}) |
|----------|----------------------------|----------------------------|----------------------|--|
| System 1 | A 2.0 | Sulfate ($-\text{SO}_4$) | -40 | (660 nm, 690 nm)-red |
| | B 2.2 | Amidine ($=\text{NR}$) | +50 | (494 nm, 521 nm)-green |
| System 2 | A 4.0 | Sulfate ($-\text{SO}_4$) | -35 | Insensitive |
| | B 0.9 | Amine ($-\text{NH}_2$) | +10 | (494 nm, 521 nm)-green |

The particle suspensions were mixed rapidly and immediately subjected to the unidirectional electric field, leading to induced dipole chaining. Figure 9.1b, c show the bright field and fluorescence images of long chains formed from the mixture of 4 μm and 0.9 μm latexes in the presence of a field. While the 4 μm latex particles were not fluorescent, the 0.9 μm particles appeared green when observed in fluorescence mode of the microscope. Some rearrangements in the linear directional structures were observed with the removal of AC-field after its initial application for 1 min. However, the structures didn't disintegrate completely, but a fraction of particles remained glued as chains of specific lengths.

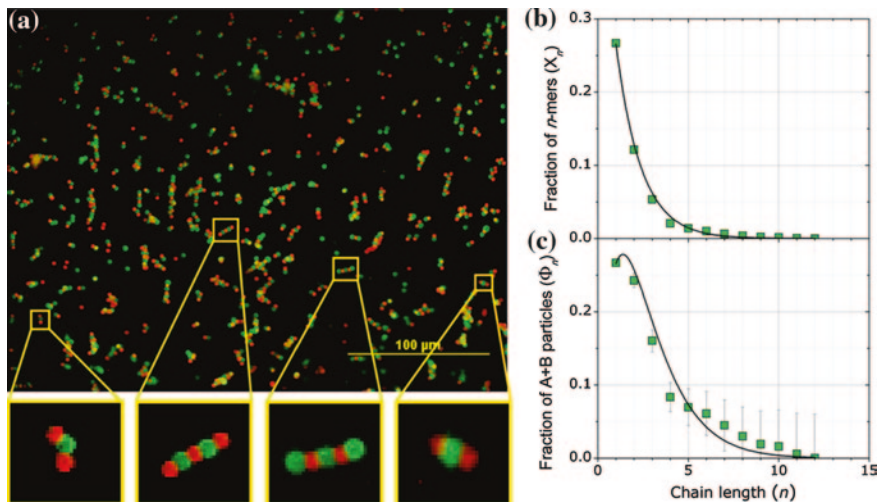


Fig. 9.2 Microscope images and chain length distribution for System 1 ($D_{\text{small}}/D_{\text{large}} = 0.91$). **a** Fluorescence images of the permanent structures formed by initial application of DEP field on the suspension containing $2.2 \mu\text{m}$ positive latex (green) and $2.0 \mu\text{m}$ negative latex (red) particles at $r = 1$; insets show specific aggregates at higher magnification. **b** Fractions of n -mer aggregates X_n as a function of n . **c** The same results expressed by the fractions of particles existing in form of n -mers, Φ_n . In (b) and (c) the points represent the experimental data, the lines represent the statistical model fit. In (b) the error bars are no larger than the symbols

We measured the distribution of chain lengths as a function of two parameters, viz., the particle size ratio, $D_{\text{small}}/D_{\text{large}}$, and the particle number ratio $r = N_{\text{small}}/N_{\text{large}}$. Examples of permanent structures formed in System 1 ($D_{\text{small}}/D_{\text{large}} = 0.91$) for equal numbers of positive and negative particles ($r = 1$) are shown in the fluorescence microscope images in Fig. 9.2. Since the long-range drag experienced by the particles in the electric field is dependent of the particle size ($F_{\text{DEP}} \simeq D^3$) [25] and the size of positive and negative particles is similar, all particles experience nearly the same DEP force and could be dragged with equal probability into any position in the chains. Accordingly, we observed a random sequence of negative (A-type) and positive (B-type) particles in these chains. When the field was switched off, contacts between equally charged (repelling) neighboring particles (A–A and B–B) disintegrated. Accordingly, the predominantly observed entities were monomers and short linear aggregates (chains) of alternating positive (green) and negative (red) particles. Results of a quantitative analysis of aggregate sizes are also shown in Fig. 9.2, where $X_n = N_n / (N_A + N_B)$ represents the number of linear clusters consisting of n particles, normalized to the total number of A and B particles (Fig. 9.2b), and $\Phi_n = nX_n$ gives the fraction of A and B particles contained in aggregates of length n (Fig. 9.2c). Experiments with an excess of either types of particles ($r \neq 1$) yield assemblies with even shorter chain lengths (not shown).

In System 2 ($D_{\text{small}}/D_{\text{large}} = 0.225$) the larger particles are of nearly two orders of magnitude greater volume than that of the small ones. Hence a much greater DEP force is exerted on the large particles in the electric field and only these

(A-type) particles participate in the rapid primary field-induced chain formation step. In a slower secondary process, the small (B-type) particles are captured, predominantly into the contact regions between large particles because of the high field intensity in those regions. This observation is in correlation with the results of Gupta et al. [26] on DEP chaining of yeast cells in the presence of (smaller) latex particles. Because in the present case A and B type particles carry opposite charges, the small particles trapped in the junctions can form a link between neighboring large particles. Accordingly, when the field is switched off the chain will break only at A–A contacts where no B particle was captured at the junction points.

DEP co-assembly in System 2 was studied for particle number ratios $r = N_B/N_A$ ranging from 1 to 24. The results of the chain length analysis are presented in Fig. 9.3. For this System we define chain length n as the number of large (A type) particles in the aggregates, and the respective number of chains, N_n , is normalized as $X_n = N_n/N_A$. The microscope images for $r = 1, 2.5, 12$ and 24 (Fig. 9.3a–d) indicate that, on average, longer chains are formed when a higher excess of B particles was present. This is most pronounced for the highest number ratio ($r = 24$) for which a distribution including very long chains was found, with some chains extending over the entire length of the microscope image. Closer inspection of the enlarged bright-field images (insets Fig. 9.3) of individual permanent chains and the respective fluorescence images (where only the small B particles are visible) indicates that several small particles may be captured in the gap between two large particles. The images also reveal that not all B particles are captured but some remain free, especially in samples with a high excess of B particles.

The trends in chain length distribution observed in the two systems can be explained by a combinatorial probabilistic model. For system 1 ($D_{\text{small}}/D_{\text{large}} = 0.91$), in the processes of random chain formation of A and B particles the probability of finding a chain of n particles in alternating sequence of A and B depends on the number fractions x and $1 - x$ and is proportional to $x^m(1 - x)^{n-m}$, where $m = (n \pm 1)/2$ (for $n = 1, 3, 5, \dots$) and $m = n/2$ (for $n = 2, 4, \dots$). For a stoichiometric composition of A and B particles ($x = \frac{1}{2}$) this combinatorial mathematics approach yields normalized numbers of n -mer chains as

$$X_n \equiv \frac{N_n}{N_A + N_B} = \frac{1}{2} \left(\frac{1}{2} \right)^n \quad (9.1)$$

and fraction of particles in n -mer chains $\Phi_n = nX_n$, is in fair agreement with the experimental findings (Fig. 9.2b, c). When the particle number ratio r in Eq. 9.1 was treated as an adjustable parameter, the best fit of the experimental X_n data was obtained for $r_{\text{eff}} = 0.93$. This deviation is within the error limits of the image analysis. From Eq. 9.1 the mean chain length for this number ratio is $\bar{n} = 2.3$.

To model the assembly process and the resulting chain length distribution for System 2 ($D_{\text{small}}/D_{\text{large}} = 0.225$), we evaluate the probability that a smaller particle of opposite charge will be captured in the junction between the large particles and serve as a “link” for the chain will depend on the ratio r . The model is based on the assumption that each contact point in the chain of large particles (A) formed in the primary DEP process serves as a binding site for the positively charged small particles

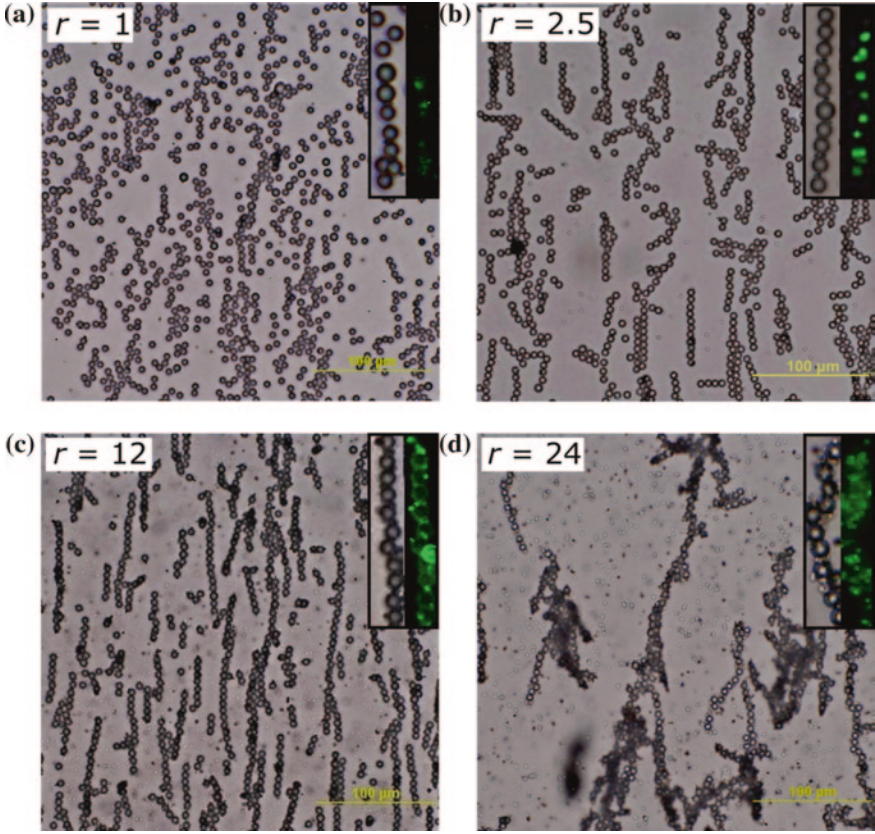


Fig. 9.3 Microscope images for System 2 ($D_{\text{small}}/D_{\text{large}} = 0.225$). **a–d** Bright-field microscope images of permanent structures for $r = 1, 2.5, 12$ and 24 , respectively. The insets are the magnified images of chain structures in bright field and fluorescence mode, indicating the location of the binding sites of small particles in the aggregates. The chain length increases with r and chains longer than the length of the microscope field of imaging were obtained at $r = 24$

(B), which form the permanent bond between the two A particles. If $S - S_0$ out of the S binding sites in the primary chain of A particles are occupied by B particles and S_0 sites remain vacant, the primary chain will break up into $S_0 + 1$ fragments when the field is switched off. The resulting distribution of fragment chain lengths X_n can be expressed generally by the fraction of vacant sites in the primary chain, S_0/S . To account for the observation that more than one B particle can be accommodated per binding site, we adapted a model of sequential binding equilibria that relates the fractions of binding sites occupied by $m - 1$ and m particles. This leads to the following distribution function

$$X_n \equiv \frac{N_n}{N_A} = \left(\frac{1}{r+1} \right)^2 \left(\frac{r}{r+1} \right)^{n-1} \quad (9.2)$$

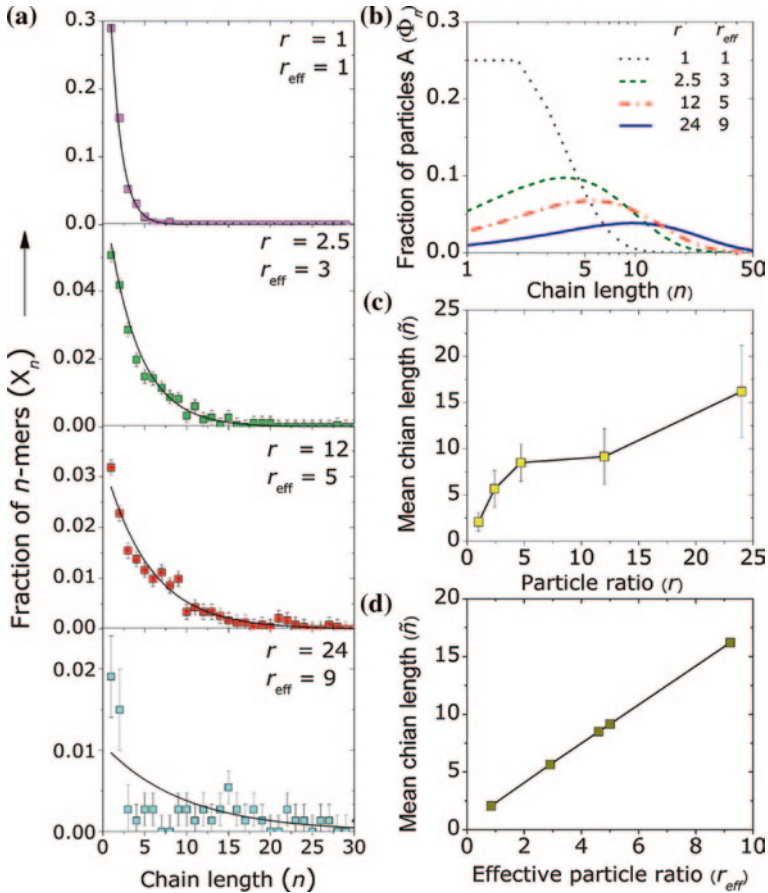


Fig. 9.4 Chain length distributions for system 2 ($D_{small}/D_{large} = 0.225$). **a** Fraction of n -mers or particle number fraction X_n of chain aggregates containing n large particles as a function of n for different r . The points represent the experimental data as derived from the bright-field images, the solid lines show fits by the proposed model, the values of r and r_{eff} given in the plots represent the experimental and the model best-fit particle ratio. **b** Fraction of A-type particles Φ_n that exists in form of n -mer chains. The values of r and corresponding r_{eff} are given in the plot. The figure illustrates the pronounced shift in the distribution to larger n values as the particle number ratio r_{eff} increases. **c** Mean chain lengths \bar{n} plotted as the function of the experimental particle number ratio r . **d** Mean chain length as a function of the effective particle number ratio r_{eff}

(see Sect. 3.2.3.2). When comparing the predicted chain length distribution with the experimental findings one has to take into account that not all B particles are incorporated in the chains. We used Eq. 9.2 to determine the effective particle ratio r_{eff} in the chains from the experimental chain length distribution. With these effective r values, Eq. 9.2 gives a good representation of the experimental chain length distribution X_n for particle number ratios up to $r = 12$, as shown in Fig. 9.4a.

At higher number ratios the data analysis is unreliable because the resulting assemblies are just a few chains extending over the whole length of the microscope field. Figure 9.4b illustrates the effect of increasing particle number ratio r on the fraction of A particles contained in chains of n segments, $\Phi_n = nX_n$. For equal numbers of A and B particles and for moderate excess of B ($r = 2.5$) we find that r_{eff} is close to or even somewhat less than the experimental r . For a larger excess of B, however, r_{eff} becomes much smaller than r , indicating that a decreasing fraction of B particles is incorporated in the chains (less than 50 % for $r = 24$). The increase of the mean chain length \bar{n} with the effective particle number ratio is shown in Fig. 9.4c. Interestingly, we find a linear increase of \bar{n} with r_{eff} (Fig. 9.4d).

The above results are unusual in the use of combinatorial mathematics and reaction kinetics rules to predict results of particle structuring in external fields. Two important assembly rules emerge on this basis: Permanent chains of significant length are obtained only if (1) the positive and negative particles have different sizes; (2) the small particles have to be present in excess. The importance of using particles of different sizes is underscored by the fact that for equally sized particles an excess of positive or negative particles leads not to an increase but a *decrease* of the mean chain length. In both cases, however, the opposite charge of the two types of particles leads to the formation of permanent chains. In this respect our work differs from earlier studies of particle pattern formation in AC electric fields, including the work on sterically stabilized binary suspensions of oppositely charged microparticles by Vissers et al. [27] in which the lanes formed upon the application of external field were temporary and disappeared on removing the electric field.

The present findings open up a new field of studies in AC-field induced supracolloidal permanent assembly. They show a promising way of directed assembly of permanent structures organized on large scales in a single-step, rapid and controllable manner. The statistical interpretation developed can provide guidance for the synthesis of linear clusters and chains of controlled lengths, which can be tuned experimentally by using the model-predicted particle sizes and ratios. This permanent chaining of polymer particles can find application in gels and fluids with unusual directional rheology response. In addition, the linear chain structures formed will show anisotropy in heat and electrical conductance that leads to their potential use in microdevice cooling and wiring. The permanent chains of well-defined length and morphology can also be used in tissue engineering as matrices for bio-scaffolds.

References

1. Velev OD, Gupta S (2009) Materials fabricated by micro- and nanoparticle assembly—The challenging path from science to engineering. *Adv Mater* 21:1897
2. Tang Z, Kotov NA (2005) One-dimensional assemblies of nanoparticles: preparation, properties, and promise. *Adv Mater* 17:951
3. Li F, Josephson DP, Stein A (2011) Colloidal assembly: the road from particles to colloidal molecules and crystals. *Angew Chem Int Ed* 50:360

4. Yethiraj A, Thijssen JHJ, Wouterse A, Blaaderen AV (2004) Large-area electric-field-induced colloidal single crystals for photonic applications. *Adv Mater* 16:596
5. Dreyfus R, Baudry J, Roper ML, Fermigier M, Stone HA, Bibette J (2005) Microscopic artificial swimmers. *Nature* 437:862
6. Mackay ME, Dao TT, Tuteja A, Ho DL, Horn BV, Kim HC, Hawker CJ (2003) Molecular architecture and rheological characterization of novel intramolecularly crosslinked polystyrene nanoparticles. *Nat Mater* 2:762
7. Gudiksen MS, Lauhon LJ, Wang J, Smith DC, Lieber CM (2002) Growth of nanowire superlattice structures for nanoscale photonics and electronics. *Nature* 415:617
8. Thelander C, Martensson T, Björk MT, Ohisson BJ, Larsson MW, Wallenberg LR, Samuelson L (2003) Single-electron transistors in heterostructure nanowires. *Appl Phys Lett* 83:2052
9. Terray A, Oakey J, Marr DWM (2002) Single-electron transistors in heterostructure nanowires. *Appl Phys Lett* 81:1555
10. Sharma KP, Kumaraswamy G, Ly I, Mondain-Monval O (2009) Self-assembly of silica particles in a nonionic surfactant hexagonal mesophase. *J Phys Chem B* 113:3423
11. Grzybowski BA, Stone HA, Whitesides GM (2000) Dynamic self-assembly of magnetized, millimetre-sized objects rotating at a liquid–air interface. *Nature* 405:1033
12. Zerrouki D, Baudry J, Pine D, Chaikin P, Bibette J (2008) Chiral colloidal clusters. *Nature* 455:380
13. Gangwal S, Cayre OJ, Velev OD (2008) Dielectrophoretic assembly of metallo dielectric Janus particles in AC electric fields. *Langmuir* 24:13312
14. Piech M, George MC, Bell NS, Braun PV (2006) Patterned colloid assembly by grafted photochromic polymer layers. *Langmuir* 22:1379
15. Jones TB (1995) *Electromechanics of particles*. Cambridge University Press, Cambridge
16. Techaumnat B, Eua-arporn B, Takuma T (2004) Calculation of electric field and dielectrophoretic force on spherical particles in chain. *J Phys D Appl Phys* 37:3337
17. Velev OD, Bhatt KH (2006) On-chip micromanipulation and assembly of colloidal particles by electric fields. *Soft Matter* 2:738
18. Hermanson KD, Lumsdon SO, Williams JP, Kaler EW, Velev OD (2001) Dielectrophoretic assembly of electrically functional microwires from nanoparticle suspensions. *Science* 294:1082
19. Lumsdon SO, Kaler EW, Velev OD (2004) Two-dimensional crystallization of microspheres by a coplanar AC electric field. *Langmuir* 20:2018
20. Gupta S, Alargova RG, Kilpatrick PK, Velev OD (2010) On-chip dielectrophoretic coassembly of live cells and particles into responsive biomaterials. *Langmuir* 26:3441
21. Leunissen ME, Christova CG, Hynnien AP, Royall CP, Campbell AI, Imhof A, Dijkstra M, Roij Rv, Blaaderen AV (2005) Ionic colloidal crystals of oppositely charged particles. *Nature* 437:235
22. Vutukuri HR, Stiefelhagen J, Vissers T, Imhof A, Blaaderen AV (2012) Bonding assembled colloids without loss of colloidal stability. *Adv Mater* 24:412
23. Bharti B, Meissner J, Findenegg GH (2011) Aggregation of silica nanoparticles directed by adsorption of lysozyme. *Langmuir* 27:9823
24. Lin W, Kobayashi M, Skarba M, Changdao M, Galletto P, Borkovec M (2006) Heteroaggregation in binary mixtures of oppositely charged colloidal particles. *Langmuir* 22:1038
25. Stoy RD (1994) Interactive dipole model for two-sphere system. *J Electrostat* 33:385
26. Gupta S, Alargova RG, Kilpatrick PK, Velev OD (2008) On-chip electric field driven assembly of biocomposites from live cells and functionalized particles. *Soft Matter* 4:726
27. Vissers T, Blaaderen AV, Imhof A (2011) Band formation in mixtures of oppositely charged colloids driven by an AC electric field. *Phys Rev Lett* 106:228303

Part V

Summary and Outlook

To conclude, a short summary of the work is given which indicates how the different projects studied address and contribute to the better understanding of the colloidal interactions. We also propose an outlook of the projects to highlight the possible extension and applications of the studied projects.

Chapter 10

Summary and Outlook

The main goal of this Ph.D. research was to get a better understanding of adsorption and aggregation processes occurring in colloidal dispersions in the presence of soft matter. Specifically, the adsorption of nonionic surfactants and of globular proteins onto hydrophilic silica nanoparticles was studied. For the proteins studied in the present work their adsorption onto silica nanoparticles caused hetero-flocculation in a wide pH range, which was also studied by a combination of different experimental techniques. In addition, the aggregation of microparticles was investigated with the aim to produce permanent aggregate structure on a supra-colloidal length scale. In this work, we not only studied the colloidal systems by various experimental techniques, but also accounted for the resulting structures on the basis of different theoretical models. This section of the thesis summarizes the outcome of the studied topics and their impacts on the field of colloid science.

10.1 Interaction Between Hydrophilic Silica and a Nonionic Surfactant

Adsorption of surfactant onto silica surfaces is an important process that plays a vital role in the dispersion stability and governs its other physical properties. We studied the factors affecting adsorption of the nonionic surfactant $C_{12}E_5$ onto silica nanoparticles and in the pores of mesoporous SBA-15 silica. From our adsorption isotherm studies we proved that the limiting surface excess of surfactant is a function of surface curvature and the maximum amount which can be loaded per unit area of particle surface decreases by a factor 3 when the particle size was reduced from 42 to 13 nm. Another important factor that influenced the adsorption phenomenon was the surface chemistry of the silica. We altered the surface chemistry of the silica by addition of the basic amino acid lysine. Lysine showed preferential adsorption over $C_{12}E_5$ molecules and was able to displace the pre-adsorbed $C_{12}E_5$ molecules from silica surface. The displacement of surfactant from silica

nanoparticles was also studied by small-angle neutron scattering (SANS) in silica contrast match conditions. SANS profiles in the absence of surface modifier were fitted by *micelles-decorated bead* model indicating that the surfactant is adsorbed on the surface of silica in the form of discrete surface aggregates. Gradual addition of lysine to the dispersion leads to a decrease in the surface concentration of surfactant aggregates. The SANS study showed that the surfactant desorbed from the silica surface formed wormlike micelles in the bulk and lead to a phase separation of the water- $C_{12}E_5$ system at elevated temperatures.

The effect of surface modifier on the adsorption of $C_{12}E_5$ on silica was also studied in the nanopores of SBA-15 silica. A similar lysine-induced surfactant-desorption effect was observed as on the silica nanoparticles. Here again the transitions occurring in the surfactant aggregate morphology at a fixed $C_{12}E_5$ loading with increasing lysine concentration were traced by SANS. By analyzing the SANS profile on the basis of *Treubner-Strey* model, we established that in the absence of lysine, $C_{12}E_5$ forms discrete bilayer patches at the pore walls, which then transforms to elongated wormlike structures still adhering to the pore walls at intermediate lysine concentrations. A further addition of surface modifier then results in a complete desorption of the surfactant from the pores, which then forms cylindrical micelles in the exterior of SBA-15 pores as in the case of silica nanoparticles.

By studying the adsorption of surfactant onto nanoparticles and in the nanopores, we affirm that there are two important factors governing the aggregative adsorption of these molecules: (1) surface curvature and (2) surface chemistry. Surface curvature can be altered by changing the size of adsorbent particle and surface chemistry can be tempered by the addition of some more strongly adsorbing molecules. These established facts can play an important role in the formulation of dispersions for various biological and industrial applications. On the other hand, our study leaves open questions that need further attention, such as *What is the influence of increasing binding strength of surfactant head group (C_iE_j) to the silica surface on the desorption effect of lysine? What other modifiers are capable of delivering a similar effect?*

10.2 Protein-Nanoparticle Interactions

The interaction of 20 nm silica nanoparticles with two globular proteins, viz. lysozyme and cytochrome C, was studied in an extensive way. In the case of lysozyme, our systematic study of adsorption isotherm proved that the maximum amount of protein per unit area is highly pH responsive. It increases steeply with increasing pH indicating that the electrostatic interaction represents the main driving force. To prove this conjuncture the ionic strength of the dispersion was increased by adding NaCl. Presence of salt in dispersion screens the electrostatic interactions between the constituent charged species, i.e. silica nanoparticles and protein molecules, resulting in a decrease of the adsorbed protein amount with the

increasing salinity. This effect of salinity is taken as evidence for the dominance of charge-charge interactions between protein and silica particles. The binding of a positive protein to a negatively charged silica nanoparticle dispersion resulted in the formation of protein-nanoparticle heteroaggregates. The protein-particle composite showed striking pH responsiveness. The aggregates exist in a pH range from 4 to 10 and completely dissolved both at $\text{pH} < 4$ and at $\text{pH} > 10$. At $\text{pH} < 4$ the silica is only weakly charged, leading to the lack of protein adsorption and hence the lack of silica aggregation. On the other hand, at $\text{pH} > 10$, lysozyme is feebly charged (isoelectric point (IEP) = 11.0) and is unable to glue the negatively charged silica particles together. A pH-dependent study of aggregate morphology by SAXS and analytic centrifugation proved that, at $\text{pH} 4\text{--}6$ compact aggregates are formed whereas in the pH range $6\text{--}10$ the aggregates were loosely packed and of fractal dimension. In addition, the structure factors obtained by the SAXS profiles could be represented by the *Sticky-hard-sphere* model. This model characterizes the system in terms of a short-range attractive potential between the silica particles. High values of the stickiness parameter in the intermediate pH regime give direct evidence of the role of the protein as 'glue' between the negatively charged silica particles.

The protein-induced aggregation of silica nanoparticles observed with lysozyme was compared with corresponding effects with cytochrome C. These two proteins are similar in terms of their sizes, IEP and net surface charge; but differ in their net dipole moments. Aggregation of 22 nm silica particles induced by cytochrome C was observed in the range from $\text{pH} 4\text{--}8$, whereas the aggregating regime for lysozyme was $\text{pH} 4\text{--}10$. For cytochrome C, the shift in the pH values where silica aggregates re-dissolve was attributed to the two factors (1) lower IEP of cytochrome C, and (2) non-uniform distribution of surface charge.

The Thesis addressed several of the fundamental questions about the protein adsorption and induced aggregation with silica nanoparticles. However, some important open questions that arise from the performed work are: *What is the morphology and the extent of denaturation of the adsorbed protein? In pH titrations, when a protein desorbs from silica nanoparticle by the change in pH, does it fully regain its native conformations? Can the surface chemistry of the silica particles be altered, such that the tendency of protein adsorption remains high with no aggregation of nanoparticles?*

10.3 Supra-Colloidal Permanent Assembly of Microparticles

The heteroaggregation of protein and silica nanoparticles was found to be almost completely random, only a slight alteration in the aggregate morphology was possible by changing the pH. In order to achieve highly ordered system, dielectrophoresis (DEP) was used as an external force directing the aggregate morphology. DEP has been widely used for assembling dielectric particles into linear chains

and 2D arrays. However, the assembly formed is temporary and exists only as long as the field is present. The ordered structure completely disassembles, when the field is switched off. In the present work micron sized latex particles of opposite charges were mixed and an immediate application of AC electric field to the biparticle dispersion forces the particles to arrange into linear chains. Since the heteroaggregation of the oppositely charged particles is irreversible, the chains assembled retain their linear structure even after removal of external AC-field. We developed a new model for predicting the distribution of chain lengths of the permanent chains at a given positive-to-negative particle number ratio and size ratio. The model gives an excellent account for the obtained experimental chain lengths. Based on the proposed statistical model and its experimental proof, we proposed the *assembly rules* for harvesting such chain structures: (1) Long chains can be assembled only if the ratio of the sizes (D_{small}/D_{large}) is less than 0.25; (2) Chain length increases with the increase in particle number ratio ($N_{small}/N_{large} > 1$).

The method adopted here for making permanent structures is a novel approach and was only used to get permanent chains. Such assembled system can find their applications in field responsive gels and dispersions with impeccable rheological properties. The study is the first of its kind and generates several questions, which should be addressed in further studies. Some of them are: *Is it possible to fabricate 2D and 3D structures by using biparticle dispersion? How to achieve the DEP directed biparticle assembly at nanoscale? What is the effect of surface charge density of particles on the assembled structures?*

Appendix

A.1 Materials

C₁₂E₅ (Sigma-Aldrich, $\geq 98\%$), 2,6-diaminohexanoic acid (lysine) (Fluka, purity $>98\%$), tetraethyl orthosilicate (TEOS) (ABCR GmbH, purity $>98\%$), D₂O (Eurisotop, 99.9%), ninhydrin reagent (Sigma, 2% solution) Lysozyme from chicken egg white (Sigma-Aldrich, 69,000 units/mg protein, lot no. 019k1320, purity $>90\%$), cytochrome C from equine heart (Sigma-Aldrich, lot no. 070M7031v, purity $\geq 95\%$), organic buffers *N,N*-Bis(2-hydroxyethyl) glycine (BICINE) (Sigma-Aldrich, purity $>99\%$) and 2-(*N*-morpholino)-ethanesulfonic acid (MES) (Sigma-Aldrich, purity $>99\%$). Pierce® bicinchoninic acid (BCA) purchased from Pierce Biotechnology, Inc. (Rockford, IL) were used without further purification. Polystyrene microspheres of sizes 0.90, 4.0 2.0 and 2.2 μm were supplied by *invitrogen*. Water was purified by a Milli-Q water from MilliPore QPAK®(2) unit.

A.2 Mesoporous SBA-15 Silica Characterization

See Fig. [A.1](#).

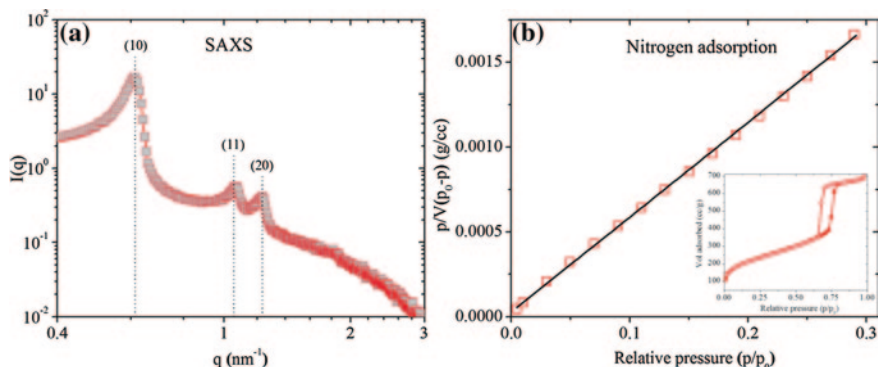


Fig. A.1 Characterization of the SBA-15 silica material **a** SAXS intensity profile $I(q)$ as a function of scattering vector q , the number indicated are the miller indices of the Bragg's reflection from the ordered mesopore; **b** BET plot of the Nitrogen adsorption isotherm along with its linear fit. Complete N_2 adsorption-desorption isotherm is shown in the *inset*

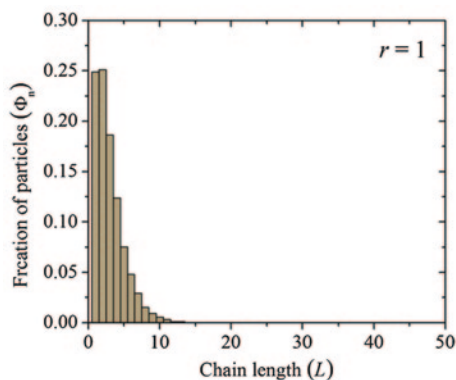


Fig. A.2 Chain length distribution obtained by the arranging two types of balls in a complete random manner into a linear array. The model mimics the chaining scenario for the equal sized particles with equal number ratio. The obtained distribution is in agreement with the experimental results (Chap. 9). The details of the simulations are given in Sect. 3.2.2.1

A.3 Permanent Chaining: Characterizing the Chains Structures

A.3.1 Numerical Simulations

A.3.1.1 Equal-Size Particles

See Fig. A.2.

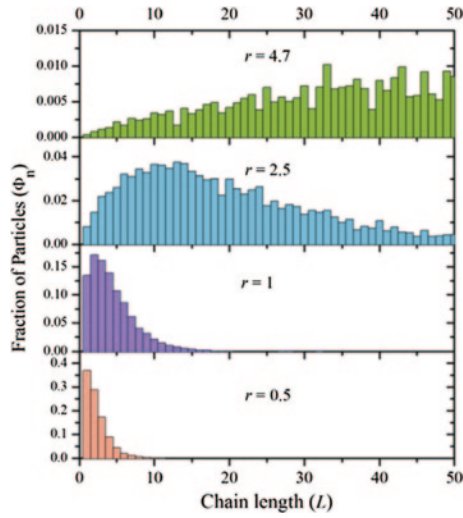


Fig. A.3 Simulation results for unequal sized particles (see Sect. 3.2.2.2) with increasing small-to-large particle number ratio. Simple model of throwing balls-in-boxes reproduces the essence of the experimentally observed increase in chain length with increase in number of small to large particles (Chap. 9)

A.3.1.2 Differently-Sized Particles

See Fig. A.3.

A.3.2 Radial Distribution of Particles

See Fig. A.4.

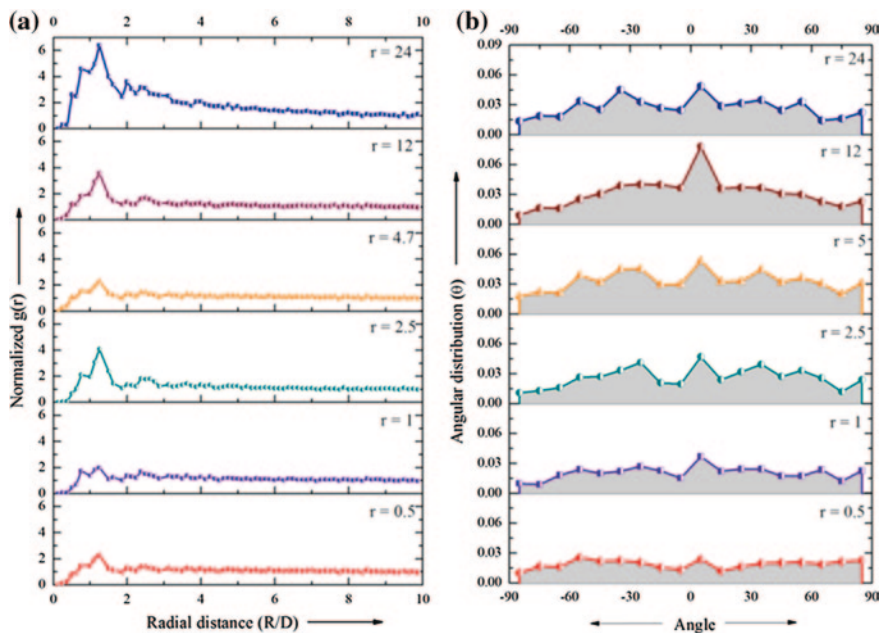


Fig. A.4 Experimental radial and angular distribution obtained by the microscope image analysis for permanent chains formed by 4.0 and 1.0 μm latex particles at increasing particle number ratios ' r ' (Chap. 9). **a** The normalized radial distribution function ' $g(r)$ ' is represented as the function of distance in the units of diameter of the larger latex particle. An increase in the integral intensity of first oscillation of $g(r)$ with particle ratio indicates higher degree of ordering in the system. **b** The *angular* distribution of each pair of larger microspheres is represented as a function of angle with respect to the initially applied electric field. The distribution intensifies along the angle 0° with increasing r , indicating the lack of free movement of the longer chains formed (For details see Chap. 9)